Lattice QCD Studies of the Low-Lying Δ and Λ Resonances in Meson-Baryon Scattering

by

Sarah Skinner

Submitted in partial fulfillment of the
requirements for the degree of
Doctor of Philosophy
at
Carnegie Mellon University
Department of Physics
Pittsburgh, Pennsylvania

Advised by Professor Colin Morningstar

August 11, 2024

Abstract

Scattering amplitudes for several channels are calculated using lattice QCD on a single ensemble of gauge field configurations with $N_\mathrm{f} = 2+1$ dynamical quark flavors and $m_\pi \approx 200$ MeV and $m_K \approx 487$ MeV. The calculations for the πN scattering amplitudes in the $\Delta(1232)$ regime and the coupled channel $\pi\Sigma$-$\bar{K}N$ scattering amplitudes in the $\Lambda(1405)$ regime are detailed. In the coupled channels, two poles are found. The πN s-wave scattering shifts for the total isospins $I = 1/2$ and $I = 3/2$, and the p-wave including the $\Delta(1232)$ resonance are reported. The coupled channel $\pi\Sigma$-$\bar{K}N$ s-wave scattering length is reported. Resonance masses and widths are calculated for the $\Delta(1232)$, the $\Lambda(1405)$, and even the elusive $\Lambda(1380)$. Along with the high-precision scattering amplitudes, methodologies for increasing confidence in our analysis were tested.

Acknowledgments

I am grateful to my advisor, Dr. Colin Morningstar, who supported me in my ideas, ambitions, and independence as a researcher. I would also like to express deep gratitude to my collaborators Fernando Romero-López, Andrew Hanlon, and John Bulava for each being a pillar I could lean on throughout my graduate career. Not only could they answer every almost every question, but they also gave support above and beyond what is expected of any collaborator. Thanks should also go to André Walker-Loud for sharing his innovative ideas and insights and for supporting me in my career goals. In addition, I would be remiss if I did not mention Bárbara Cid Mora and Joseph Moscoso for the adventures and projects shared over the years. I enjoyed working together and growing together as graduate students despite being in different programs around the world. Lastly, I would like to send the warmest regards to my two housemates, Jeremiah Szanto and Rockstar, the two cutest boys, who gave me love and support outside of my graduate career, partially by constantly interrupting my studies.

Computations were carried out on Frontera [1] at the Texas Advanced Computing Center (TACC) under award PHY20009, and at the National Energy Research Scientific Computing Center (NERSC), a U.S. Department of Energy Office of Science User Facility located at Lawrence Berkeley National Laboratory, operated under Contract No. DE-AC02-05CH11231 using NERSC awards NP-ERCAP0005287, NP-ERCAP0010836 and NP-ERCAP0015497. I acknowledge support from the U.S. NSF under awards PHY-1913158 and PHY-2209167.

Contents

List of Tables

List of Figures

Chapter 1

Introduction

Although quantum chromodynamics (QCD) was born in 1973 [2], we still struggle to make experimental predictions with it in the low to medium energy sector. In the high-energy range there is asymptotic freedom, meaning that the strong force coupling is small at short distances. The coupling grows stronger at lower energies, and thus perturbation theory is no longer applicable. When using field theory to calculate scattering observables, one should include all possible Feynman diagrams with the input and output desired. There are infinitely many of these diagrams, but thankfully for most theories, the simplest ones contribute the most, and the more complicated diagrams are used as correction terms. This is not the case in low-energy QCD. The complicated diagrams dominate, and it is impossible to calculate the scattering observables by ordinary perturbation theory. Lattice QCD saves the day by taking a Monte Carlo approach to the problem instead. Using the theory to filter the random sampling, all the diagrams that contribute are included. The only major limitation is statistics.

Most of the known hadrons are *resonances*. Resonances are particles that are not stable and decay into other products, usually on the order of nanoseconds. To study these states using lattice QCD, we calculate the finite volume energy spectrum and then compute the scattering amplitude properties using the Lüscher method. This approach does not make assumptions about the resonances and uses first-principles physics, unlike effective field theory, which relies on phenomenological inputs.

Our calculations utilize the stochastic Laplacian-Heaviside method. This technique efficiently computes quark propagators [3, 4], enabling large statistics on a large lattice volume with high-precision calculations. These algorithms have recently been applied to meson-baryon scattering amplitudes in this thesis and in other analyses [5, 6], demonstrating their valuable computational efficiency and robustness. This powerful methodology enables us to compute higher-precision results using less computation time and resources.

Nucleon-pion ($N\pi$) scattering is a crucial process in nuclear physics. Because the pion is the lightest hadron, the pion exchange between nucleons is one of the primary

mechanisms for the binding of atomic nuclei and nuclear scattering. Furthermore, nucleon-pion scattering includes the narrow $\Delta(1232)$ resonance, which significantly influences many nuclear processes, which includes lepton-nucleon and lepton-nucleus scattering. These processes are particularly relevant for various electron-nucleus and neutrino-nucleus scattering experiments. Lattice QCD results will provide valuable input for models of neutrino-nucleus scattering cross sections, aiding next-generation experiments such as DUNE [7] and Hyper-K [8], which aim to measure unknown properties of neutrinos. One of the frontiers in these lattice QCD applications is understanding the Δ-resonance contribution to the inelastic νN structure. To achieve this, it is essential to establish control over $N\pi$ scattering, as it is a necessary component of the nucleon inelastic resonant structure. The main results of the πN study are in Figures 7.3-7.5 and Tables 7.2-7.3 using Equations 7.1-7.4.

In lattice QCD calculations, it is vital that there are sufficient hadronic operators (Section 3.1) used to calculate the scattering observables. If a necessary operator is omitted, then this can lead to incorrect results. Therefore, it is prudent to find ways to check for such missing states especially in the cases where the hadronic operators reflect exotic particles. Several new methods are outlined and tested. These methods have some success and some setbacks in their current status.

In meson-baryon scattering, the $\Lambda(1405)$ is currently recognized as a 4-star resonance by the Particle Data Group (PDG) [9], which indicates the confidence of the particle's existence out of 4 stars. The $\Lambda(1380)$, a possible nearby resonance of the same quantum numbers, is listed in the PDG with only a 2-star status. Past phenomenological models have led to conflicting conclusions about whether or not there are one or two resonances in this energy region, and experimental efforts have also presented different tentative conclusions [9]. This controversy warrants a first-principles calculation of the scattering amplitudes. Efforts using lattice QCD have been made in the past [10–17], but the results presented in References [18, 19] and reviewed in this thesis are the first calculations of the scattering amplitudes from lattice QCD using a full set of one- and two-hadron operators. The main results of our $\Lambda(1405)$ study are in Figures 8.4b and 8.6 using Equation 8.13.

In this thesis, I will thoroughly review the extensive process of computing and analyzing lattice QCD simulations, present new potential methodologies to verify a vital part of our analysis chain, and review important scattering results calculated from such simulations.

Chapter 2

Lattice QCD

Through Lattice QCD, we can make quantitative predictions of particle interactions directly from QCD of the Standard Model. In this work only the effects of the strong force are considered; weak nuclear and electromagnetic effects are ignored. The strong force is a quantum field theory based on local $SU(3)$ gauge symmetry, a theoretical framework where quantum field operators create and annihilate particles. The particles in this case include quarks (fermions) and gluons (bosons), and alongside momentum and spin, in QCD the particles gain an additional degree of freedom. To characterize this $SU(3)$ freedom, each quark carries one of three unique color charges, red, green, or blue, and consequently the gluons have eight color states, which are compositions color charge and anticharge. The theory is also a gauge theory, which indicates the requirement of a constraint on the degrees of freedom that define the theory. Nonperturbative calculations of QCD can be achieved by introducing a space-time lattice, and a natural and necessary consequence of this lattice is that it will act as a regulator of ultraviolet divergences.

In order to study this theory on a lattice, many necessary modifications will have to be made, but these modifications will satisfy some basic requirements: when the lattice spacing is taken to zero and the volume to infinity, the lattice QCD action matches the continuum QCD action. Also, gauge invariance will be maintained in the lattice QCD action when formulated on the lattice. These principles will ensure that the simulation will represent real strong-interaction physics.

2.1 QCD in Continuum

Setting up any lattice QCD simulation begins with the continuum physics QCD Lagrangian[1] which includes the free field Lagrangians for fermions and gluons and the interaction term between them. To gain a full understanding of the theory, I will

[1] Any mention of 'the Lagrangian' in this thesis is actually the Lagrangian density $\mathcal{L}$ rather than the traditional Lagrangian L.

iterate through each of these parts as well as how observables are calculated from them. Note that natural units are used throughout this thesis.

2.1.1 Free Fermionic Fields

Despite the fact that no quark in the Standard Model can exist as a free particle due to the color-singlet requirement of confinement, in this section, we will ignore gluons and the color index and study free fermionic fields for quarks. When no forces are present, fermionic fields, $\psi(x)$ and $\overline{\psi}(x)$, that depend on the four-dimensional space-time variable x,[2] behave according to the fermionic Lagrangian,

$$\mathcal{L}_{\mathrm{F}}[\psi, \overline{\psi}] = \sum_{f=1}^{N_f} \overline{\psi}_{\alpha}^{(f)} (i\gamma_{\alpha\beta}^{\mu} \partial_{\mu} - m^{(f)} \delta_{\alpha\beta}) \psi_{\beta}^{(f)}, \tag{2.1}$$

where γ^{μ} are the Dirac-representation γ-matrices, $m^{(f)}$ is the flavor mass, α and β refer to Dirac indices, μ and ν are the Minkowski space-time indices, and f represents the flavor index. The color index is omitted here. Although N_f, the number of fermions, could be any number, there has only been confirmed evidence of six flavors of quarks: up, down, strange, charm, top, and bottom. In this work, only the up (u), down (d), and strange (s) quarks will be considered due to their light masses compared to the other quarks. Not only do the u, d, and s quarks make up most known matter, when the up and down are treated as degenerate particles called *light* (l) quarks with $m_l \equiv m_u = m_d$, the isospin symmetry $SU_I(2)$ is exact, further simplifying our calculations. Due to computational costs, m_l will not be set to the physical value of m_u or m_d, instead it will be set to 200 MeV or higher. This effect will shift our final scattering results from the physical values.

Each field is a function of four-dimensional space-time. The indices representing space-time directions use Greek letters beginning with the letter μ and can have values 0,1,2,3 for t, x_1, x_2, x_3 for the temporal and three spatial directions. The Minkowski space-time interval is given as $dx^2 = dt^2 - dx_1^2 - dx_2^2 - dx_3^2$ in natural units where x represents the space-time coordinate (t, x_1, x_2, x_3). The fermionic fields are massive Dirac spinors with Dirac indices, represented by the Greek alphabet beginning with α, which take values $\alpha = 0, 1, 2, 3$.

2.1.2 Gluon Fields

The gluon fields, $\mathcal{A}_{\mu}(x)$, are the gauge fields for chromodynamics. Rather than the $U(1)$ symmetry in electromagnetism, the strong force features $SU(3)$ transformation properties, making it more complicated to calculate theoretical observables. The

[2] All fields and variables with space-time dependence will acknowledge the x in the initial definition, and the (x) will be implied when omitted in further equations.

Lagrangian for gluon fields is most simply written in terms of the gluon field tensor $G^A_{\mu\nu}(\mathcal{A})$:

$$\mathcal{L}_{\rm G}[\mathcal{A}] = -{\rm Tr}(\frac{1}{4}G^A_{\mu\nu}G^{\mu\nu}_A). \tag{2.2}$$

The gluon field tensor is defined as

$$G^A_{\mu\nu} = \partial_\mu \mathcal{A}^A_\nu - \partial_\nu \mathcal{A}^A_\mu - g f_{ABC}\mathcal{A}^B_\mu \mathcal{A}^C_\nu$$

where f_{ABC} are structure constants of the $SU(3)$ group and g is the QCD coupling. The gluon generators—represented by uppercase Latin letters $A, B, C...$—can have values 1,2,...,8 for each $SU(3)$ generator index. Each of the generators is associated with a gluon and is often written in terms of the 3×3 Gell-Mann matrices, λ, and determines each gluon's contribution to the gluon field,

$$\mathcal{A}_{\mu ab} = \sum_{A=1}^{8} \mathcal{A}^A_\mu \frac{\lambda_{Aab}}{2}.$$

The Gell-Mann matrices carry the $SU(3)$ transformation properties of the color charge in the gluon field interaction and a Lie algebra according to

$$[\lambda^A, \lambda^B] = 2i f_{ABC}\lambda^C.$$

These $SU(3)$ transformation properties not only give us eight gluons and determine the transformation of the color charge, but they also cause the phenomenon unique to the strong force: gluon self-interactions. When the free gluon Lagrangian is expanded, not only is there a kinetic term for each gluon, but there are also three-gluon self-interactions and four-gluon self-interactions. These gluonic self-interactions increase the number of possible Feynman diagrams that contribute to a given interaction. In the high-energy region of the strong force, the more complicated diagrams can be ignored, but for our calculations of interest, we must account for them.

2.1.3 The Gluon-Fermion Interaction

Finally, we have reached the interaction term of the strong-force Lagrangian, which dictates how gluons and fermions interact with each other. The interaction term is defined as

$$\mathcal{L}_{\rm int}[\psi, \overline{\psi}, G] = -g \sum_{f=1}^{N_f} \overline{\psi}^{(f)}_{a\alpha}(\gamma^\mu_{\alpha\beta}\mathcal{A}_{\mu ab})\psi^{(f)}_{b\beta}. \tag{2.3}$$

Though all terms have been defined previously in the free field, the fermions have gained a new index for the fermionic color charge represented by lowercase Latin letters, $a, b... = 1, 2, 3$. This new color dimension allows for resonances such as Δ^{++}.

This term can be derived naturally by working from the free fermionic Lagrangian and requiring it to be invariant under local $SU_c(3)$ transformations properties. Consider the fermionic Lagrangian (Equation 2.1) and the transformations $\psi \to \psi' = \Omega\psi$ and $\overline{\psi} \to \overline{\psi}' = \overline{\psi}\Omega^\dagger$, where Ω is a local $SU_c(3)$ transformation, which is a special unitary matrix. When these transformation properties are applied to our fermionic Lagrangian, we would hope that it would be invariant, but instead the result gains an extra term $\overline{\psi}\Omega^\dagger(\partial_\mu\Omega)\psi$. Because the free fermionic Lagrangian does not have the $SU_c(3)$ transformation property required by QCD, we must rewrite the Lagrangian into one that does. This is easily solved by replacing the derivative with the gauge-covariant derivative $\mathcal{D}_\mu = \partial_\mu + i\mathcal{A}_\mu(x)$ and the additional property $\mathcal{A}_\mu \to \mathcal{A}'_\mu = \Omega\mathcal{A}_\mu\Omega^\dagger + i(\partial_\mu\Omega)\Omega^\dagger$. Now, the new form behaves as expected, the gluon kinetic term is fixed, and the interaction term was naturally retrieved. A similar strategy will be used on the lattice.

After combining the fermionic and gluonic Lagrangians, we have arrived at the QCD Lagrangian, the starting place for our lattice simulation. Altogether, these terms form the QCD Lagrangian that dictates the motion of fermions and gluons in a system,

$$\mathcal{L}[\psi, \overline{\psi}, G] = \sum_{f=1}^{N_f} \overline{\psi}^{(f)}_{a\alpha}(i\gamma^\mu_{\alpha\beta}\mathcal{D}_{\mu ab} - m^{(f)}\delta_{\alpha\beta}\delta_{ab})\psi^{(f)}_{b\beta} - \mathrm{Tr}(\frac{1}{4}G^A_{\mu\nu}G^{\mu\nu}_A). \tag{2.4}$$

This Lagrangian gives us the building blocks for QCD interactions. In terms of Feynman diagrams, the building blocks are outlined in Figure 2.1.

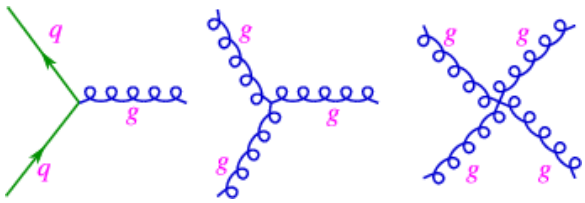

Figure 2.1: Feynman diagram building blocks for lattice QCD. The blue coil lines with label 'g' represent the gluon lines, and the green arrowed lines labeled with 'q' represent quark lines. These building blocks are a diagrammatic representation of all possible interactions of quarks and gluons through QCD. Figure was obtained from University of Sheffield Open Educational Resources [20].

2.1.4 Observables from Continuum

The strategy for putting QCD on the lattice is achieved using the path integral approach and in that approach, the primary mathematical tools to study quantum mechanical systems on a lattice are vacuum expectation values (VEVs). Define Z as

$$Z = \int \mathcal{D}[\psi, \overline{\psi}, \mathcal{A}_\mu]\ e^{iS[\psi,\overline{\psi},\mathcal{A}_\mu]/\hbar}, \tag{2.5}$$

where the integration region is all possible field configurations and S is the action $S = \int d^4x\mathcal{L}$. The formula to calculate the vacuum expectation value (VEV) for an observable $\mathcal{O}$ is then given by

$$\langle\mathcal{O}\rangle = \frac{1}{Z}\int \mathcal{D}[\psi,\overline{\psi},\mathcal{A}_\mu]\; e^{iS/\hbar}\mathcal{O}[\psi(t),\overline{\psi}(t),\mathcal{A}_\mu(t)] \tag{2.6}$$

where Z is the normalization factor i.e. the transition function integrated over all space-time and $\mathcal{O}$ is some operator that is composed of the fermionic and gluonic fields.

There are a few observables of particular interest when computing values that can be compared to experiment: two-point correlation functions. Two-point correlation functions, or *correlators*, are defined as

$$C_{ij}(t) = \langle\mathcal{T}\mathcal{O}_i(t)\overline{\mathcal{O}}_j(0)\rangle. \tag{2.7}$$

where $\mathcal{T}$ is the time-ordered operator $\mathcal{O}_i$ are operators that are functionals of fermionic and gluonic fields, and spatial sites have been summed over. The two-point correlation function gives access to the finite-volume energy spectrum (explained in detail in Section 2.2.2), a valuable step in computing scattering observables from the lattice.

2.2 QCD in Discretized Finite Volume

The next step is to write our Lagrangian in discrete space, though we will take care to ensure that the continuum physics can be retrieved when taking the lattice spacing to zero and the volume to infinity. As a natural consequence of using finite volume, the energy and momentum spectrum will be discretized on the lattice as well.

2.2.1 The Lattice and its Effects

The lattice used in this example is an isotropic tesseract grid Λ defined by a set of vector indexes representing x_μ such that $x_\mu = an_\mu$, where a is the lattice spacing for both spatial and temporal dimensions, n_μ is the vector index, and $N = x_{\max}/a$. In summary,

$$\Lambda \equiv \{n_\mu = \{n_0, n_1, n_2, n_3\} | n_0, n_1, n_2, n_3 = 0, 1, ..., N-1\}. \tag{2.8}$$

The momentum is then quantized to be

$$\mathbf{p} = \frac{2\pi}{L}\mathbf{n}, \tag{2.9}$$

where L is the spatial extent of the Lattice. The momentum is constrained to the range $(-\pi/a, \pi/a]$ due to the cutoff effects of the lattice spacing.

2.2.2 Two-point Correlation Functions

A finite-volume with open temporal boundary conditions will yield a discretized energy and momentum spectrum. With an appropriately large time extent T, by inserting a complete set of energy eigenstates, we may write the correlation functions in terms of the energies E_n and overlaps onto the steady-state eigenvectors $|n\rangle$,

$$\begin{aligned} C_{ij,T}(t) &= \langle 0|\mathcal{T}\mathcal{O}_i(t+t_0)\overline{\mathcal{O}}_j(t_0)|0\rangle \\ &= \sum_{n=0}^{\infty}\langle 0|\mathcal{O}_i(t)|n\rangle\langle n|\overline{\mathcal{O}}_j(0)|0\rangle e^{i(E_n-E_0)t}. \end{aligned} \tag{2.10}$$

As shown in this equation, the two-point correlation function can be related to the discrete energies in a finite volume. Though the discrete energy spectrum can give some qualitative information, the observables we are interested in are the continuum phase shifts that can be compared to experiment. Using the Lüscher method (Chapter 5), we can use the spectrum to calculate phase shifts in the continuum limit for a given interaction.

2.2.3 Euclidean time

A key feature of lattice physics is the "Euclidean time" or "imaginary time". This simply means that the time coordinate is transformed to Euclidean time, τ, using the transformation $t \to -i\tau$. Not only does this transformation make the Minkowski metric equivalent to the identity matrix, it makes Monte Carlo estimations of Lattice QCD possible. To understand this, let us look at the VEV for a given operator $\mathcal{O}$ again but with Euclidean spacetime,

$$\langle\mathcal{O}\rangle = \frac{1}{Z}\int \mathcal{D}[\psi,\overline{\psi},\mathcal{A}_\mu]\; e^{-S[\psi,\overline{\psi},\mathcal{A}_\mu]}\mathcal{O}[\psi(t),\overline{\psi}(t),\mathcal{A}_\mu(t)]. \tag{2.11}$$

Now, the VEV is a sum of the possible configurations, each multiplied by a weight (e^{-S}) rather than a phase (e^{iS}), where S is real-valued. Because the weight is real and positive, it can be interpreted as a probability, where the classical path is at the maximum, and can be used for Monte Carlo-Metropolis Hastings importance sampling, encoding the physics into the stochastic simulation. When written as a Monte Carlo integral and converted to Euclidean time, the transition function becomes equivalent to the partition function of statistical mechanics.

Another incredibly important consequence of the time transformation is the spectral decomposition of the correlation functions,

$$C_{ij}(\tau) = \sum_{n=0}^{\infty}\langle 0|\mathcal{O}_i(0)|n\rangle\langle n|\overline{\mathcal{O}}_j(0)|0\rangle e^{-(E_n-E_0)\tau}. \tag{2.12}$$

In this new form, each correlator is not a sum of phases but now a sum of decaying exponentials, where the energies can be retrieved more precisely.

2.2.4 Discretization and Gauge Links

The interaction term between fermions and gluons naturally arises from enforcing local gauge invariance in the fermionic Lagrangian. In order to write the Lagrangian using a space-time lattice and maintain gauge invariance, we need to rewrite our gluon fields in terms of gauge links [21].

A standard method in computational science is to use the central difference formula to evaluate the derivatives on the lattice. The free fermionic Lagrangian in Euclidean space-time on the lattice becomes

$$\mathcal{L}_{\mathrm{F}}[\psi,\overline{\psi}] = \sum_{f=1}^{N_f} \overline{\psi}_{\alpha}^{(f)}(n) \left(\sum_{\mu=1}^{4} \gamma_{\alpha\beta}^{\mu} \frac{\psi_{\beta}^{(f)}(n+\hat{\mu}) - \psi_{\beta}^{(f)}(n-\hat{\mu})}{2a} - m^{(f)} \psi_{\alpha}^{(f)}(n) \right), \quad (2.13)$$

where a is the lattice spacing for all dimensions[3]. Just like in continuum physics, we require that our discretized Lagrangian satisfies local gauge invariance. Our final equation should have this quality, but in equation 2.13, when the transformations $\psi(n) \to \Omega(n)\psi(n)$ and $\overline{\psi}(n) \to \overline{\psi}(n)\Omega^{\dagger}(n)$ are applied, there are leftover terms with $\Omega(n+\hat{\mu})$ and $\Omega(n-\hat{\mu})$ in the transformed Lagrangian, indicating the need for gauge links, $U_{\mu}(n)$, which connect the space-time points. A graphical representation is shown in Figure 2.2.

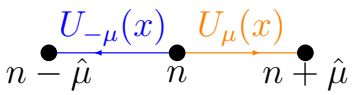

Figure 2.2: Graphical diagram of gauge links. [22]

These gauge links transform as $U_{\mu}(n) \to \Omega(n)U_{\mu}(n)\Omega^{\dagger}(n+\hat{\mu})$ and $U_{-\mu}(n) \to \Omega(n)U_{-\mu}(n)\Omega^{\dagger}(n-\hat{\mu})$ under gauge transformation. By using a new discretized covariant derivative as,

$$\mathcal{D}_{\mu}^{'} \to \frac{U_{\mu}(n)\psi_{\beta}^{(f)}(n+\hat{\mu}) - U_{-\mu}(n)\psi_{\beta}^{(f)}(n-\hat{\mu})}{2a}, \quad (2.14)$$

the discretized fermionic Lagrangian now behaves as it should under the local gauge transformation. We can relate this discretized covariant derivative to the continuum covariant derivative with the relation using the gauge transporter, a continuum object with the same gauge transformation properties, approximated as, $U_{\mu}(n) \approx (\exp\{ia\mathcal{A}_{\mu}(n)\})$, which recovers the correct form, $\mathcal{D}_{\mu} = \partial_{\mu} + ig\mathcal{A}_{\mu}$ in the continuum limit. Like in continuous spacetime, enforcing local gauge invariance in fermionic fields determines the interaction between the fermions and gluons.

The discretized action can be separated into fermionic (S_F) and gluonic (S_G) parts written,

$$S[\psi,\overline{\psi},U] = S_F[\psi,\overline{\psi},U] + S_G[U] = \overline{\psi}D[U]\psi + S_G[U] \quad (2.15)$$

[3]Lattice spacing can be different for spatial and temporal dimensions.

where fermion indices are suppressed and $D[U]$ is known as the *Dirac matrix*. As will be shown in the next chapter, calculating Monte Carlo observables requires inverting the Dirac matrix. This matrix relates space-time coordinates, spin, and color between the fermionic fields and can have $\sim 10^{16}$ elements. Inverting the Dirac matrix is our most computationally expensive task.

2.2.5 Discretization and Fermions

Though we managed to account for local gauge invariance with our discretized Lagrangian, there are other consequences of discretization such as fermion doublers. When we look at the Fourier transform of this Lagrangian, we see that there is not just one pole in the propagator at $p^2 = m^2$ as expected, but $2^d - 1$ poles at the edges of the Brillouin zone as well. These poles, the *fermion doublers*, are unphysical, and their effect can be reduced by the addition of improvement terms in the Lagrangian. These improvement terms must satisfy the requirements outlined above, and they must vanish in the continuum limit. There are many variations of these terms, but the one used in this study is called the *Wilson term*.

Despite the reduction of the doublers, a new problem arises as the Wilson term increases chiral symmetry breaking. Although we could try to add yet another term to address this issue, it has been shown in Ref [23] that it is impossible to correct both problems completely on a lattice; thus, we are stuck with choosing one effect or the other. Our choice of action must balance the need to minimize negative effects on the observables we wish to study and the need to minimize computational times. We chose a clover-improved action because its violations of chirality are sufficiently small and computational times are adequately fast. The Lagrangian used to generate our results is the tree-level improved Lüscher-Weisz gauge action [24] and a non-perturbatively O(a)-improved Wilson fermion action [25].

2.3 Metropolis-Hastings Simulation

The Metropolis-Hastings simulation is a type of Markov-chain Monte Carlo simulation. A Monte Carlo simulation is the use of pseudo-random sampling to calculate a given result. A Markov-Chain simulation is a Monte Carlo simulation that samples and maps a probability distribution randomly, but uses each sampling to guide the next sampling choice. This method requires detailed balance and ergodicity to produce accurate results, but once these conditions are enforced, this method will provide speed and efficiency in a high-dimensional simulation. A Metropolis-Hastings simulation is a Markov-chain that uses an "accept/reject" strategy to achieve the required fixed-point probability distribution of the Markov-chain.

Concepts relevant to the calculation of our results are outlined in this section. Details pertaining to the ensemble setup used for results can be found in Section 6.1.

2.3.1 Observables on the Lattice

As stated in a previous section, the standard method of calculating the VEV of an operator $\mathcal{O}$ in a Monte Carlo simulation is an integration i.e. a sum over all dimensions written as

$$\langle \mathcal{O} \rangle_T = \frac{1}{Z_T} \int \mathcal{D}[\psi, \overline{\psi}] \mathcal{D}[U] \mathcal{O}[\psi, \overline{\psi}, U] e^{-S[\psi, \overline{\psi}, U]}. \tag{2.16}$$

where T indicates the finite time extent, and is normalized by the partition function,

$$Z_T = \int \mathcal{D}[\psi, \overline{\psi}] \mathcal{D}[U] e^{-S[\psi, \overline{\psi}, U]}. \tag{2.17}$$

The integration includes a product of differentials in all flavor, spin, color, and space-time indices in the manner:

$$\mathcal{D}[\psi, \overline{\psi}] \equiv \prod_{n \epsilon \Lambda} \prod_{f,a,\alpha} \mathrm{d}\psi^{(f)}_{a\alpha}(n) \mathrm{d}\overline{\psi}^{(f)}_{a\alpha}(n) \quad \text{and} \quad \mathcal{D}[U] \equiv \prod_{n \epsilon \Lambda} \prod_{\mu=1}^{4} \mathrm{d}U_\mu(n). \tag{2.18}$$

The integration over the Grassman-valued fermionic fields cannot be estimated using Monte Carlo. Thankfully, because they are in the form of a multi-variate Gaussian, they can be evaluated analytically:

$$\langle \mathcal{O} \rangle_T = \frac{\int \mathcal{D}[U] F(D^{-1}[U]) \mathrm{det} D[U] e^{-S_G[U]}}{\int \mathcal{D}[U] \mathrm{det} D[U] e^{-S_G[U]}}, \tag{2.19}$$

where $\mathcal{O}$ has been partially evaluated and rewritten in terms of Wick contractions into a function F that only depends on $D^{-1}[U]$. Now, all that remains is the integration over the gluon fields, which can be done using Monte Carlo integration. Note that task of inverting the Dirac matrix is the most computationally intensive task of this whole simulation and analysis chain, yet we need hundreds of these observables in the form of correlators in order to calculate meaningful results. In the next chapter, I will explain how we tackle this issue.

2.3.2 Variance estimation methods

With a statistically independent set of samples, there are two common methods to estimate the variance of a given quantity on those samples, *bootstrap* and *jackknife* resampling methods. In either method, to measure the variance, many subsets x_i of the original set x are made, that is, $x_i \exists x$. Using these sets, the variance of the mean is estimated as

$$\sigma^2_{\overline{x}} = \langle \overline{x}^2 \rangle - \langle \overline{x} \rangle^2, \tag{2.20}$$

where $\overline{x}$ indicates the mean of an individual set, and $\langle\rangle$ indicates an average over all sets.

Jackknife

To generate sets for jackknife-resampling, from the original set x of size N, generate N copies of x, but for each new set x_i, the element x_i is removed. Because the resampling sets are very similar to the original set, the variance estimation is similar to a simple Monte Carlo estimation and can often underestimate the variance.

To measure the covariance, jackknife specific normalization must occur for accurate results and is estimated as

$$\text{cov}(f_i, f_j) = \frac{N-1}{N} \sum_{i=1}^{N} (\langle f \rangle_i - \langle f \rangle^J)(\langle f \rangle_j - \langle f \rangle^J), \tag{2.21}$$

where $\langle f \rangle_i$ is the average of the i^{th} jackknife resampling of f and $\langle f \rangle^J$ is the average over all jackknife samplings.

Bootstrap

For bootstrap resampling, N_B new sets of size N are generated, and the elements are chosen by randomly sampling the original set. This method tends to compute a larger variance than the jackknife method due to the random picking. One caveat of this method is that outlier samples can be oversampled for the random picker can choose those samplings multiple times.

To measure the covariance, bootstrap-specific normalization must occur for accurate results and is estimated as

$$\text{cov}(f_i, f_j) = \frac{1}{N_B - 1} \sum_{i=1}^{N_B} (\langle f \rangle_i - \langle f \rangle^B)(\langle f \rangle_j - \langle f \rangle^B), \tag{2.22}$$

where $\langle f \rangle_i$ is the average of the i^{th} bootstrap resampling of f and $\langle f \rangle^B$ is the average over all bootstrap samplings.

2.3.3 Generating Configurations

Because of the similarities in structure, lattice QCD simulations are equivalent to Monte Carlo simulations of statistical mechanics, though they will not reflect the same physics. For example, throughout this section there will be Euclidean time and Metropolis-Hastings (MH) time. The Euclidean time represents the manipulated physical time dimension, while the other is a simulation construct. Each unit in MH time represents one sweep over all lattice points where each point has been updated to generate the next sampling. If you were to study this "evolution" of the sampling on its own, it would appear as a four-dimensional thermodynamics simulation. The process of generating each sampling is given the by dimension MH time in units of molecular dynamics units (MDUs) because of the coincidence. Usually, there are more

than one MDU between each sampling measurement to prevent statistical dependence between samplings.

We can only obtain accurate samplings after the lattice simulation has passed a *thermalization* stage and achieved a *detailed balance*. Detailed balance is commonly known as an equilibrium state in a thermodynamics simulation. When the simulation reaches detailed balance, the transition from one state to the next is just as likely to happen in reverse order. Only once the simulation reaches thermalization do we use the samples for our results. To estimate how long it takes to reach this point, a small amount of samplings are run twice, once with a 'cold' start (all values initialized to zero) and once with a 'hot' start (all values initialized randomly). The thermalization time is considered the total MH time it takes for the same observables calculated on the two Markov chains to match in value.

The ability to set a hot and cold start for the simulation is possible because the simulation is *ergodic*, meaning that all configurations are possible and reachable in the probability distribution, no matter how unlikely. This means that we can start using any configuration desired and that the simulation will reach the detailed balance described above. As with continuum quantum physics, all configurations are possible, but paths further away from the classical path are less likely.

In the Metropolis method, a new field configuration is proposed, and then it is accepted or rejected based on the change to the action. When generating gauge configurations, proposing large changes to the current configuration is preferred to reduce computation cost and autocorrelation effects, but such proposals are often rejected due to large changes in the action. It is therefore ideal to set up an updating proposal probability so that the updating scheme can make large changes while keeping the change to the action small.

In order to determine the updating proposal probability between each MC sample in the MH chain, the Hybrid Monte Carlo [26] (HMC) and Rational Hybrid Monte Carlo [27] (RHMC) algorithms are used, HMC for the light quarks and RHMC for the the strange. In the MH simulation, the next sampling is computed by *sweeping* across the lattice updating each point to produce a new sampling. This sampling must be statistically independent of the last. In order to ensure that there are as few MDUs as possible between samples while still maintaining equilibrium, the updates are determined using *importance sampling* where a given probability distribution is used to guide the next sample in such a way that the simulation maintains detailed balance and ergodicity while speeding up calculations. The target probability distribution that we want to use to achieve these properties is

$$p(U) = \frac{\det D[U] e^{-S_G[U]}}{\int \mathcal{D}\left[U'\right] \det D\left[U'\right] e^{-S_G[U']}}, \tag{2.23}$$

but this can still be computationally intense to calculate the determinant of the Dirac matrix. The probability distribution does not need to be perfect, so we can estimate it instead. The HMC and RHMC algorithms are used in tandem to estimate this

probability density and both use a fictitious action and the Hamiltonian equations of motion to determine the update. The fictitious action S_{eff} is generated by replacing $\det De^{-S_G[U]}$ with an integral over $e^{-S_{\text{eff}}}$ in the probability.

$$\det De^{-S_G[U]} \approx \int \mathcal{D}\phi_l^\dagger \mathcal{D}\phi_l \mathcal{D}\phi_s^\dagger \mathcal{D}\phi_s \; e^{-S_{\text{eff}}[\phi_l, \phi_l^\dagger, \phi_s, \phi_s^\dagger]}, \tag{2.24}$$

where $S_{\text{eff}}[\phi_l, \phi_l^\dagger, \phi_s, \phi_s^\dagger] = S_G + S_l[\phi_l, \phi_l^\dagger] + S_s[\phi_s, \phi_s^\dagger]$, and where S_l contains the estimated light-quark contribution to the action and S_s contains the estimated strange-quark contribution. Both methods begin with estimating the respective quark determinants from Equation 2.24,

$$\det D = \det D^{(u)} \det D^{(d)} \det D^{(s)}, \tag{2.25}$$

where $\det D^{(u)}$, $\det D^{(d)}$, and $\det D^{(s)}$ are the up, down, and strange quark determinants.

Though the RHMC method could in principle be used to calculate all three quarks updated at the same time, it can fail if the matrix is ill-conditioned. Dirac matrices representing lower-mass quarks are more likely to have negative fluctuations in the eigenvalues and thus have an ill-conditioned matrix. The HMC method is much more robust and therefore can handle such cases, but is limited to an even number of quarks that have the same mass.

Hybrid Monte Carlo Setup

In order to construct the fictitious Hamiltonian, first we rewrite the light-quark fermion determinants in terms of light pseudo-fermions ϕ_l,

$$\det D^{(u)} \det D^{(d)} = \det[D^{(l)\dagger} D^{(l)}] = \int \mathcal{D}\phi_l^\dagger \mathcal{D}\phi_l \exp\left[\phi_l^\dagger \left(D^{(l)\dagger} D^{(l)}\right)^{-1} \phi_l\right], \tag{2.26}$$

where ϕ_l is computed by first computing a noise vector η with a Gaussian distribution with variance of $1/2$ and then calculating $\phi_l = D^\dagger \eta$. The normalization factors have been absorbed by the path-integral measures. The light-quark contribution is consequently

$$S_l = \phi_l^\dagger \left(D^{(l)\dagger} D^{(l)}\right)^{-1} \phi_l. \tag{2.27}$$

Rational Hybrid Monte Carlo Setup

To continue constructing the fictitious Hamiltonian, we rewrite the strange quark fermion determinant in terms of strange pseudo-fermions ϕ_s,

$$\det D^{(s)} = \det[D^{(s)\dagger} D^{(s)}]^{1/2} = \int \mathcal{D}\phi_s^\dagger \mathcal{D}\phi_s \exp\left[\phi_s^\dagger \left(D^{(s)\dagger} D^{(s)}\right)^{-1/2} \phi_s\right], \tag{2.28}$$

where ϕ_s is computed by first computing a noise vector η with a Gaussian distribution with variance of $1/2$ and then calculating $\phi_s = (D^\dagger D)^{1/4}\eta$. The normalization factors have been absorbed by the path integral measures. The fourth-root can be estimated with the rational approximation,

$$\left(D^\dagger D\right)^{\frac{1}{4}} \approx \alpha_0 1 + \sum_i \frac{\alpha_i}{D^\dagger D + \beta_i}, \tag{2.29}$$

where α_i and β_i are coefficients that specify the approximation and are evaluated using a multi-shift solver [28]. The strange quark contribution is consequently

$$S_s = \phi_s^\dagger \left(D^{(s)\dagger} D^{(s)}\right)^{-1/2} \phi_s. \tag{2.30}$$

Ensuring Ergodicity

Though we have light and strange contributions to the effective action, we still need fictitious momentum, π. Here, we introduce a canonical conjugate momentum of the gauge links, normalized using a Gaussian integrand, to define π. The complete fictitious Hamiltonian is then outlined as

$$H = \frac{1}{2}\pi^\dagger \pi + S_{\text{eff}}[U, \phi, \phi^\dagger]. \tag{2.31}$$

Then, we can evolve the gauge field by integrating Hamilton's equations of motion. The equations of motion for the fictitious Hamiltonian evolve in MH time rather than Euclidean time. The motion here is does not only optimize the MH updating scheme, but turns the lattice into the 4D-thermodynamics simulation.

To ensure ergodicity, the pseudo-fermion and momenta fields must be regenerated each trajectory. Because new equations of motion were defined in the MH time, the discretization effect causes error to the probability distribution. This is corrected for by using a final accept/reject step

$$P_{\text{accept}} = \min(1, e^{-\delta H}), \tag{2.32}$$

that determines whether the element is updated or not when performing the sweep. The RHMC and the HMC enable the update to propose large changes to the configuration while keeping the change to the action small.

2.3.4 Autocorrelation

Although a lot of time is saved by using a Markov chain, there is an inherent risk of autocorrelation affecting our results. An important feature of a Monte Carlo simulation is that each sample is statistically independent. In a traditional Monte Carlo simulation, each sample would be computed from a random initialization, but with

a Markov chain each new configuration is calculated from a previous configuration. This saves an immense amount of time for each sample does not need to undergo thermalization, but if there are not enough MDU's between each sample, we could oversample high-probability areas of the integration curve and artificially reduce our statistical error estimation.

In order to detect whether autocorrelation is affecting our results, we monitor the variance on our observables. Once an observable is calculated on each configuration, the bootstrap or jackknife method is used to determine the final estimate of the variance. If we "rebin" the observable samples by averaging every N_{bin} samples to create a new set of samples and recalculate the variance, then the value and variance should remain the same if no autocorrelation is present. This is not something that can be easily estimated early on in the Markov chain as the precision of the observables also depends on the number of samples/configurations available. An example of autocorrelation effects is shown in Figure 2.3. In this figure, we see that the variance σ^2 for a given rebinning scheme increases with larger rebin. If we do find evidence of autocorrelation, then we rebin until the effects are negligible so that our statistical variance is accurately determined. Although at larger rebin values, finite-volume effects can affect our results which is indicated by a sudden jump in the χ^2 of our fit. In the case of Figure 2.3, $N_{\text{bin}} = 10$ was chosen due to its stability with $N_{\text{bin}} = 15$ and relatively small χ^2. Though $N_{\text{bin}} = 15$ had smaller χ^2, for similar results, less rebinning is always favored to minimize the reduction in statistics.

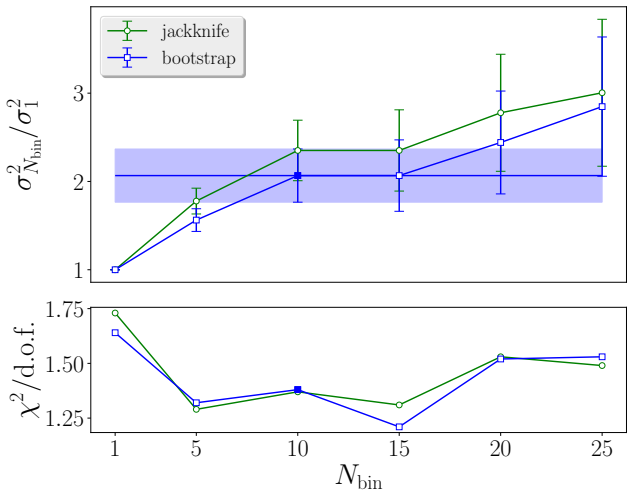

Figure 2.3: Rebinning analysis for the D200 ensemble. Figure taken from Reference [19]. *Top.* Relative variance of the pion rest mass determination for different rebinning schemes where the denominator corresponds to the variance with no rebinning ($N_{\text{bin}} = 1$). Both Jackknife and Bootstrap resampling methods were used to calculate the variance. The horizontal bar indicates the chosen rebin value for final results. *Bottom.* χ^2/d.o.f. of the corresponding fit results in the top figure.

Chapter 3

Constructing Correlators

The last section covered how the quark and gluon fields are generated in the Markov-Chain Monte Carlo method, but next, we need to construct correlation functions of the hadrons of interest out of the quark and gluon fields. Care needs to be taken to ensure that the necessary physics properties persist throughout our calculations. Once the hadronic operators have been built, we can then study their time-dependent correlation functions to compute the energy eigenvalues (spectrum) of the symmetry channel of interest.

3.1 Operator Construction

3.1.1 Smearing

We are only interested in the lowest energy modes of any given channel, so it is in our best interest to smear the fields in such a way that the hadronic operators constructed create states when acting on the QCD vacuum, which have minimal overlap with higher states while maintaining gauge covariance and other symmetries. In our framework, we couple to the lowest-lying states by smearing the gauge links using Stout smearing and the quark fields using LapH smearing.

Gauge Link Smearing (Stout Smearing)

Stout smearing, introduced and developed in Reference [29], can best be described as replacing a gauge link with a weighted sum over a set of perpendicular gauge link "staples" that connect to the same start and end points. This procedure is then performed on all gauge links some number of iterations until it is determined that the coupling to higher-energy states has been satisfactorily reduced. Stout smearing can be used for both the construction of the lattice action and for correlators. In some results, stout smearing has been used for both calculations, but in others, only the correlators.

As stated above, the smearing operator must respect the correct symmetries and physics, thus the weights for smearing are not computed randomly. When computed randomly, the smeared gauge links are no longer analytic or $SU(3)$ symmetric. If the smeared links are not analytic, then when computing gauge ensembles, the HMC algorithms are no longer applicable. If the smeared links are no longer $SU(3)$ symmetric, then they no longer represent physical gluon fields. When composing a method for smearing gauge links, it is critical to maintain these two features, and stout smearing accomplishes this.

To understand how stout smearing is applied, first we write down a sum of all perpendicular staples,

$$C_\mu(x) = \sum_{\nu\neq\mu} \rho_{\mu\nu}\Big(U_\nu(x)U_\mu(x+\hat{\nu})U_\nu^\dagger(x+\hat{\mu}) + U_\nu^\dagger(x-\hat{\nu})U_\mu(x-\hat{\nu})U_\nu(x-\hat{\nu}+\hat{\mu})\Big),$$

where $\hat{\mu}, \hat{\nu}$ are vectors of one lattice unit length in directions μ, ν, respectively. Notice that weights are applied to opposing staples equally (each term in the sum is a different staple). This is not necessary for the solution, and a different basis for the weights is allowed. Using Lie algebra, we can build a Hermitian traceless generator of $SU(N)$, $Q_\mu(x)$, if we apply the formula,

$$Q_\mu(x) = \frac{i}{2}\Big(\Omega_\mu^\dagger(x) - \Omega_\mu(x)\Big) - \frac{i}{2N}\,\mathrm{Tr}\Big(\Omega_\mu^\dagger(x) - \Omega_\mu(x)\Big), \tag{3.1}$$

where

$$\Omega_\mu(x) = C_\mu(x)\; U_\mu^\dagger(x) \quad \text{(no summation over } \mu\text{)}. \tag{3.2}$$

Because $Q_\mu(x)$ is Hermitian and traceless, this means that $\exp(iQ_\mu(x))$ is an element of $SU(N)$ Lie group. With this fact, an iterative and analytic smearing method can be computed as

$$U_\mu^{(n+1)}(x) = \exp\Big(iQ_\mu^{(n)}(x)\Big)\; U_\mu^{(n)}(x) \tag{3.3}$$

where n indicates the number of iterations where this smearing method has been applied to all links, indicating that $U_\mu^{(0)}(x) \equiv U_\mu(x)$ and $\exp(iQ_\mu(x))$ is the smearing coefficient applied each iteration. With the choice of $N = 3$, both $\exp(iQ_\mu(x))$ and $U_\mu^{(n)}(x)$, enforcing that $U_\mu^{(n+1)}(x)$ is also within $SU(3)$. A visualization of the first-order expansion of $\exp(iQ_\mu(x))$.

With this definition, we see that the choice in weights $\rho_{\mu\nu}$ is *somewhat* arbitrary. When computing correlators we set the weights as $\rho_{4\nu} = \rho_{\mu 4} = 0$. We do not want smearing in the temporal direction for computing temporal correlators, as we want to ensure that the hadronic operator only includes fields from a single time slice. The choices for the remaining elements of $\rho_{\mu\nu}$ are $\rho_{jk} = \rho$.

Further details on how $\exp(iQ_\mu(x))$ is approximated can be found in Reference [29].

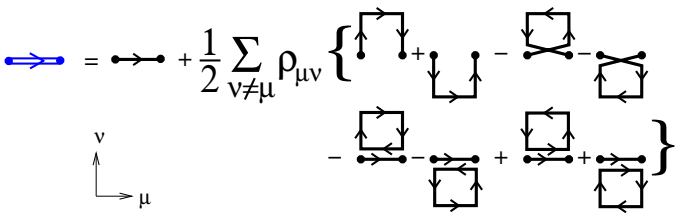

Figure 3.1: Diagramatic representation of the first order expansion of equation 3.3.

Quark Field Smearing (LapH Smearing)

To further reduce the coupling of our measured observables to higher-energy modes of the system, Laplacian-Heaviside (LapH) smearing is applied to the quark fields [3, 4]. For discretized space, to compute the second derivative, the central difference formula is used. The definition of the central difference formula is equivalent to a weighted sum of neighbors for any set of positions x, y, i.e. a smoothing function. For our cases, we begin with the gauge-covariant Laplacian matrix on the lattice,

$$\begin{aligned}\widetilde{\Delta}^{ab}(x,y;U) = \sum_{k=1}^{3}\Big\{&\widetilde{U}_k^{ab}(x)\delta(y,x+\hat{k}) \\ &+\widetilde{U}_k^{ba}(y)^*\delta(y,x-\hat{k}) - 2\delta(x,y)\delta^{ab}\Big\},\end{aligned} \tag{3.4}$$

where $\widetilde{U}$ represents the stout-smeared gauge fields. Although we now have a methodology for smearing, a simple second-order derivative will not reduce the coupling to higher modes. What the operator can do is indicate the higher modes by studying the N_Δ eigenvalues of Laplacian matrix. We diagonalize the Laplace operator so that

$$\widetilde{\Delta} = V_\Delta\ \Lambda_\Delta\ V_\Delta^\dagger. \tag{3.5}$$

where Λ_Δ is a matrix of the eigenvalues along the diagonal, and V_Δ contains the corresponding eigenvectors. The larger-valued eigenvalues correspond to the higher-energy modes of the system and we can decouple from those modes by generating a smearing matrix,

$$\mathcal{S} = V_\Delta\ \Theta\left(\sigma_s^2 + \Lambda_\Delta\right)\ V_\Delta^\dagger, \tag{3.6}$$

that applies a Heaviside function with a tunable upper threshhold σ_s^2 for the eigenvalues of $\widetilde{\Delta}$ and removes the contribution of higher eigenvalues from the matrix. This matrix can then be applied to the quark fields to produce LapH-smeared quark fields,

$$\widetilde{\psi}_{a\alpha}(x) = \mathcal{S}_{ab}(x,y)\ \psi_{b\alpha}(y). \tag{3.7}$$

To determine the cutoff σ_s^2, an effective mass is measured at an early time for various σ_s^2 and the minimum value is chosen. Not only are undesired couplings to the higher

modes removed as shown in Reference [3], but by using eigenvalues of the gauge-covariant Laplacian, we maintain the necessary symmetries and quantum numbers in the smeared quark fields.

3.1.2 Relevant Quantum Numbers

Identifying the quantum numbers of any particle is equivalent to identifying its transformation properties under various symmetries. On the lattice those symmetries are reduced but still provide vital information for computing continuum-scattering results. The relevant symmetries we consider are outlined in this section.

Rotational symmetry

In continuum quantum mechanics, stationary states of a system are characterized by angular momentum, but on the hypercubic lattice, we are confined to ninety-degree rotations in spacetime. The $SO(3)$ rotation group is not a symmetry group of the lattice gauge theory, only a subset of it is. As realized by Johnson et al. in Reference [30], the octahedral group [31] provides an adequate symmetry group for the lattice. More often used in crystalline physics, the irreducible representations (irreps) of the octahedral group will provide us with a new quantum number which the continuum angular momentum can be mapped onto.

Integer values of the angular momentum can be mapped onto states of the octahedral group, which contains 24 elements in five conjugacy classes. The conjugacy classes and descriptions of their symmetries are listed in Table 3.1. The conjugacy classes are labeled as nC_m where each of the n elements is a m-th root of the identity.

The irreps we use are related to the conjugacy classes according to Table 3.2. Vector representations of $SO(3)$ ($j = 0, 1, 2, ...$) map onto these irreps.

Spin

To incorporate spin in the irreducible representation, we will instead use the double cover of the octahedral group, ${}^2O$. ${}^2O$ includes all elements of O with the addition of all elements of O multiplied by negative identity J. Naturally, all elements and irreps involved with O are contained within ${}^2O$ as well as three new conjugacy groups equivalent to 24 more elements. The three new conjugacy classes arise from C_3 and C_4 and J. The new irreps map to the conjugacy classes according to table 3.3, and $SU(2)$ representations ($j = 1/2, 3/2, ...$) map onto the new irreps that arise out of ${}^2O$.

Parity

To incorporate parity, spatial inversions I_s can be applied to both O and ${}^2O$. When spatial inversions are included in either of these groups, it doubles their size and they

Class	Description	Diagram
I	identity	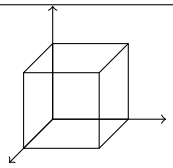
$3C_2$	π rotations about 3 coordinate axes	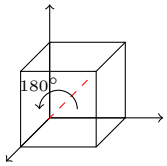
$8C_3$	$\pm(2\pi/3)$ about the body diagonals	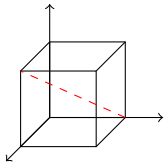
$6C_4$	$\pm\pi/2$ rotations about 3 coordinate axes	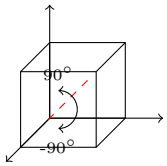
$6C_2$	π rotations about the face diagonals	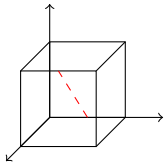

Table 3.1: Descriptions and example diagrams of the symmetries of the 5 conjugacy classes of the octahedral point group. The red dotted line indicates the axis of rotation. For classes with the same axes, the included rotations are also noted in the diagram.

	I	$3C_2$	$8C_3$	$6C_4$	$6C_2$
A_1	1	1	1	1	1
A_2	1	1	1	-1	-1
E	2	2	-1	0	0
T_1	3	-1	0	-1	1
T_2	3	-1	0	1	-1

j	irreps j appears in
0	A_1
1	T_1
2	$E + T_2$
3	$A_2 + T_1 + T_2$
...	

Table 3.2: Mappings of irreducible representations of the octahedral point group. *Left.* Coefficient of each symmetry group for the irreducible representations. *Right.* Mapping of angular momentum on irreducible representations.

are denoted by O_h and ${}^2O_h$. To indicate the spatial-inversion symmetry in the irreps, an additional label g or u is added to the subscript of the irrep. From the German words *gerade* and *ungerade*, g and u indicate positive and negative parity respectively.

	I	J	$6C_4$	$8C_3$	$8C_6$	$6C_8$	$6C_8'$	$12C_4'$
G_1	2	-2	0	-1	1	$-\sqrt{2}$	$\sqrt{2}$	0
G_2	2	-2	0	-1	1	$\sqrt{2}$	$-\sqrt{2}$	0
H	4	-4	0	1	-1	0	0	0

j	irreps j appears in
1/2	G_1
3/2	H
5/2	$G_2 + H$
...	

Table 3.3: Mappings of irreducible representations of the double cover of the octahedral point group. *Left.* Coefficient of each symmetry group for the additional irreducible representations of ${}^2O$. The rest are outlined in Table 3.2. *Right.* Mapping of spin on irreducible representations.

Flavor symmetry

Out of all the three smallest mass quarks, m_u and m_d are the only quarks with similar masses as is shown in Figure 3.2, and thus, in our simulations we set $m_u = m_d$ to give us an exact $SU(2)$ flavor symmetry. To avoid mixing between states of definite

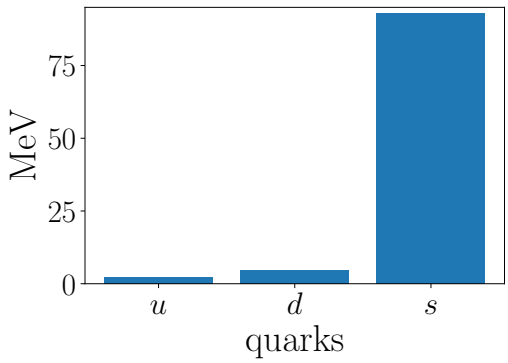

Figure 3.2: A comparison of the three lightest quark masses. Values were collected from the PDG [9].

isospin, we establish a $SU(2)$ multiplet for each of our operators with u and d as two different states. This doublet is called isospin, I, symmetry with $I_3 = +1/2$ for the u flavor state and $I_3 = -1/2$ for the d flavor state where I_3 is the projection onto the z-axis in isospin space. The isospin doublet mathematically functions the same as spin, but does not relate to spin, physical space, or angular momentum.

The $SU(2)$ isospin rotation can be written as

$$U_{R_\tau} = \exp(-i\varphi \cdot \tau), \tag{3.8}$$

where φ is the rotation vector, and τ is a vector of the three generators of isospin rotations. The hadronic operators, $\overline{O}^{(I)}_{I_3}$ and $O^{(I)}_{I_3}$, must maintain this symmetry by demanding the following transformation properties,

$$U_{R_\tau} \overline{O}^{(I)}_{I_3} U^\dagger_{R_\tau} = \sum_{I_3'} \overline{O}^{(I)}_{I_3'} D^{(I)}_{I_3', I_3}(R_\tau) \tag{3.9}$$

and

$$U_{R_\tau} O^{(I)}_{I_3} U^\dagger_{R_\tau} = \sum_{I'_3} O^{(I)}_{I'_3} D^{(I)}_{I'_3, I_3}(R_\tau)^*, \tag{3.10}$$

where $D^{(I)}(R_\tau)$ are the Wigner rotation matrices.

G-parity

For electrically/flavor-neutral meson states, charge conjugation is another good quantum number. Charge conjugation is the behavior of the state when the quarks are replaced with their anti-quark partners. Only some electrically/flavor-neutral meson states (including tetraquark states) are eigenstates of their conjugation (for example, $\mathcal{C}|\pi^0\rangle = +|\pi^0\rangle$ where $\mathcal{C}$ is the charge-conjugation operator). The strong force is blind to electromagnetic charge, so differentiating states like π^+, π^0, π^- comes down to the isospin of the light quark to differentiate up and down. Instead of charge conjugation alone, we can use G-parity which is a combination of the charge conjugation and a rotation in isospin space,

$$U_G = \mathcal{C} e^{-i\pi\tau_2}. \tag{3.11}$$

Moving Frames

To generate irreps with definite momentum, the representation of ${}^2O_h$ is considered combined with a translational element. The moving irreps must maintain the rotational symmetry along the line of translation. These translations are summarized in the little group of $\mathbf{p}$, where $\mathbf{p}$ is the lattice momentum vector. To define the new conjugacy classes for the moving irreps, we subduce the representations of ${}^2O_h$ onto the little group $\mathbf{p}$. For $\mathbf{p} = (0,0,0)$, this includes all representations of ${}^2O_h$. The conjugacy classes and subductions for different basic lattice momenta are outlined in Tables 3.4-3.6.

$\mathbf{p} = (0,0,1)$		
C_{4v} classes	subduced O_h representations	description
$\mathcal{C}_1$	$\{I\}$	identity
$\mathcal{C}_2$	$\{C_{2z}\}$	π rotations about the z axes
$\mathcal{C}_3$	$\{C_{4z}, C_{4z}^{-1}\}$	$\pm\pi/2$ rotations about the z axes
$\mathcal{C}_4$	$\{I_s C_{2x}, I_s C_{2y}\}$	π rotation combined with spatial inversion about the x and y axes
$\mathcal{C}_5$	$\{I_s C_{2a}, I_s C_{2b}\}$	π rotation combined with spatial inversion about the $x = y$ and $x = -y$ axes

Table 3.4: Subduction of conjugacy classes from ${}^2O_h$ onto little group $\mathbf{p} = (0,0,1)$ with descriptions of the symmetries.

$\mathbf{p} = (0,1,1)$		
C_{2v} classes	subduced O_h representations	description
$\mathcal{C}_1$	$\{I\}$	identity
$\mathcal{C}_2$	$\{C_{2e}\}$	π rotations about the $z = y$ axis
$\mathcal{C}_3$	$\{I_s C_{2f}\}$	π rotation combined with spatial inversion about the $z = -y$ axis
$\mathcal{C}_4$	$\{I_s C_{2x}\}$	π rotation combined with spatial inversion around the x axis

Table 3.5: Subduction of conjugacy classes from ${}^2O_h$ onto little group $\mathbf{p} = (0,1,1)$ with descriptions of the symmetries.

$\mathbf{p} = (1,1,1)$		
C_{3v} classes	subduced O_h representations	description
$\mathcal{C}_1$	$\{I\}$	identity
$\mathcal{C}_2$	$\{C_{3\delta},\, C_{3\delta}^{-1}\}$	$\pm(2\pi/3)$ about the $x = y = z$ axis
$\mathcal{C}_3$	$\{I_s C_{2b},\, I_s C_{2d},\, I_s C_{2f}\}$	π rotation combined with spatial inversion about the $x = -y$, $x = -z$, and $z = -y$ axes

Table 3.6: Subduction of conjugacy classes from ${}^2O_h$ onto little group $\mathbf{p} = (1,1,1)$ with descriptions of the symmetries.

When we reference irreps later on, we will often use the notation $\Lambda(\boldsymbol{d^2})$ where Λ refers to the irrep and $\boldsymbol{d}$ refers to the lattice momentum.

3.1.3 Elemental Single-Hadron Operators

Before we enforce any quantum numbers on the operators, next we will construct the basic elemental hadronic operators out of the smeared quark and gluon fields.

Displacements

In order to include radial and orbital effects in our correlators, some of the hadron operators must be distended in space. In order to do that, we define a gauge-covariant displacement operator in the j^{th} direction by,

$$\widetilde{D}_j^{(p)}(x,x') = \widetilde{U}_j(x)\widetilde{U}_j(x+\hat{j})\ldots\widetilde{U}_j(x+(p-1)\hat{j})\delta_{x',x+p\hat{j}}, \tag{3.12}$$

where $p > 0$ indicates the number of steps in that direction. For ease of writing the hadron operators, $p = 0$ is included to indicate no displacement ($\widetilde{D}_j^{(0)}(x,x') = \delta_{x',x}$).

Elemental Simple-Meson Operators

Although mesons are defined as any color singlet state with the same number of quarks and antiquarks, in this work we will only study mesons of one or two quark-antiquark ($q\bar{q}$) pairs. To distinguish between these types of mesons, the single $q\bar{q}$ particle will be considered the *simple mesons* or just *mesons*. Particles of two $q\bar{q}$ pairs are called *tetraquarks*.

To begin constructing our meson operator, let us look at an operator made from our smeared quark fields,

$$\tilde{\chi}^A_{a\alpha}\tilde{\psi}^B_{b\beta}, \tag{3.13}$$

where $\chi = \overline{\psi}\gamma_4$, capital Latin superscripts indicate flavor, Greek subscripts indicate Dirac spin, and a, b, c, d indicate color. In order to create an operator that represents a physical meson, the final operator must be color-singlet i.e. gauge-invariant. The only way to produce this in a meson operator is a delta function between color indices,

$$\delta_{ab}\tilde{\chi}^A_{a\alpha}\tilde{\psi}^B_{b\beta}. \tag{3.14}$$

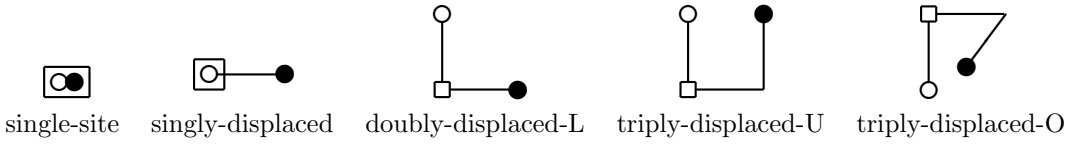

Figure 3.3: Diagrammatic depiction of meson displacements, taken from Reference [32]. All diagrams are planar except for triply-displaced-O, for which the diagonal line represents projection into the third spatial dimension. The solid circles indicate the final position of the quark, the hollow circles indicate the final position of the antiquark, and the hollow square indicates the assignment of the meson operator location.

At this point, we have not considered the spatial component of these quark fields. The fields may be separated from each other. Because we do not know the spatial displacements of quarks within a meson, many displacements of the meson operators were studied and are identified in Figure 3.3. For displacements that span multiple dimensions, the magnitudes of displacements in the different dimensions are the same, but varying magnitudes are studied. An operator with these displacements can be written as

$$\delta_{ab}\left(\tilde{\chi}D_i^{(p)\dagger}\right)^A_{a\alpha}\left(D_j^{(p)}D_k^{(p)}\tilde{\psi}\right)^B_{b\beta}, \tag{3.15}$$

where p is the magnitude of the displacement if not zero and i, j, k represent spatial directions. The magnitude p for each displacement is chosen to achieve the configurations in Figure 3.3.

Rather than studying a meson operator with definite location, we would like to study a meson operator with definite momentum, so we apply a discrete Fourier

transform to our elemental meson and antimeson operators,

$$\Phi^{AB}_{\alpha\beta;ijk}(\boldsymbol{p},t) = \sum_{x} e^{-i\boldsymbol{p}(\boldsymbol{x}+\frac{1}{2}(\boldsymbol{d}_a+\boldsymbol{d}_b))}\delta_{ab}\left(\tilde{\chi}D^{(p)\dagger}_i\right)^{A}_{a\alpha}(\boldsymbol{x},t)\left(D^{(p)}_j D^{(p)}_k\tilde{\psi}\right)^{B}_{b\beta}(\boldsymbol{x},t), \quad (3.16)$$

and

$$\overline{\Phi}^{AB}_{\alpha\beta;ijk}(\boldsymbol{p},t) = \sum_{x} e^{i\boldsymbol{p}(\boldsymbol{x}+\frac{1}{2}(\boldsymbol{d}_a+\boldsymbol{d}_b))}\delta_{ab}\left(\tilde{\chi}D^{(p)\dagger}_k D^{(p)\dagger}_j\right)^{B}_{b\beta}(\boldsymbol{x},t)\left(D^{(p)}_i\tilde{\psi}\right)^{A}_{a\alpha}(\boldsymbol{x},t), \quad (3.17)$$

where $\boldsymbol{p}$ is the definite momentum, and $\boldsymbol{d}_{a,b}$ are the total displacements of the quark and antiquark fields. To be able to project the correct behavior of the meson operators under G-parity, the displacements are included in the phase factor. The annihilation operators and their quantum numbers for the mesons used in our simulations are outlined in Table 3.7.

Name	I	I_3	S	G	Annihilation Operator
$\eta_{\alpha\beta}$	0	0	0	1	$\Phi^{uu}_{\alpha,\beta} + \Phi^{dd}_{\alpha,\beta}$
$\phi_{\alpha\beta}$	0	0	0	-1	$\Phi^{ss}_{\alpha,\beta}$
$\pi^{+}_{\alpha\beta}$	1	1	0	-1	$\Phi^{du}_{\alpha,\beta}$
$K^{+}_{\alpha\beta}$			1		$\Phi^{su}_{\alpha,\beta}$
$\overline{K}^{0}_{\alpha\beta}$			-1		$\Phi^{ds}_{\alpha,\beta}$
$\pi^{0}_{\alpha\beta}$	1	0	0	-1	$\Phi^{dd}_{\alpha,\beta} - \Phi^{uu}_{\alpha,\beta}$
$\pi^{-}_{\alpha\beta}$	1	-1	0	-1	$\Phi^{ud}_{\alpha,\beta}$
$K^{0}_{\alpha\beta}$		$-$	-1		$\Phi^{sd}_{\alpha,\beta}$
$\overline{K}^{-}_{\alpha\beta}$		$-$	1		$\Phi^{us}_{\alpha,\beta}$

Table 3.7: Final meson annihilation operators after projecting onto definite G-parity. First flavor index of the operator indicates the antiquark and second index, the quark. Particle names indicate the flavor structure and may not reflect the real particles, which may have a more complicated flavor composition.

Elemental Baryon Operators

The baryon operator is constructed in a similar manner as the simple meson operator except that the baryon operator is constructed out of three quark fields. To create a color singlet state, the Levi-Civita coupling is used in place of the delta function. The elemental baryon and antibaryon operators are then written as

$$\Phi^{ABC}_{\alpha\beta\gamma;ijk}(\boldsymbol{p},t) = \sum_{x} e^{-i\boldsymbol{p}\boldsymbol{x}}\varepsilon_{abc}\tilde{\psi}^{A}_{a\alpha i}(\boldsymbol{x},t)\tilde{\psi}^{B}_{b\beta j}(\boldsymbol{x},t)\tilde{\psi}^{C}_{c\gamma k}(\boldsymbol{x},t) \quad (3.18)$$

and

$$\overline{\Phi}^{ABC}_{\alpha\beta\gamma;ijk}(\boldsymbol{p},t) = \sum_{x} e^{i\boldsymbol{p}\boldsymbol{x}}\varepsilon_{abc}\tilde{\chi}^{C}_{c\gamma k}(\boldsymbol{x},t)\tilde{\chi}^{B}_{b\beta j}(\boldsymbol{x},t)\tilde{\chi}^{A}_{a\alpha i}(\boldsymbol{x},t), \quad (3.19)$$

where

$$\tilde{\psi}^A_{a\alpha i}(\boldsymbol{x},t) = \left(D^{(p)}_i \tilde{\psi}\right)^A_{a\alpha}(\boldsymbol{x},t) \text{ and } \tilde{\chi}^A_{a\alpha i}(\boldsymbol{x},t) = \left(\tilde{\chi} D^{(p)\dagger}_i\right)^A_{a\alpha}(\boldsymbol{x},t). \tag{3.20}$$

The displacement operators function the same as for the mesons, but the configurations investigated are outlined in Figure 3.4. In this case, the displacement vectors were not included in the phase of the momentum projection because G-parity is not a quantum number of baryons, and thus there is no need to project onto it. The quantum numbers and quark makeup of the relevant baryon operators are outlined in Table 3.8.

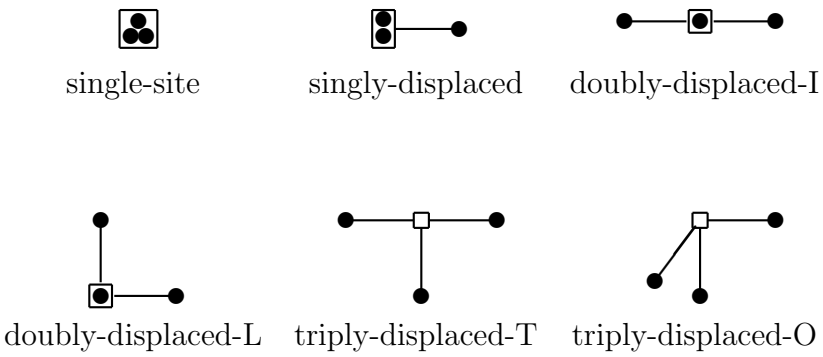

Figure 3.4: Diagrammatic depiction of baryon displacements, taken from Reference [33]. Similarly to baryon displacements, all diagrams are planar except for triply-displaced-O, for which the diagonal line represents projection into the third spatial dimension. Solid circles indicate the final position of the quark and the hollow square indicates the assignment of the baryon operator location.

Hadron	$I = I_3$	S	G	Annihilation Operators
Δ^{++}	$\frac{3}{2}$	0		$\Phi^{uuu}_{\alpha\beta\gamma}$
Σ^+	1	-1		$\Phi^{uus}_{\alpha\beta\gamma}$
N^+	$\frac{1}{2}$	0		$\Phi^{uud}_{\alpha\beta\gamma} - \Phi^{duu}_{\alpha\beta\gamma}$
Λ^0	0	-1		$\Phi^{uds}_{\alpha\beta\gamma} - \Phi^{dus}_{\alpha\beta\gamma}$

Table 3.8: Maximal-I_3 baryons and their corresponding elemental annihilation operators.

Elemental Tetraquark Operators

The only way to create color singlet objects with four quarks is for there to be an equal number of quarks and antiquarks. In this case, there are two linearly independent ways to construct tetraquark operators: $\bar{q}_a q_a \bar{q}_b q_b$ and $\bar{q}_a q_b \bar{q}_b q_a$ where a, b indicate

color, resulting in two linearly independent gauge-invariant elemental tetraquark and anti-tetraquark operators:

$$\Phi^{ABCD\pm}_{\alpha\beta\mu\nu;ijkl}(\boldsymbol{p},t) = \sum_{x} e^{-i\boldsymbol{p}\boldsymbol{x}}(\delta_{ab}\delta_{cd} \pm \delta_{ad}\delta_{bc})\tilde{\chi}^{A}_{a\alpha i}(\boldsymbol{x},t)\tilde{\psi}^{B}_{b\beta j}(\boldsymbol{x},t)\tilde{\chi}^{C}_{c\mu k}(\boldsymbol{x},t)\tilde{\psi}^{D}_{d\nu l}(\boldsymbol{x},t) \tag{3.21}$$

and

$$\overline{\Phi}^{ABCD\pm}_{\alpha\beta\mu\nu;ijkl}(\boldsymbol{p},t) = \sum_{x} e^{-ipx}(\delta_{ab}\delta_{cd} \pm \delta_{ad}\delta_{bc})\tilde{\chi}^{D}_{d\nu l}(\boldsymbol{x},t)\tilde{\psi}^{C}_{c\mu k}(\boldsymbol{x},t)\tilde{\chi}^{B}_{b\beta j}(\boldsymbol{x},t)\tilde{\psi}^{A}_{a\alpha i}(\boldsymbol{x},t), \tag{3.22}$$

where fields have been replaced with the displaced fields described in Equation 3.20. The displacements studied for the tetraquark operators are outlined in Figure 3.5.

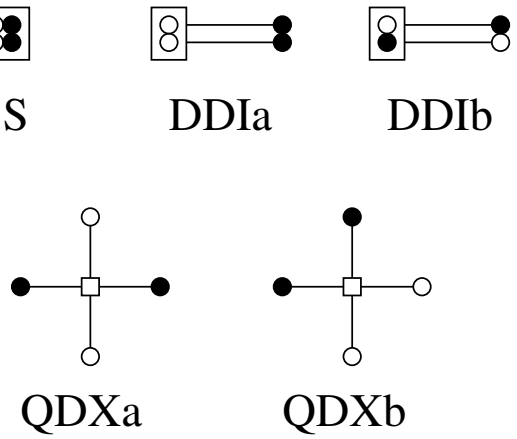

Figure 3.5: Diagrammatic depiction of tetraquark displacements, taken from Reference [33]. Solid circles indicate the final position of the quark, hollow circles indicate the final position of the anti-quark, and the hollow square indicates the assignment of the tetraquark operator location.

3.1.4 Single-Hadron Operators

The elemental single-hadron operators by their construction have some quantum numbers, such as Dirac spin, definite flavor, displacements, and momentum, but the hadrons of interest have quantum numbers associated with rotational symmetry instead of Dirac spin. Not only that, some meson operators also have G-parity. Therefore, we need to construct operators from the elemental single-hadron operators that represent the quantum numbers that we want to study. For any of the elemental operators listed in the previous section, the new operators are constructed in the form

$$\mathcal{O}_l(\boldsymbol{p},t) = c^{(l)}_{\alpha\beta\ldots}\Phi^{AB\ldots}_{\alpha\beta\ldots;ijk}(\boldsymbol{p},t), \tag{3.23}$$

and

$$\overline{\mathcal{O}}_l(\boldsymbol{p},t) = c^{(l)*}_{\alpha\beta\ldots}\overline{\Phi}^{AB\ldots}_{\alpha\beta\ldots;ijk}(\boldsymbol{p},t), \tag{3.24}$$

where $c^{(l)}_{\alpha\beta\ldots}, c^{(l)*}_{\alpha\beta\ldots}$ are the weights and l incorporates all of the relevant quantum numbers. Enforcing these quantum numbers is equivalent to computing an operator that transforms according to the corresponding symmetry group. To find the correct coefficients, we enforce that the operators transform according to the λ row of the Λ irreducible representation of a symmetry transformation R. In order to construct this operator, we know that if the operators transform according to the irrep row, $\overline{\mathcal{O}}^{\Lambda\lambda}$ and $\mathcal{O}^{\Lambda\lambda}$, they must satisfy the conditions:

$$U_R \mathcal{O}^{\Lambda\lambda} U_R^\dagger = \sum_\mu \mathcal{O}^{\Lambda\mu} \Gamma^{(\Lambda)}_{\mu\lambda}(R)^* \tag{3.25}$$

and

$$U_R \overline{\mathcal{O}}^{\Lambda\lambda} U_R^\dagger = \sum_\mu \overline{\mathcal{O}}^{\Lambda\mu} \Gamma^{(\Lambda)}_{\mu\lambda}(R), \tag{3.26}$$

where U_R is the unitary quantum operator associated with R and $\Gamma^{(\Lambda)}(R)$ is the matrix of the symmetry transformation R in the Λ irreducible representation. With this condition, we can write out how the correlators should be constructed,

$$\mathcal{O}^{\Lambda\lambda} = \frac{d_\Lambda}{g_\mathcal{G}} \sum_{R\in\mathcal{G}} \Gamma^{(\Lambda)}_{\lambda\mu}(R) U_R \mathcal{O} U_R^\dagger \tag{3.27}$$

and

$$\overline{\mathcal{O}}^{\Lambda\lambda} = \frac{d_\Lambda}{g_\mathcal{G}} \sum_{R\in\mathcal{G}} \Gamma^{(\Lambda)*}_{\lambda\mu}(R) U_R \overline{\mathcal{O}} U_R^\dagger \tag{3.28}$$

where d_Λ is the dimension of Λ, R are the elements of the group $\mathcal{G}$, $g_\mathcal{G}$ is the order of $\mathcal{G}$, and all other indices have been suppressed. The index μ is arbitrary, though only $\mu = \lambda$ guarantees true projection. Because this equation does not enforce a phase or weight, the coefficients have enough flexibility to satisfy both this condition and produce an equivalent operator for different values of μ. Therefore, we can sum over the irrep rows of the resulting correlators to increase statistics.

3.1.5 Multi-Hadron Operators

Constructing multi-hadron operators is fairly straightforward once the single-hadron operators have been properly constructed. The same quantum numbers needed for the single-hadron apply to all multi-hadron operators. To construct a two-hadron operator, a first attempt may be a mere product of the two single-hadron operators. Although individual operators have been designed to conform to the quantum numbers of interest, their product does not have this guarantee. Therefore, similarly to the single-hadron, we make a linear combination of the operator products that adheres to all the symmetry requirements of the previous section for the interacting channel of interest. This is precisely what makes the tetraquark fundamentally different from

a two-hadron operator. The $\bar{q}q$ product fields within the tetraquark operator are not projected onto any symmetries.

Though multihadron operators can include any number of hadrons, only single- and two-hadron operators are considered in this thesis. The Lüscher formalism for retrieving the scattering information from the finite-volume spectrum as described in this work is only valid below the three-particle threshold. The formalism for three-particle scattering is making strides, but is outside the scope of this work.

3.2 Quark Propagator Construction

As shown earlier, the fermionic parts of the correlator can be analytically integrated over, though it does leave a Dirac matrix inversion in the gluon field integration. This Dirac matrix inversion is the most expensive part of the correlator computation. It has indices of spacetime, color, and Dirac spin, so for a theory of three colors and four Dirac indices on a $32^3 \times 256$ lattice, this amounts to a complex-valued matrix of size $\sim 10^8 \times 10^8$. Storing this matrix at double precision would amount to about 160 petabytes. Thus, computing the Dirac matrix and its inverse is done on the fly, and to speed things up, there are methods of stochastically estimating this inverse to greatly reduce computation.

Quark Lines

Evaluating temporal correlators with hadronic operators involves an integration of a product of quark propagators, the connecting lines between creation and annihilation operators in Feynman diagrams. On the lattice, a quark propagator is called a quark line. There are several basic categories of the quark lines: forward-time quark line, backward-time quark line, and same-time quark line. The same-time quark lines contribute to disconnected diagrams and represent sea quarks. As stated before, these have been found to be essential to medium-energy scattering results.

To understand how quark lines are computed on the lattice, I will review Monte Carlo integration. Recall from Chapter 2 that analytical integration over fermionic fields gave us Equation 2.19. This means that calculating any observable requires computing the inverse Dirac matrix. For example, the fermionic integration over a set of meson operators results in,

$$\int \mathcal{D}[\overline{\psi}, \psi] \psi_a \psi_b \overline{\psi}_c \overline{\psi}_d \exp\left(-\overline{\psi}^T D \psi\right) = \left(D^{-1}_{ad} D^{-1}_{bc} - D^{-1}_{ac} D^{-1}_{bd}\right) \det D, \tag{3.29}$$

where D is the Dirac matrix. From this point on, for convenience, $\chi \equiv \bar{\psi}\gamma_4$ and $\Omega = \gamma_4 D$. This will help reduce the confusion between the displacement operator and the Dirac matrix and make it easier to construct hermitian baryon matrices.

With smearing $\mathcal{S}$ and displacements D, a forward-time quark line is defined as

$$Q_{jk}(t, t_0) = D_j \mathcal{S} \Omega^{-1}(t, t_0) \mathcal{S} D^\dagger_k. \tag{3.30}$$

From this definition, we can easily obtain the backward-

$$\overline{Q}_{jk}(t,t_0) = (\gamma_5\gamma_4 Q_{jk}(t,t_0)\,\gamma_4\gamma_5)^* = -Q_{kj}(t_0,t) \tag{3.31}$$

and same-time ($Q_{jk}(t,t)$) quark lines.

Stochastic Estimation

When applying the Fourier transform to the operators to project into momentum space, the computation time increases dramatically with more hadrons involved. When computing single-hadron correlators, translational invariance can be used to reduce calculations or increase statistics, but as soon as there are nonzero-momentum multi-hadron operators or disconnected multi-hadron operators, this trick no longer works. To improve computation time without sacrificing the accuracy of the results, another trick has been found instead: inserting stochastic noise. Because the variance is dominated by statistical noise, inverses do not need to be computed exactly. We can control the uncertainty by combining the noise and the dilutions of that noise.

To understand how this works, consider an $N \times N$ complex matrix M for which we would like to stochastically compute the inverse. First, we introduce a noise vector, η, that satisfies expectations $E(\eta_i) = 0$ and $E(\eta_i \eta_j^*) = \delta_{ij}$ where E is the standard expectation function. Next, we solve the function $MX = \eta$ for the vector X. With a set of X, we can arrive at the following conclusion:

$$E\left(X_i \eta_j^*\right) = E\left(\sum_k M_{ik}^{-1} \eta_k \eta_j^*\right) = \sum_k M_{ik}^{-1} E\left(\eta_k \eta_j^*\right) = \sum_k M_{ik}^{-1} \delta_{kj} = M_{ij}^{-1}. \tag{3.32}$$

And thus M_{ij}^{-1} can be estimated as

$$M_{ij}^{-1} \approx \lim_{N_R \to \infty} \frac{1}{N_R} \sum_{r=1}^{N_R} X_i^{(r)} \eta_j^{(r)*}, \quad \text{where } MX^{(r)} = \eta^{(r)}. \tag{3.33}$$

Using this method alone is not sensible for application. In order to compute the exact solution for the Dirac matrix inverse, one would need to sample over infinite noise vectors. Even if one were to choose $N_R < N$ noise vectors, the variance is too large to be useful. However, if the noise vectors are engineered in such a way that the exact solution is achieved in the limit $N_R \to N$ instead of $N_R \to \infty$, this method is very useful. The strategy used to accomplish this is called *dilution*, and it begins with the decomposition of a given noise vector into a sum of vectors where each decomposed vector $\eta_j^{(r)[s]}$ contains only the s-th element of the original vector $\eta_j^{(r)}$ and all other elements are zero.

$$\eta_j^{(r)} = \sum_{s=1}^{N} \eta_j^{(r)[s]}, \quad \eta_j^{(r)[s]} = \eta_j^{(r)} \delta_{js} \quad (\text{ no sum over } j). \tag{3.34}$$

If this decomposition is used instead, then by following the same steps as above, we find the following equation is produced,

$$\begin{aligned}\sum_{s=1}^{N} X_i^{(r)[s]} \eta_j^{(r)[s]*} &= \sum_s M_{is}^{-1} \eta_s^{(r)} \eta_j^{(r)[s]*} \\ &= \sum_s M_{is}^{-1} \eta_s^{(r)} \eta_j^{(r)*} \delta_{sj} \\ &= M_{ij}^{-1} \eta_j^{(r)} \eta_j^{(r)*}, \quad (\text{ no sum over } j),\end{aligned} \tag{3.35}$$

where $X^{(r)[s]}$ is the solution of $MX^{(r)[s]} = \eta^{(r)[s]}$. From this equation, it is clear to see that if the original noise vector has the property $\eta_j^{(r)} \eta_j^{(r)*} = 1$, then the inverse is calculated exactly with only N decomposed noise vectors of one unit modulus noise vector.

Using maximal dilution does not improve the computation cost of inverting the Dirac matrix, but if not all decomposed noise vectors are used, a low-variance, accurate Dirac matrix can be achieved, which is shown in Reference [4]. Maximal dilution ensures that many of the elements are exact zeros rather than statistical zeros, and that all of the diagonal elements are exact. For later convenience, we can introduce a new entity, dilution projection matrices, that convert the noise vector to a diluted noise vector

$$\eta^{[a]} = P^{(a)} \eta. \tag{3.36}$$

Quark sources and sinks

By stochastically estimating the inverse of the Dirac matrix, we are allowed to split the quark line into two parts: quark sources and quark sinks. Take the original definition of the quark line, Equation 3.30,

$$Q_{jk}(t, t_0) = D_j \mathcal{S} \Omega^{-1}(t, t_0) \mathcal{S} D_k^\dagger.$$

Using the noise vector properties written in matrix form, $E(\eta) = 0, \quad E\left(\eta\eta^\dagger\right) = I$, we can rewrite the quark line as such

$$\begin{aligned}Q_{jk} &= D_j \mathcal{S} \Omega^{-1} E\left(\eta\eta^\dagger\right) \mathcal{S} D_k^\dagger \\ &= E\left(D_j \mathcal{S} \Omega^{-1} \eta \left(D_k \mathcal{S} \eta\right)^\dagger\right).\end{aligned} \tag{3.37}$$

Recall that $\mathcal{S}$ is Hermitian. Similar to the process above, let us include the new vector ϕ which is a solution of the equation, $\Omega\phi = \eta$. Then $\Omega^{-1}\eta = \phi$. By making this replacement, one can see that the quark line can be rewritten as an outer product of a sink vector and source vector,

$$\begin{aligned}Q_{jk} &= E\left(D_j \mathcal{S} \phi \left(D_k \mathcal{S} \eta\right)^\dagger\right) \\ &= E\left(\phi_j \eta_k^\dagger\right),\end{aligned} \tag{3.38}$$

where

$$\eta_j = D_j \mathcal{S} \eta \quad \text{and} \quad \phi_j = D_j \mathcal{S} \phi. \tag{3.39}$$

Dilution projectors can also be inserted into our quark line equation similarly to the noise vector. With a few simple steps, we can use the stochastically estimated noise vectors instead,

$$\begin{aligned} Q_{jk} &= \sum_a D_j \mathcal{S} \Omega^{-1} P^{(a)} P^{(a)\dagger} \mathcal{S} D_k^\dagger \\ &= \sum_a D_j \mathcal{S} \Omega^{-1} P^{(a)} E\left(\eta \eta^\dagger\right) P^{(a)\dagger} \mathcal{S} D_k^\dagger \\ &= \sum_a E\left(D_j \mathcal{S} \Omega^{-1} P^{(a)} \eta \left(D_k \mathcal{S} P^{(a)} \eta\right)^\dagger\right) \\ &= \sum_a E\left(\phi_j^{[a]} \eta_k^{[a]\dagger}\right), \end{aligned} \tag{3.40}$$

where we have defined

$$\begin{aligned} \eta_j^{[a]} &= D_j \mathcal{S} \eta^{[a]}, \qquad \eta^{[a]} = P^{(a)} \eta \\ \phi_j^{[a]} &= D_j \mathcal{S} \phi^{[a]}, \quad \Omega \phi^{[a]} = \eta^{[a]}. \end{aligned} \tag{3.41}$$

Though one can in principle introduce noise in the full spin-color-space-time vector space, there is another framework available to us: the LapH subspace. Because the LapH subspace has already been introduced in the simulation, it is a very convenient candidate for noise vectors. This also reduces the number of indices to track as the color and spin indices are replaced by a LapH eigenvector indices.

To understand how this stochastic factorization improved the computational cost of the simulation, consider a $32^3 \times 256$ lattice with LapH eigenumber, $N_\nu = 264$. If we consider all possible single and multi-hadron correlators of mesons and baryons made up of u and d quarks, for full dilution, this requires 270,336 inversions per configuration, whereas when stochastic LapH is applied, only 1664 inversions are needed per configuration [4].

3.3 Two-point Correlator Construction

I have now introduced the single-hadron and multihadron operators as well as quark lines. Next I will explain how we stitch those pieces together as well as use the consequences of stochastic estimation to further improve the total computation time of all correlators.

Correlator Factorization

In order to compute correlators, we shall review the original equation for computing observables on the lattice, Equation 2.19

$$\langle \mathcal{O} \rangle_T = \frac{\int \mathcal{D}[U] F(D^{-1}[U]) \det D[U] e^{-S_G[U]}}{\int \mathcal{D}[U] \det D[U] e^{-S_G[U]}},$$

where $\mathcal{O}$ is some operator, T indicates the finite time extent, and is normalized by the partition function. To compute two-point correlators in particular, we review Equation 2.10,

$$C_{ij,T}(t) = \langle 0 | \mathcal{T} \mathcal{O}_i(t + t_0) \overline{\mathcal{O}}_j(t_0) | 0 \rangle,$$

where $\mathcal{O}$ and $\overline{\mathcal{O}}$ are operators in the channel of interest.

If we apply the elemental operators as discussed in Section 3.1,

$$C_{l\bar{l}}\left(t_F - t_0\right) = c^{(l)}_{\alpha\beta\gamma} c^{(\bar{l})*}_{\overline{\alpha}\overline{\beta}\overline{\gamma}} \left\langle \Phi^{ABC}_{\alpha\beta\gamma}\left(t_F\right) \overline{\Phi}^{\overline{ABC}}_{\overline{\alpha}\overline{\beta}\overline{\gamma}}\left(t_0\right) \right\rangle, \tag{3.42}$$

we have the formal equation for any correlator. Then, we shall apply the analytic evaluation of the fermionic fields to rewrite the correlator in terms of quark lines, for example, the baryon correlator,

$$\begin{aligned} C_{l\bar{l}}(t) = c^{(l)}_{\alpha\beta\gamma} c^{(\bar{l})*}_{\overline{\alpha}\overline{\beta}\overline{\gamma}} \sum_{x\overline{x}} \; & \varepsilon_{abc} \; \varepsilon_{\overline{a}\overline{b}\overline{c}} e^{-ip\cdot(x-\overline{x})} \\ \times \; & \Big\langle Q^{(A\overline{A})}_{a\alpha;\overline{a}\overline{\alpha}} Q^{(B\overline{B})}_{b\beta;\overline{b}\overline{\beta}} Q^{(C\overline{C})}_{c\gamma;\overline{c}\overline{\gamma}} - Q^{(A\overline{A})}_{a\alpha;\overline{a}\overline{\alpha}} Q^{(B\overline{C})}_{b\beta;\overline{c}\overline{\gamma}} Q^{(C\overline{B})}_{c\gamma;\overline{b}\overline{\beta}} \\ - \; & Q^{(A\overline{B})}_{a\alpha;\overline{b}\overline{\beta}} Q^{(B\overline{A})}_{b\beta;\overline{a}\overline{\alpha}} Q^{(C\overline{C})}_{c\gamma;\overline{c}\overline{\gamma}} - Q^{(A\overline{C})}_{a\alpha;\overline{c}\overline{\gamma}} Q^{(B\overline{B})}_{b\beta;\overline{b}\overline{\beta}} Q^{(C\overline{A})}_{c\gamma;\overline{a}\overline{\alpha}} \\ + \; & Q^{(A\overline{C})}_{a\alpha;\overline{c}\overline{\gamma}} Q^{(B\overline{A})}_{b\beta;\overline{a}\overline{\alpha}} Q^{(C\overline{B})}_{c\gamma;\overline{b}\overline{\beta}} + Q^{(A\overline{B})}_{a\alpha;\overline{b}\overline{\beta}} Q^{(B\overline{C})}_{b\beta;\overline{c}\overline{\gamma}} Q^{(C\overline{A})}_{c\gamma;\overline{a}\overline{\alpha}} \Big\rangle_U, \end{aligned} \tag{3.43}$$

where we have defined $t \equiv t_F - t_0$, where time and spatial labels have been omitted, and where

$$\langle f(U) \rangle_U = \frac{\int \mathcal{D}U \, f(U) \det(M[U]) e^{-S_G[U]}}{\int DU \det(M[U]) e^{-S_G[U]}}. \tag{3.44}$$

From here, we can apply the stochastic estimation and rewrite the quark lines in terms of quark sources and sinks. The sources and sinks can be combined into hadron sources and sinks, for example, a baryon source,

$$\begin{aligned} \mathcal{B}^{[b_1 b_2 b_3]}_l\left(\varphi_1, \varphi_2, \varphi_3; t\right) = c^{(l)}_{\alpha\beta\gamma} \textstyle\sum_x e^{-ip\cdot x} \varepsilon_{abc} \\ \times \varphi^{[b_1]}_{a\alpha xt}\left(\rho_1\right) \varphi^{[b_2]}_{b\beta xt}\left(\rho_2\right) \varphi^{[b_3]}_{c\gamma xt}\left(\rho_3\right), \end{aligned} \tag{3.45}$$

where b_1, b_2, and b_3 are dilution indices, and we use short-hand notation to represent $\varphi_k = \varphi(\rho_k)$, i.e. the sink vector related to the noise vector ρ_k. The correlator can

then be rewritten as

$$
\begin{aligned}
C_{l\bar{l}}\left(t_F - t_0\right) = \Big\langle & \mathcal{B}_l^{[b_1 b_2 b_3]}\left(\varphi_1, \varphi_2, \varphi_3; t_F\right) \\
& \times \Big(\delta_{ABC}^{\overline{ABC}} \mathcal{B}_l^{[b_1 b_2 b_3]}\left(\varrho_1, \varrho_2, \varrho_3; t_0\right) \\
& - \delta_{ABC}^{\overline{ACB}} \mathcal{B}_l^{[b_1 b_3 b_2]}\left(\varrho_1, \varrho_3, \varrho_2; t_0\right) \\
& - \delta_{ABC}^{\overline{BAC}} \mathcal{B}_{\bar{l}}^{[b_2 b_1 b_3]}\left(\varrho_2, \varrho_1, \varrho_3; t_0\right) \\
& - \delta_{ABC}^{\overline{CBA}} \mathcal{B}_{\bar{l}}^{[b_3 b_2 b_1]}\left(\varrho_3, \varrho_2, \varrho_1; t_0\right) \\
& + \delta_{ABC}^{\overline{CAB}} \mathcal{B}_{\bar{l}}^{[b_2 b_3 b_1]}\left(\varrho_2, \varrho_3, \varrho_1; t_0\right) \\
& + \delta_{ABC}^{\overline{BCA}} \mathcal{B}_{\bar{l}}^{[b_3 b_1 b_2]}\left(\varrho_3, \varrho_1, \varrho_2; t_0\right) \Big)^* \Big\rangle_{U,\rho},
\end{aligned}
\tag{3.46}
$$

where $\delta_{ABC}^{DEF} = \delta_{AD}\delta_{BE}\delta_{CF}$ and $\langle \ldots \rangle_{U,\rho}$ represents an expectation value over the gauge fields U and the noise vectors ρ_k. As is shown in Equation 3.45, the correlators can be split into parts: the hadron sources and the hadron sinks.

By factorizing the correlators, this means that the sources and sinks can be calculated separately and then used for multiple correlators. One baryon sink can be used for a single or multi-hadron correlator that contains that baryon. This is yet another way we can greatly reduce the computation time.

Due to their properties, tetraquarks cannot be factorized into any smaller pieces. Similarly to mesons and baryons, the tetraquark can be thought of as one entity. In the analysis presented in this thesis, tetraquarks are not part of any multihadron operator. This is because we are not in the expected energy range of any tetraquark-meson scattering. However, as shown in the results, there is much more to learn about the nature of tetraquarks. Tetraquarks have a much more significant computational cost than mesons or baryons, for there are many more Wick contractions associated with the tetraquark operator to include when integrating out the fermions.

Chapter 4

Finite-Volume Spectrum

In order to take advantage of the Lüscher formalism to obtain continuum scattering physics, the finite-volume energies must first be evaluated. This task is challenging, and a number of theorems and methodologies have been utilized and investigated to precisely and robustly obtain the spectrum.

4.1 Correlator Matrices

Let us recall the time-dependent correlator we computed in the last chapter,

$$C_{ij}(t) = \langle 0|\mathcal{T}\mathcal{O}_i(t+t_0)\overline{\mathcal{O}}_j(t_0)|0\rangle, \tag{4.1}$$

where $\mathcal{O}_i$ and $\overline{\mathcal{O}}_j$ may represent different single- or multi-hadron operators within the same channel and irrep. Infinite-time extent is assumed. The operators are engineered to enforce the matrix as Hermitian. The correlation matrices can then be decomposed into the energy eigenstates of the channel and irrep

$$C_{ij}(t) = \sum_n Z_i^{(n)} Z_j^{(n)*} e^{-E_n t}, \tag{4.2}$$

where the energies E_n have the property $E_n < E_{n+1}$ and $Z_i^{(n)}$ represents the overlap of $\overline{\mathcal{O}}_i(t_0)|0\rangle$ with eigenstate of energy E_n, also called *operator overlap factors*. Temporal wrap-around effects are neglected. If one were to apply a phase change to the operator overlaps $Z_j^{(n)} \to Z_j^{(n)} e^{i\phi_n}$, then Equation 4.2 would remain unchanged. Due to this effect, we can only determine the magnitudes of these operator overlaps.

Often, to gain a visualization of the energy dependence of the correlators, we plot the *effective energy* or *effective mass*. The effective energy E_{eff} is the function of the correlator

$$E_{\text{eff}}(t) = -\frac{d}{dt} \ln C(t), \tag{4.3}$$

which can be estimated as

$$-\frac{1}{\Delta t} \left(\ln C(t+\Delta t) - \ln C(t)\right) \tag{4.4}$$

in discretized time. For any given correlator, the effective energy of the correlator should have the limit

$$\lim_{t\to\infty} E_{\text{eff}}(t) \to E_0, \tag{4.5}$$

where E_0 is the lowest contributing energy of the energy sum.

4.2 The Generalized Eigenvalue Problem

Though in principle one could fit to the correlators above, fitting to a tower of states at once can be very challenging and results in an often unstable high-parameter fit. Instead, we use a tactic that disentangles the lowest N energy levels in the matrix. This makes the retrieval of the energy levels much more reliable. Lüscher and Wolff outlined this important theorem in Reference [34]:

> **Theorem:** For every $t \geq 0$, let $\lambda_n(t)$ be the eigenvalues of an $N \times N$ Hermitian correlation matrix $C(t)$ ordered such that $\lambda_0 \geq \lambda_1 \geq \cdots \geq \lambda_{N-1}$, then
>
> $$\lim_{t\to\infty} \lambda_n(t) = b_n e^{-E_n t}\Big[1 + \mathcal{O}(e^{-t\Delta_n})\Big], \qquad b_n > 0, \quad \Delta_n = \min_{m\neq n} |E_n - E_m|. \tag{4.6}$$

This theorem informs us that solving for the eigenvalues at large t will allow us to determine the N lowest energies accessible to the operators in the matrix.

Because the scale of the correlators can change dramatically, to prevent round-off error when solving the eigenvalue problem, we choose a *normalization time* τ_N and normalize the correlator matrix at that time in the manner

$$\mathcal{C}_{ij}(t) = \frac{C_{ij}(t)}{\sqrt{C_{ii}(\tau_N)C_{jj}(\tau_N)}}, \tag{4.7}$$

where $\mathcal{C}_{ij}$ is our normalized correlator matrix. The normalized operator overlaps then are

$$|\mathcal{Z}_i^{(n)}| = \frac{|Z_i^{(n)}|}{\sqrt{C_{ii}(\tau_N)}}. \tag{4.8}$$

Despite the valuable disentanglement of the exponentials and the improvement of the round-off error, Theorem 4.6 alone is not enough to adequately separate the lowest energy levels. The correction term $\mathcal{O}(e^{-t\Delta_n})$ is only negligible at large times when there is a low signal-to-noise ratio. At those times, the correlators contain high fluctuations and a pivot is no longer trustworthy. Fortunately, Lüscher and Wolff addressed this issue in the same paper: The correction term can be reduced to $\mathcal{O}(e^{-t(E_N - E_n)})$ by instead solving the *generalized eigenvalue problem* (GEVP)

$$\mathcal{C}(t)v_n(t,\tau_0) = \lambda_n(t,\tau_0)\,\mathcal{C}(\tau_0)\,v_n(t,\tau_0), \quad n = 1,\cdots,N-1, \quad \frac{t}{2} \leq \tau_0 < t, \tag{4.9}$$

where τ_0 is called *metric time*. Solving this equation is equivalent to diagonalizing $G(t) = \mathcal{C}^{-1/2}(\tau_0)\,\mathcal{C}(t)\mathcal{C}^{-1/2}(\tau_0)$. The resulting time-dependent eigenvalues, or *rotated correlators*, are now guaranteed with high precision that the lowest energy level for each set of eigenvalues has $E_0 \leq E_n < E_N$ and any other energies that contribute to each eigenvalue are greater than E_N. The lowest-lying level is much easier to fit to as with larger time the higher-energy states will die off more quickly. The new eigenvalues have the form

$$\lambda_n(t) \to |Z'_n|^2\, e^{-E_n t}, \quad t \to \infty. \tag{4.10}$$

and the operator overlaps can be retrieved by

$$\mathcal{Z}_j^{(n)} \approx C_{jk}\,(\tau_0)^{1/2}\, V_{kn}(t) Z'_n \quad \text{(no sum over n)}. \tag{4.11}$$

We then order the eigenmodes of the GEVP by increasing energy. An example of the input and output of a GEVP solution is shown in Figure 4.1.

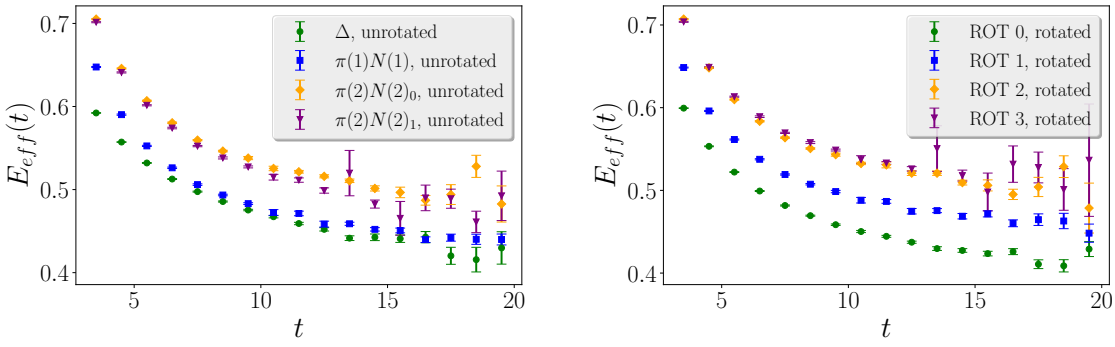

Figure 4.1: A GEVP example. Error bars are determined using bootstrap resampling method. *Left.* Diagonal correlators of the isotriplet channel with zero strangeness and irrep H_g of the little group for the total momentum squared $\boldsymbol{P}^2 = 0$. The composition of the operator is indicated by the correlator label and includes multi-hadron operators of the nucleon (N) or pion (π) operator with their individual momenta in the form of $\mathcal{O}(\boldsymbol{d}^2)$ where $\boldsymbol{P}^2 = (2\pi/L)^2\boldsymbol{d}^2$. *Right.* Time-dependent eigenvalues of the GEVP for the same channel presented in the plot on the left. Each eigenvalue is indicated by their label "ROT n" with index n which is ordered by increasing energy. GEVP was solved using the single-pivot method (see Section 4.2.1) with $(\tau_N, \tau_0, \tau_D) = (4,8,16)$.

The GEVP method assumes that the basis vectors of the matrix are linearly independent, although this is not always known before applying this method. If linearly dependent, then one eigenvalue will be very small, equal to or near zero. We can check for this by creating a condition number for the matrix using the largest and smallest eigenvalues λ

$$\xi^{\text{cn}} = \left|\frac{\lambda_{\max}}{\lambda_{\min}}\right|. \tag{4.12}$$

If this number is very large ($\geq$ 150) then this indicates that the matrix is ill-conditioned due to its basis vectors being linearly dependent. In this case, the eigenvector and eigenvalue associated with the smallest eigenvalue (≈ 0) are thrown out of the solution and not used in the result.

Although there are other methods of solving the GEVP on the samples, we have found that solving the GEVP for a given correlation matrix on the mean of the samples and then using the eigenvectors as a "pivot" to rotate on the samples of the resampling method gives us satisfactory variance on our final results. Solving the GEVP on every sample will provide more accurate error bars, but we found that this has a high computational cost and is negligibly different from the approximation (see Section 8.1 for verification of this claim). Therefore, in our analyses, we solve the GEVP on the mean sample and then apply that same pivot to the samples.

There are multiple strategies for solving and applying the solution to the correlator matrix including the *single pivot* and the *rolling pivot*.

4.2.1 Single Pivot

Though this description above indicates that the GEVP is solved on all time-slices, in practice it is less computationally intensive and more robust to compute the GEVP at one time, the diagonalization time τ_D, and then use the eigenvectors to rotate the other time-slices. This method is called the *single pivot*. Though not exact, the diagonalization at one time is nearly the same as the diagonalization of the same correlator at another time. To maximize the reduction in off-diagonal variance in the GEVP solution, τ_D is chosen as $\geq 2\tau_0$. τ_D should also be a place where there is still a high signal-to-noise ratio.

4.2.2 Rolling Pivot

In all of our studies, the single-pivot method proved to be our preferred method, but to validate the method, I extended the capabilities of our analysis to include the *rolling-pivot* method, where the GEVP is solved on every time slice. In this case, there are some difficulties due to the statistical noise in the correlator. In the ideal, noiseless case, the GEVP method could be performed on each time slice independently and order the eigenvalues in increasing order at each time slice. The eigenvalues in this order would each match to the same rotated correlator. In any Monte-Carlo simulation, exactness is impossible to reach, and there is statistical noise present. This statistical noise can cause the eigenvalues to fluctuate, and levels that are near each other can change order at some time slices. To prevent this, I check the eigenvectors. By matching the eigenvectors between each time slice, I can prevent this switching effect.

An additional issue when using the rolling-pivot method is that solving the GEVP is only trustworthy when the signal-to-noise ratio is reasonably high. At large times, the signal-to-noise ratio decreases, but that is also where the most valuable information is. (As a reminder, we seek the lowest energy from these correlators, which is achieved by estimating the $t \to \infty$ behavior.) It is more sensible to use an accurately determined pivot and apply it to later time slices than to compute the pivot at a noise-

dominated time slice; thus, the single-pivot method is preferred (given that there is no sensitivity in the final results due to changes in the diagonalization parameters).

An example of the level 0 rotated correlators for the single pivot and rolling pivot is shown in Figure 4.2.

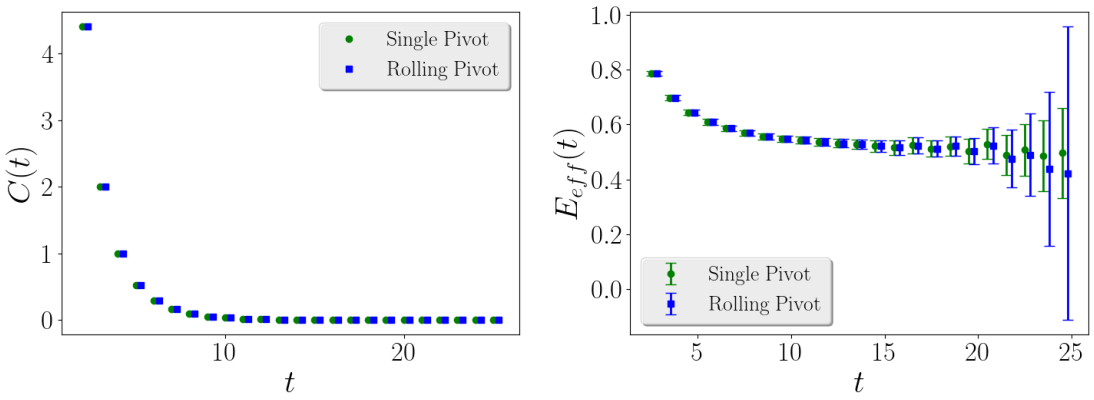

Figure 4.2: The lowest eigenvalue of the correlation matrix with isospin $I = 0$, strangeness $S = -1$, and irrep $\Lambda(\boldsymbol{d}^2) = G_{1g}(0)$. The eigenvalue was calculated using the single-pivot method with parameters $(\tau_N,\, \tau_0,\, \tau_D) = (4,4,16)$ and the rolling-pivot method $(\tau_N,\, \tau_0) = (4,4)$. *Left.* Rotated correlator plotted. *Right.* Effective energy of rotated correlator plotted.

4.3 Spectrum Fitting Methods

Once the rotated diagonal correlators are computed, we can fit to them and the noninteracting correlators to estimate the $t \to \infty$ limit. There are some key features to remember when computing these fits. One, in a Markov-Chain Monte-Carlo simulation, because each correlation function was computed from the same set of gauge ensembles, the measurements are highly correlated. Rather than a simple minimization of χ^2, we must minimize the correlated-χ^2. This requires computing the resampling covariance between observables. For the jackknife method, the covariance estimation is

$$\mathrm{cov}(f_i, f_j) = \frac{N_c - 1}{N_c} \sum_{i=1}^{N_c} \left(\langle f\rangle_i - \langle f\rangle^J\right)\left(\langle f\rangle_j - \langle f\rangle^J\right), \tag{4.13}$$

where $\langle f\rangle_i$ denotes the average of f over the i^{th} jackknife resampling, and $\langle f\rangle^J$ denotes the average of f over all samples. For bootstrap resampling, the covariance estimation is

$$\mathrm{cov}(f_i, f_j) = \frac{1}{N_b - 1} \sum_{i=1}^{N_b} \left(\langle f\rangle_i - \langle f\rangle^B\right)\left(\langle f\rangle_j - \langle f\rangle^B\right), \tag{4.14}$$

where $\langle f \rangle_i$ denotes the average of f over the i^{th} bootstrap resampling, and $\langle f \rangle^B$ denotes the average of $\langle f \rangle_i$ over all bootstrap resamplings. Once we have our equations for the covariances, we can compute the correlated-χ^2 defined by

$$\chi^2 = \sum_{t,t'} \left(C(t) - f(t;\alpha)\right) \operatorname{cov}^{-1}\left(C(t), C(t')\right) \left(C(t') - f(t';\alpha)\right), \tag{4.15}$$

where f indicates the fit model and α indicates the model's parameter set. The model parameters are then chosen by minimizing this equation on each resampling where the uncertainties are determined by the covariance equations above.

To determine the goodness of the fit (especially between different datsets and models), we compare the χ^2/d.o.f. where d.o.f. stands for the *degrees of freedom*. In principle, the ideal fit is χ^2/d.o.f. $= 1$. χ^2/d.o.f. $<< 1$ indicates overfitting of the data, and χ^2/d.o.f. $>> 1$ indicates that the model is not a good descriptor of the data. Due to Monte Carlo fluctuations in our data, the latter tends to be the case. Our rule of thumb is to aim for fits in the range χ^2/d.o.f. < 1.5, though this is not always possible.

The energies retrieved from fits to the correlator with non-zero momentum frames are in the lab frame. We want to compare and use the energies in the center-of-mass frame instead. We can shift from the lab frame to the center-of-mass frame using the energy dispersion relation

$$E_{\text{lab}} = \sqrt{E_{\text{cm}}^2 + \boldsymbol{P}^2}, \tag{4.16}$$

where E_{lab} is the energy in the lab frame, E_{cm} is the energy in the center-of-mass frame, and $\boldsymbol{P}^2$ is squared momentum.

Occasionally, when there are many models for a fit with varying complexity, the Akaike information criterion (AIC) [35] is used to choose a fit. The AIC balances the goodness of fit with the simplicity of the model and is defined by

$$\text{AIC} = \chi^2 - 2\, n_{\text{dof}}, \tag{4.17}$$

where n_{dof} denotes the number of degrees of freedom. This value is a prediction of the information error; therefore, the fit with the lowest AIC would maximally reduce the potential loss of information.

Another occasional strategy to reduce computation time is to use a derivative method of calculating the variance. Generally, to accurately calculate the variance of a fit result, the fit is performed on every sample, then the results use the method described in Section 2.3.2 to compute the variance. If the fit is a costly endeavor, then, to reduce the computational cost, a derivative method will be used instead. As described in Equation 3.4 of Reference [36], rather than recomputing the fit, this method uses the matrix of covariances between the parameters p_n and p_m, given by

$$V_{nm} = \left(\frac{\partial X_i}{\partial p_n} (C^{-1})_{ij} \frac{\partial X_j}{\partial p_m} \right)^{-1}, \tag{4.18}$$

where the partial derivatives are evaluated numerically at the minimum of χ^2 and X is the data being fitted to. This method often underestimates the variance, because it assumes linear error propagation and it does not take single-hadron mass fluctuations into account.

The AIC and the derivative method of variance are typically applied when computing scattering amplitudes from the finite-volume spectrum, though the correlated-χ^2 fitting will be the same.

4.3.1 Ratio Fits

I often fit to the correlators directly, but there is usually still a high amount of higher-energy contribution to the correlators. As stated above, the GEVP solution merely sorts out the N lowest levels for the resulting correlators. Anything above the N lowest levels still contributes to the correlators.

To remedy this, I have found that dividing the correlator by corresponding non-interacting single-hadron correlators often cancels out the higher-lying states. The *ratio correlator* is defined as

$$R(t) = \frac{\lambda_n(t)}{C_i^{\mathrm{SH}}(t) C_j^{\mathrm{SH}}(t)}, \tag{4.19}$$

where $\lambda_n(t)$ indicates a correlation matrix eigenvector and $C_i^{\mathrm{SH}}(t)$ indicates a noninteracting single-hadron correlator. The single-hadron correlators chosen correspond to the same hadrons used in the multi-hadron interacting correlators of the irrep. When possible, they are often chosen to match the constituents of the interacting operator that contributes the most significantly to that eigenvector. The limit of the ratio correlator is then

$$\lim_{t\to\infty} R(t) \to A e^{-\delta_n t}. \tag{4.20}$$

The E_{n} can easily be retrieved by the relation $\delta_n = E_n - E_{\mathrm{SH},i} - E_{\mathrm{SH},j}$ where $E_{\mathrm{SH},i}$ is retrieved using the zero-momentum single-hadron fit and the energy dispersion (Equation 4.16) relation to boost into the momentum frame of the noninteracting correlator.

One potential issue with fitting to the ratio correlator is that the ratio correlator is no longer a sum of decaying exponentials. Therefore, the location of the plateau for the correlator is not guaranteed to be the same for the ratio correlator. We find that in practice the plateau of the ratio correlator tends to start before the plateau of the simple rotated correlator. To verify our results, we compare to the results of other fit forms.

4.3.2 Standard Fit Forms

The simplest fit form to determine the $t \to \infty$ limit is the *single-exponential* model

$$C(t) = A e^{-Et}. \tag{4.21}$$

If there was no contamination, then one could fit to the entire available time range of the correlator. This is not the case, and thus we have to choose a late time range in which the correlator plateaus. Two examples are shown in Figure 4.3.

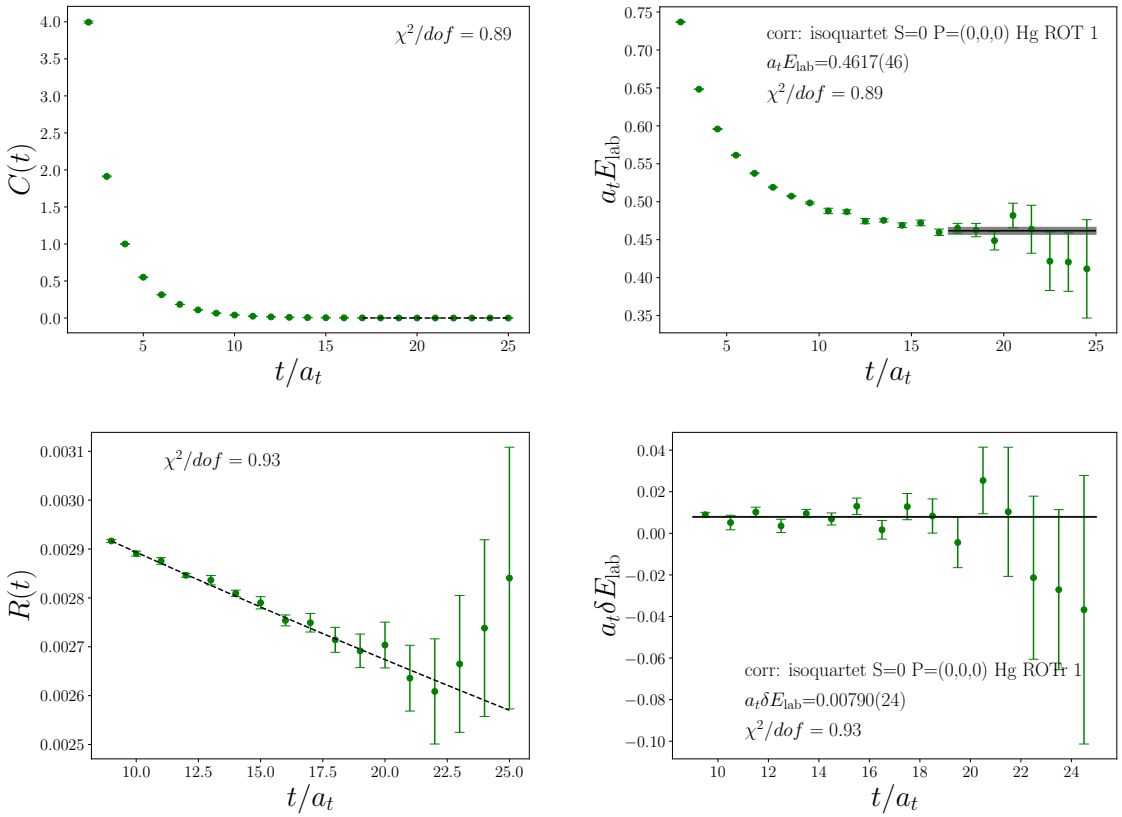

Figure 4.3: Example fits to the second eigenvalue of the $H_g(0)$ irrep matrix in isoquartet non-strange channel. *Upper left.* Correlator plotted with single-exponential model fit to t-range=[17,25]. *Upper right.* Same fit as upper left plot, but effective energy is plotted instead. *Lower left.* Ratio correlator with single-exponential model fit (independent fit in comparison to the upper plots) with t-range=[15,25]. The denominator is $\pi(1)N(1)$. *Lower right.* Same fit as lower left plot, but effective energy of the ratio is plotted instead.

Instead of ignoring the high-energy contribution completely, because we know the form of the correlator, we have several fit forms that account for it. Usually, including multiple exponentials quickly leads to unstable fits; the fit form can be written in a way that ensures stability in the χ^2 minimization. The simplest method of estimating the contamination in the fit is a simple *two-exponential* model

$$C(t) = Ae^{-Et}\left(1 + Be^{-\Delta^2 t}\right). \tag{4.22}$$

A two-exponential fit does not simulate an infinite tower of states, so fitting to the whole time range is generally not possible for a two-exponential fit either, but it tends to use more data than a single-exponential fit to the tail.

Another method that we use to try to characterize the contamination is the *geometric-series* model

$$C(t) = \frac{Ae^{-Et}}{1 - Be^{-\Delta^2 t}} = Ae^{-Et}\left(\sum_{n=0}^{\infty} B^n e^{-n\Delta^2 t}\right). \tag{4.23}$$

As shown in Equation 4.23, the denominator expands into an infinite set of evenly spaced states. Although higher-lying states cannot be accurately determined with this method, it is often successful in estimating the contamination.

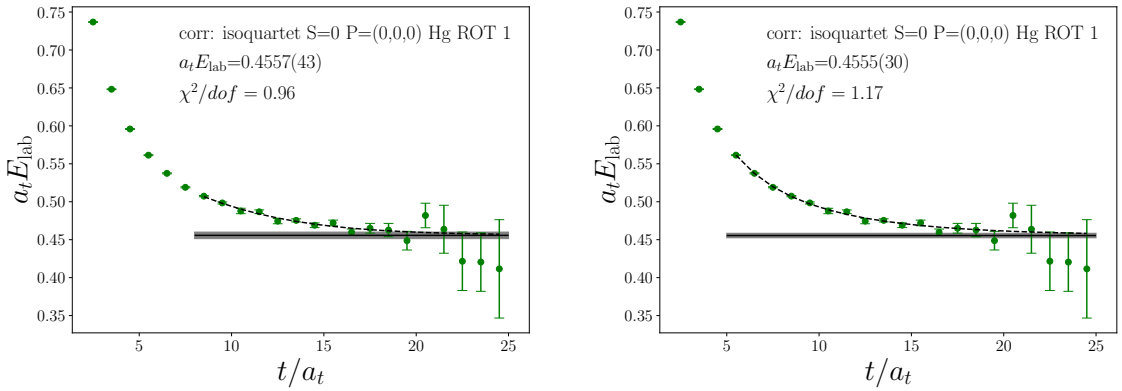

Figure 4.4: More example fits to the second eigenvalue of the $H_g(0)$ irrep matrix in isoquartet nonstrange channel. *Left.* Effective energy of the correlator plotted with a two-exponential model fit to t-range=[10,25]. *Right.* Effective energy of the correlator plotted with a geometric-series model fit to t-range=[6,25].

4.3.3 Stability Analysis

When choosing a fit, not only do we consider the χ^2/d.o.f, we take into account a variety of fit forms applied to both the rotated correlator and the ratio of the rotated correlator over non-interacting correlators. If a fit is applied to the ratio correlator, the result is nicknamed a "ratio fit". To assess the validity of a fit, we often compare the fit results with a similar fit to the same fit form but with a different t_{min}. We consider the fit to be reliable if it has a good χ^2/d.o.f and is consistent between fits with varying t_{min}s, also called the *plateau* of the fit. We compare the plateau regions of multiple fit forms. An example is shown in Figure 4.5. In this case, we chose a single-exponential fit to the ratio correlator with $t_{\text{min}} = 9$ because it was precise and consistent with similar fits and the plateau regimes of other fit forms.

4.3.4 Finite-time Domain Effects

To seek $t \to \infty$ information on a lattice of finite temporal extent T, some care must be taken. We can make this assumption because T is large enough that any effects

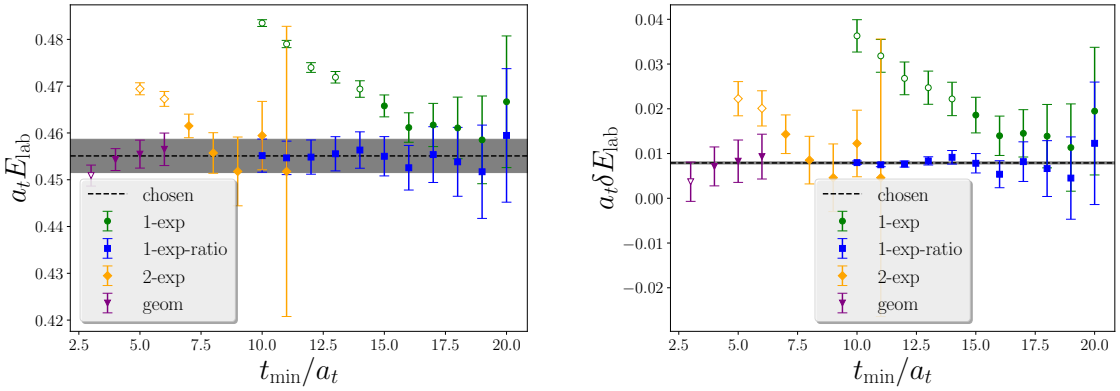

Figure 4.5: Results of many fits to the second eigenvalue of the $H_g(0)$ irrep matrix in isoquartet nonstrange channel. All fits use $t_{\text{max}} = 25$. *Left.* E_{lab} of the resulting fit for varying t_{min} and fit forms. In this plot, ratio fit results shifted to E_{lab} for comparison. The energies are shifted using the relation described in the text of Section 4.3.1. *Right.* Same data as left plot, but the ratio results are unmodified and all the other fit results are shifted to compare to the ratio fit results. Filled symbols indicate a good fit ($\chi^2/\text{dof} < 1.4$). Hollow symbols indicate a poor fit ($\chi^2/\text{dof} \geq 1.4$). Horizontal dotted black line and grey band indicate the value and variance of the chosen fit.

of the far wall are negligible.

To verify this assumption, we can study the single-exp fit model with wall effects

$$C(t) = A(e^{-Et} + e^{-E(T-t)}). \tag{4.24}$$

When the assumption $T \to \infty$ is made, the model simplifies to a single-exponential fit. Fits to the kaon and nucleon are shown in Figure 4.6. The finite-time effects are

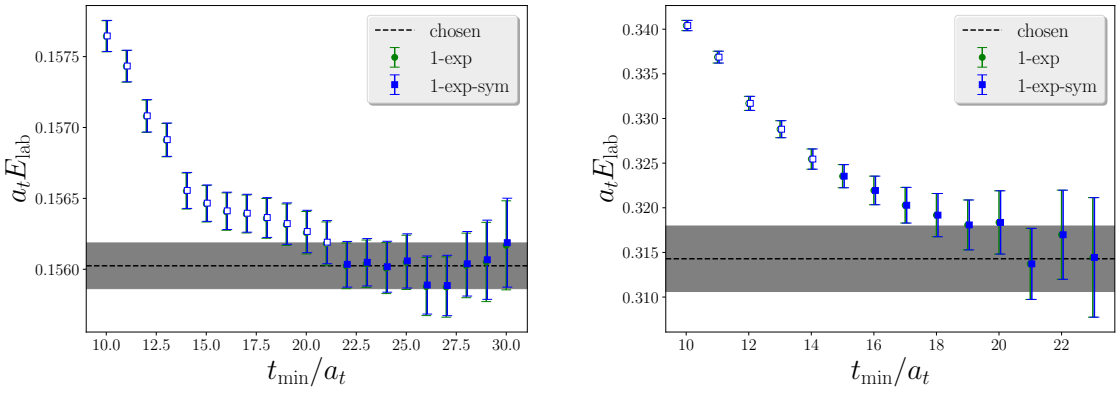

Figure 4.6: Several fits for varying t_{min} to single-exponential model (1-exp) and Equation 4.24 (1-exp-sym). Filled symbols indicate a good fit ($\chi^2/\text{dof} < 1.5$). Hollow symbols indicate a poor fit ($\chi^2/\text{dof} \geq 1.5$). Horizontal dotted black line and grey band indicate the value and variance of the chosen fit. *Left.* Fits to the kaon single-hadron correlator are shown. *Right.* Fits to the nucleon correlator.

known to only affect the lightest states. The pion was also investigated, but because of its extremely high precision, statistical fluctuations due to autocorrelation caused the pion fits using Equation 4.24 to have a large χ^2.

4.3.5 Exploratory Fit Forms

The precision and amount of information to be gained from the Lüscher analysis greatly depend on the precision and accuracy of the finite-volume spectrum. Single- and two-exponential fits alone often produce fits with variance that is similar in magnitude to the statistical noise of the tail-end data. We often need more precise results. This can be produced in two ways: we can either use increased statistics (computationally expensive), or we can use the properties of the correlators to precisely determine the tail-end behavior (much cheaper).

I have integrated two additional methods/tools into our analysis chain to use on future projects, *priors* and *simultaneous fits*. Using these tools, new fit models have been investigated.

Constrained Parameters

Given that we have knowledge of how the parameters should behave, we can introduce parameter constraints into the fit [37]. By setting a mean and width for the prior of a given parameter, we can stabilize fits that would otherwise have failed.

In order to add priors to the fit, instead of minimizing the correlated-χ^2 we fit to an augmented correlated-χ^2

$$\chi^2 \quad \rightarrow \quad \chi^2_{\text{aug}} \equiv \chi^2 + \chi^2_{\text{prior}} \tag{4.25}$$

where χ^2_{prior} takes the form

$$\chi^2_{\text{prior}} \equiv \sum_i \frac{(P_i - \tilde{P}_i)^2}{\tilde{\sigma}_i^2} \tag{4.26}$$

where some or all parameters of the fit P_i are given the prior mean $\tilde{P}_i$ and prior width $\tilde{\sigma}_i$. This augmented χ^2 discourages the parameter from moving away from the value $\tilde{P}_i$ with strength dependent on $\tilde{\sigma}_i$. The values for the priors are based on prior knowledge of the fits.

To prevent these priors from artificially reducing our error bar, we tend to choose large prior widths, larger than the noise in the tail-end behavior. Also, when resampling, rather than using the user set point $\tilde{P}_i$, the fits to the samples instead use a random sampling from a normal distribution with mean of $\tilde{P}_i$ and width of $\tilde{\sigma}_i$. Parameter constraints are very helpful in modeling contributions from the high-lying states that are not of interest, but care must be taken to ensure the low-lying parameters of interest are insensitive to the parameter constraints.

Simultaneous Fits

Exactly as the name indicates, simultaneous fits are when two fit forms to two datasets are minimized together. Because of the highly correlated data, this can be advantageous even if the parameters and data are completely independent between the two fits, but simultaneous fits also have the ability to share parameters between fits. This can be advantageous when we believe that different correlators will share parameters. This will be useful when a precise signal cannot be achieved otherwise.

Multiexponential Method

The current method of our analysis includes looking at every single rotated correlator and manually choosing a fit form and t-range based on the plateaus of each fit. This is a very tedious task that we would like to simplify by generating a fit form that can characterize the entire time range of the correlator while still accurately retrieving the energies.

One method I came up with and tested was what I called the "multiexponential method". This method was developed with the intention of trying to characterize the correlator contamination with a sum of exponentials, but only the lowest energy level obtained from the fit is considered for later use. Fits to a linear superposition of exponential terms are generally unstable due to the large number of parameters that are poorly constrained. In order to make the fits produce useful results, additional constraints must be added. The method tested here imposes such constraints using Bayesian priors and a level-by-level approach.

The level-by-level approach begins with a fit to a simple single-exponential model,

$$C(t) = A_0 e^{-E_0 t}, \tag{4.27}$$

and with the full available time-range. Then, the t_{min} is increased until the fits reach a consistency in value and also achieve an acceptable χ^2/d.o.f.. Once a final fit has been chosen based on these qualifications, the energy fit and error are used as a prior in the next fit with prior mean of E_0 and prior width of $c\sigma_{E_0}$ where σ_{E_0} is the variance and c is a inflating factor. To avoid an underestimation of the error variance, the inflating factor is greater than one. The next fit is to the two-exponential model

$$C(t) = A_0 e^{-E_0 t}\left(1 + A_1 e^{-E_1^2 t}\right), \tag{4.28}$$

where E_0 is priored with the resulting value from the single-exponential fit. Similarly, this fit is done with the entire time-range and then the t_{min} is increased until it has entered the stability region and has an acceptable χ^2/d.o.f..

After the two-exponential fit, the data is fit to a three-exponential fit

$$C(t) = A_0 e^{-E_0 t}\left(1 + A_1 e^{-E_1^2 t} + A_2 e^{-E_2^2 t}\right), \tag{4.29}$$

to the entire t-range where E_0 and E_1 are priored according to the best stable results for the two-exponential fit (widths are inflated). Fits with three exponential fits or higher are given a wide-ranging prior of mean $\tilde{E}_n = 2E_{n-1}$ and width $\tilde{\sigma}_{E_n} = E_{n-1}/2$ on the highest energy to prevent the highest energy from running away to infinity or falling to the same value as one of the lower energies. This process is continued until the entire range is fitted with a tower of states with a good χ^2/d.o.f.. An example of this process at each stage is presented in Figure 4.7.

An issue found with this method was that it had the tendency to overfit the noise region. See the example in Figure 4.8. Checks on this method included looking for consistency with alterations of the inflating factor. Due to the overfitting of the noise and these failed checks, this method was never used for final results.

Conspiracy

Based on the success of the ratio fits, a new method developed by André Walker-Loud, facetiously called the "conspiracy" method, takes advantage of contamination cancellation to form a priored simultaneous fit. Based on the similar contamination structures, it was hypothesized that the leading contaminating states are the same or similar. To construct this fit, we first start with a two-exponential fit to the single hadrons. Let us start with the degenerate case, where the two single hadrons chosen for the interacting correlator are the same hadron. The single hadron is fit to a two-exponential model:

$$C_{\mathrm{SH}}(t) = A_{\mathrm{SH}} e^{-m_{\mathrm{SH}} t} \left(1 + B_{\mathrm{SH}} e^{-\Delta^2_{\mathrm{SH}} t}\right). \tag{4.30}$$

Then for the interacting correlator fit, the single hadron is fit to Equation 4.30 simultaneously with the conspiracy fit to the interacting correlator

$$C_{\mathrm{ROT}}(t) = A_{\mathrm{ROT}} e^{-E_0 t}(1.0 + R_{\mathrm{ROT},1} e^{-(\Delta^2_{\mathrm{SH}} + \delta_1)t} + R_{\mathrm{ROT},2} e^{-(2.0\Delta^2_{\mathrm{SH}} + \delta_2)t}), \tag{4.31}$$

where each parameter is given a prior according to Table 4.1. The conspiracy model in Equation 4.31 is based on $C^2_{\mathrm{SH}}(t)$,

$$C^2_{\mathrm{SH}}(t) \to A^2_{\mathrm{SH}} e^{-2m_{\mathrm{SH}} t}(1.0 + 2B_{\mathrm{SH}} e^{-\Delta^2_{\mathrm{SH}} t} + B^2_{\mathrm{SH}} e^{-2.0\Delta^2_{\mathrm{SH}} t}). \tag{4.32}$$

As you can see, the conspiracy model bases its exponential form on the denominator, but does not assume amplitudes and allows for flexibility of the exponents. Due to the large number of exponentials, priors are needed to keep the fit stable, but the widths of the priors are inflated to ensure accuracy of the precision of the results. This method has had success, especially in noisy baryon-baryon correlators studied in current projects. This same methodology is applied to the non-degenerate case as well as using three-exponential single-hadron fits for the conspiracy fit.

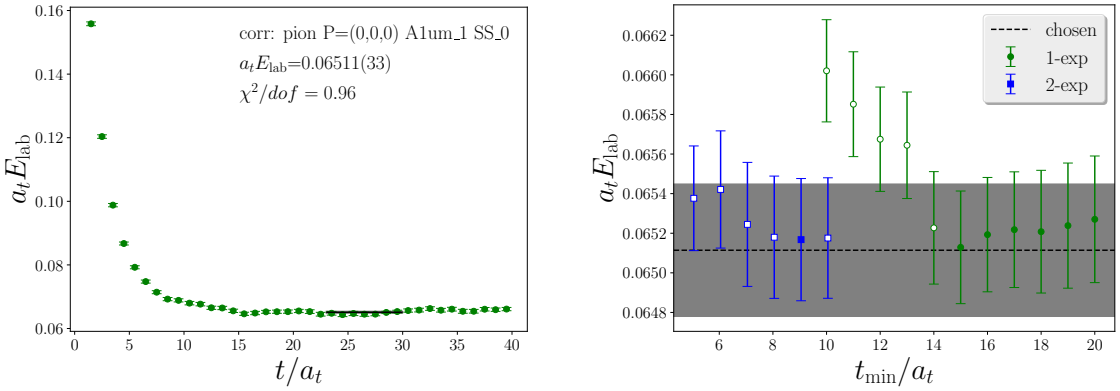

(a) single-exponential

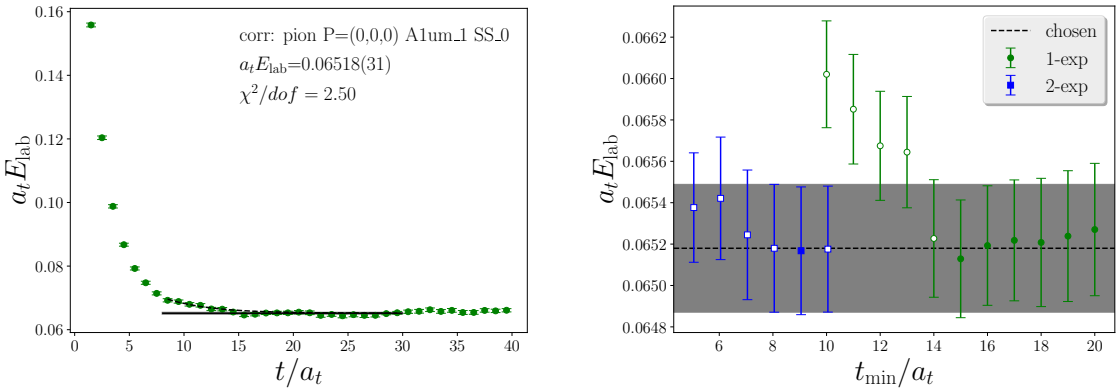

(b) two-exponential

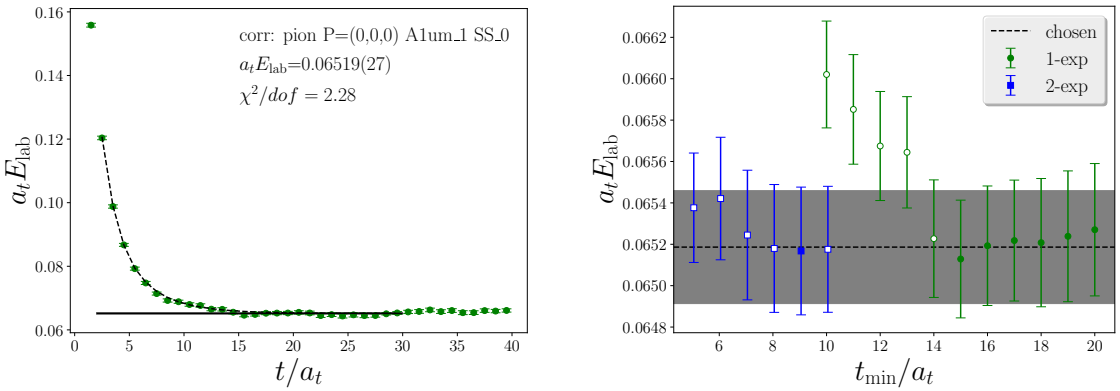

(c) three-exponential

Figure 4.7: Example of the steps in the multi-exp method applied to the D200 pion correlator. On the left, the correlator and model are plotted in effective energy. On the right, each result is compared to fits of the single- (1-exp) and two- (2-exp) exponential models without priors.

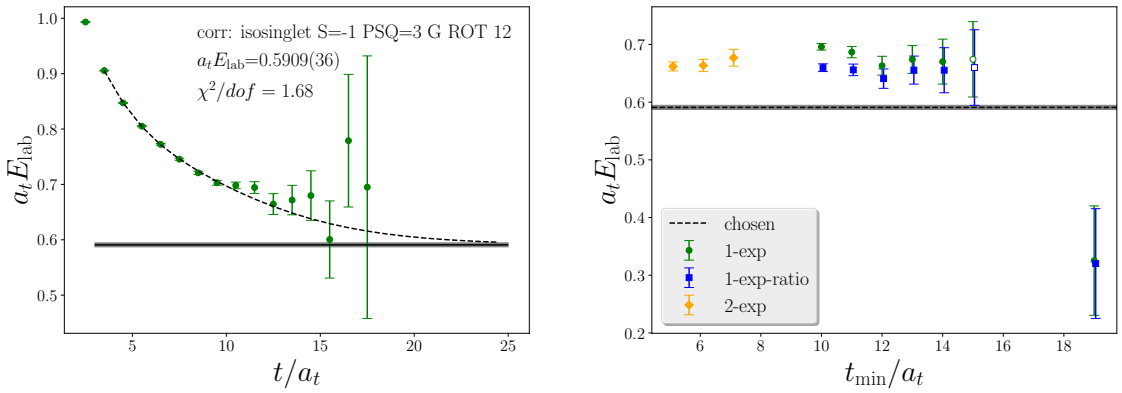

Figure 4.8: Example of the multi-exponential fit applied to the thirteenth correlator of the $G(3)$ irrep in the channel with isospin $I = 0$ and strangeness $S = -1$. All fits used a $t_{\rm max} = 25$. *Left.* Effective energy of the rotated correlator. *Right.* t-min plot comparing results of various fit forms with different fit-ranges.

parameter	mean	width
$A_{\rm SH}$	$A_{\rm SH,ind}$	$c\sigma_{A_{\rm SH,ind}}$
$m_{\rm SH}$	$m_{\rm SH,ind}$	$c\sigma_{m_{\rm SH,ind}}$
$B_{\rm SH}$	$B_{\rm SH,ind}$	$c\sigma_{B_{\rm SH,ind}}$
$\Delta_{\rm SH}$	$\Delta_{\rm SH,ind}$	$c\sigma_{\Delta_{\rm SH,ind}}$
E_0	$\tilde{E}_0 \equiv$ Effective energy of correlator at diagonalization time	$0.1\tilde{E}_0$
$A_{\rm ROT}$	$\tilde{A}_{\rm ROT} \equiv C(\tau_D)/e^{-\tilde{E}_0\tau_D}$	$0.5\tilde{A}_{\rm ROT}$
$R_{\rm ROT,1}$	1.0	0.5
$R_{\rm ROT,2}$	1.0	0.5
δ_1	0.0	0.015
δ_2	0.0	0.015

Table 4.1: Priors set for degenerate conspiracy fits. The single-hadron parameters in the simultaneous fit are set by the resulting parameters of an independent fit, and the widths are inflated by parameter c. The priors for the conspiracy fit to the interacting hadron are set based on expectations of the values and the data at the diagonalization time τ_D.

Chapter 5

Scattering Observables from the Lattice

The energy spectrum of a lattice of finite volume is very different from the spectrum of infinite volume. Because of the finite volume, first, there are no asymptotic states, and second, the boundary conditions quantize the momentum which gives us a discrete set of states in our spectrum, whereas in infinite volume the energy states are a continuous distribution. However, the discrete energy states can still give us information about the scattering amplitudes. Though the results that we observe will depend on the lattice volume, once we have the same calculations on multiple lattices with different lattice volumes, the continuum-physics results can be achieved at high precision.

The information and descriptions in this section are based heavily on the works of References [38, 39].

5.1 Scattering Observables of Interest

The ultimate goal for our calculations is to compute observables that experimentalists can compare to. The values that experimentalists measure in particle scattering experiments are the differential cross sections, i.e. the probability of the particle scattering at a certain angle for a certain interaction (see diagram in Figure 5.1). In order to accurately determine the differential cross section, all possible interactions must be accounted for in the experiment. Lattice QCD can provide input for many possible interactions, especially strong-force-dominated interactions, in the non-perturbative regime.

In our analyses, we do not directly calculate the differential cross section, but instead the partial-wave amplitudes. As a quick exercise, I will illustrate how the differential cross section is related to these quantities.

Through quantum field theory, the differential cross section $\frac{d\sigma}{d\Omega}$ is related to the scattering amplitude $\mathcal{M}$. For example, for the $2 \to 2$ scattering in the center-of-mass

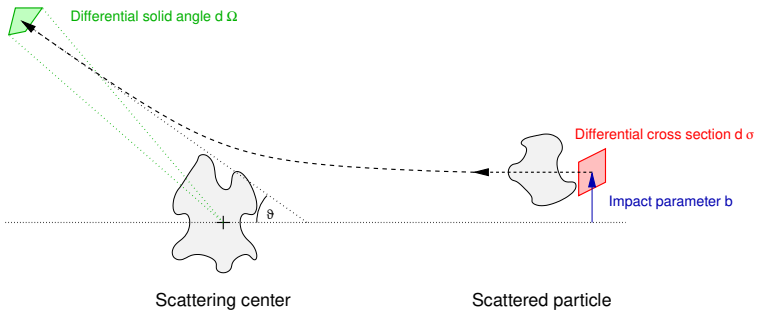

Figure 5.1: Visualization of the differential cross section $\frac{d\sigma}{d\Omega}(\theta)$. Figure provided by Wikipedia Commons [40].

(cm) frame for nonidentical particles, the relation is

$$\frac{d\sigma}{d\Omega}(\theta) = \frac{1}{64\pi^2 s}\frac{p_f}{p_i}|\mathcal{M}_{fi}(\theta)|^2, \tag{5.1}$$

where p_i and p_f represent the magnitude of each incoming and outgoing particle momentum and $s = \sqrt{E_a + E_b}$ where E_a and E_b are the center-of-mass energies of the incoming particles of masses m_a and m_b. The elastic scattering amplitude can then be decomposed into terms of partial-wave amplitudes,

$$\mathcal{M}(\theta) = \frac{1}{4\pi}\sum_{\ell} P_\ell(\cos\theta)\,\mathcal{M}_\ell(s). \tag{5.2}$$

Hadronic resonances are expected to only affect one of the infinite set of partial wave amplitudes, giving us a way to isolate their effect. To conserve the probability above the kinematic threshold, the transition amplitude must satisfy the elastic unitarity condition

$$\mathrm{Im}\frac{1}{\mathcal{M}_\ell} = -\frac{1}{16\pi}\frac{2\,q}{E}\Theta(E - E^{\mathrm{thr.}}), \tag{5.3}$$

where E is the cm-frame energy, q is the cm-frame momentum, and $E^{\mathrm{thr.}}$ is the kinematic threshold $E^{\mathrm{thr.}} = m_a + m_b$. Utilizing the Equations 5.2 and 5.3, it is common to write the real part of the partial-wave amplitudes in terms of phase shifts

$$\mathrm{Re}\frac{1}{\mathcal{M}_\ell} = \frac{1}{16\pi}\frac{2\,q}{E}\cot\delta_\ell(E). \tag{5.4}$$

5.2 Resonances

Relatively few hadron species exist in the form of bound states, hadrons that do not decay[1] such as pions, neutrons, protons and so on, but most known species decay

[1] I am only considering decay through the strong force in this thesis.

quickly and are known as *resonances*. Resonances are short-lived particle states that decay into the common hadrons of the scattering channel, whether that be the original particles or two particles of the same combined quantum numbers.

Narrow resonances contribute peak-like structures to cross sections and are characterized by their mass and widths. A qualitative diagram is shown in Figure 5.2. The mass and width can be computed from the lattice using the scattering amplitudes calculated from the Lüscher quantization condition. The presence of a resonance can be clearly be indicated by a rapid rise in the phase shift, as shown in Figure 5.2.

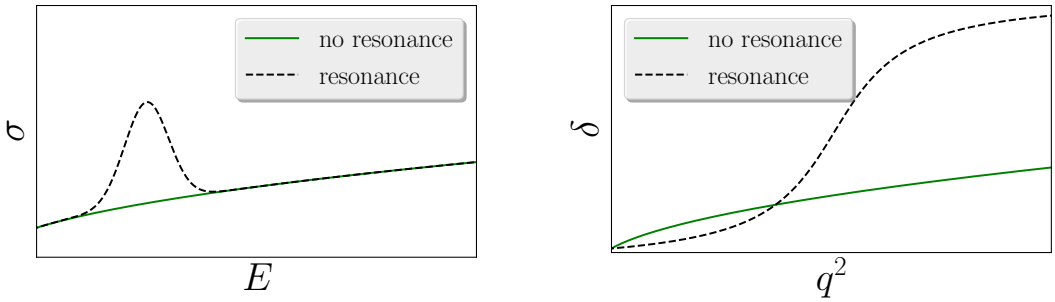

Figure 5.2: Left. Diagram of the qualitative features of a resonance in a cross section. Right. Diagram of qualitative features of phase shift when resonance is and is not present.

5.2.1 Riemann Sheets

Bound states and resonances correspond to specific poles in the scattering matrix, which can occur on different *Riemann sheets*. When considering the center-of-mass momentum,

$$q = \frac{1}{2}\left[s - 2(m_1^2 + m_2^2) + \frac{\left(m_2^2 - m_1^2\right)^2}{s}\right]^{1/2}, \tag{5.5}$$

one would notice that there is an overall square root function. Because this is a function of the complex Mandelstam variable s, $\mathcal{M}_\ell(s)$ features a branch cut at threshold $s = \left(m_1 + m_2\right)^2$ and therefore, two Riemann sheets to represent the q domain for scattering in a single channel. A visualization of the singularities in the complex q and complex E_{cm} planes for non-relativistic single-channel scattering can be seen in Figure 5.3. The physical (first) sheet in the complex energy plane where real scattering occurs is where $\text{Im}(q) > 0$ and the unphysical (second) sheet is where $\text{Im}(q) < 0$. Particles will appear as pole singularities in $\mathcal{M}_\ell(s)$ where ℓ is the particle's angular momentum. The type of particle can be defined by its location on the Riemann sheet. Bound states are poles on the real axis of the physical sheet and below threshold. Poles off the real axis on the unphysical sheet are resonances. A pole on the real

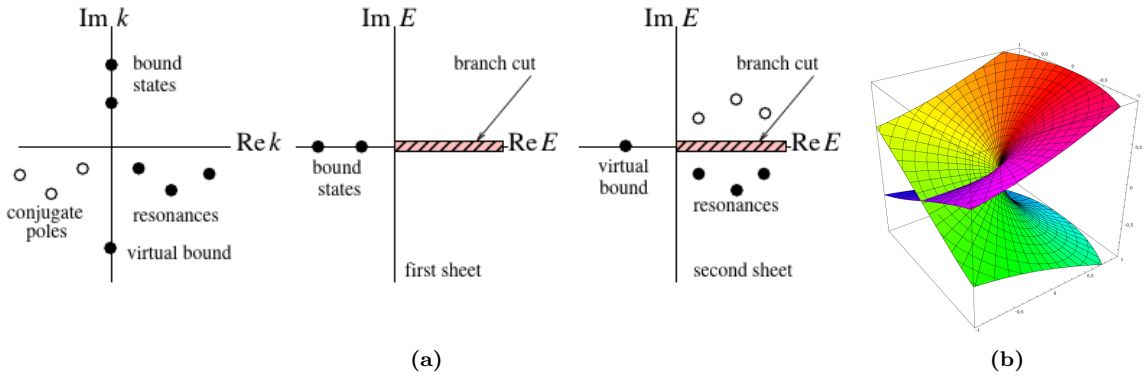

Figure 5.3: Diagrams of the pole locations on the Riemann sheets for non-relativistic single-channel scattering. **(a)** Pole positions corresponding to different types of particles in the center-of-mass momentum k and then on the Riemann sheets of the cm energy E. Figure provided by Colin Morningstar. **(b)** Example of the Riemann surface of the complex function $f(z) = \sqrt{z}$. Figure provided by Wikipedia Commons [41].

axis but on the unphysical sheet is a *virtual bound state*. All other locations on this Riemann sheet are unphysical locations for poles.

When considering nonphysical pion mass, this can cause poles to move on the Riemann sheets compared to the physical pion mass. Using effective field theories, we can often predict how the pole positions will move as a function of quark mass, and often the particles that we study in our lattice QCD simulations can be stable for large quark mass, and then become unstable resonances for lighter quark masses.

5.3 Phase Shifts: A One-Dimensional Example

To better understand how finite-volume energies can yield infinite-volume scattering information, I will present an example of calculating the scattering phase shift on a one-dimensional lattice. In this example, I will overview the simple case of elastic scattering of two identical spinless bosons in one spatial dimension in non-relativistic quantum mechanics [42].

For the quantum mechanics formulation, let us suppose that bosons, separated by a distance $|x|$, interact through a finite-range potential, $V(|x|)$, with $V(|x| > R) = 0$. Outside the potential, the wave-function of the two-boson system will be of the form $\psi_p(|x|) \sim \cos\big(p|x| + \delta(p)\big)$, where all values of the momentum, $p \geq 0$, are allowed. Given that we know the potential function, the energy eigenfunctions within the range of the potential and the wavefunctions can be matched at $x = R$ to determine the phase shift.

Now, instead of a continuum system, place this system on a lattice with size $L > R$. The momenta are quantized due to the boundary conditions, but in addition, due to the boundary conditions, the allowed momenta of the wavefunctions have the

condition

$$p = \frac{2\pi}{L} n - \frac{2}{L}\delta(p).$$

This result highlights some of the qualitative features that we are looking for in our spectrum. If there is no scattering, the phase shift will be $\delta = 0$, and the spectrum will be equivalent to the free particle spectrum. When δ is nonzero, the discrete spectrum will depend on the infinite-volume phase shift. Both the spectrum and the phase shift will depend on the lattice volume.

These same qualitative features are present when repeating this exercise with quantum field theory and a three-dimensional cubic box.

5.4 Lüscher Quantization Condition

The *Lüscher quantization condition* (LQC) is given by

$$\det\left[F^{-1}(E, \boldsymbol{P}; L) + \mathcal{M}(E)\right] = 0, \tag{5.6}$$

where $\mathcal{M}$ is built out of infinite-volume scattering matrices and F^{-1}, where F^{-1} encodes how the partial waves fit into the finite volume to satisfy the boundary conditions. Though the idea of extracting scattering information predates Lüscher's first published quantization condition [43, 44], he was the first to adapt a method for lattice QCD. In this first work, the relation was limited to scattering between two identical spinless particles with zero total momentum interacting via a central potential. Much work has been done since to expand its capabilities [45–63], and the modern relation [63] is only limited to all possible two-to-two scattering. (Breakthroughs are currently being made in three-particle scattering [64, 65].) While we are limited to two-to-two scattering, our energy range is limited by the three-particle threshold.

The Lüscher quantization condition in Equation 5.6 is derived by equating two different but equivalent versions of the two-point correlation function in a finite volume. The first way to write the correlation function is as a discrete set of eigenstates, which is outlined in Section 2.2.2, but is generalized here,

$$C_L(t, \boldsymbol{P}) = L^6 \sum_n e^{-E_n t} \langle 0|\mathcal{O}(0)|E_n, \boldsymbol{P}; L\rangle \left\langle E_n, \boldsymbol{P}; L|\overline{\mathcal{O}}(0)|0\right\rangle, \tag{5.7}$$

where the function is equivalent to Equation 2.10 but the volume dependence is included. The second way is diagrammatic, where the difference between the finite and infinite correlators come to play. The diagram is shown in Figure 5.4c and can be written as

$$\mathcal{F}_L = \left[\frac{1}{L^3} \sum_{\boldsymbol{k} - \int \frac{d\boldsymbol{k}}{(2\pi)^3}}\right] \int \frac{dk_4}{2\pi} \quad \times \mathcal{L}(P-k,k)\,\Delta(k)\,\Delta(P-k)\,\mathcal{R}^\dagger(P-k,k), \tag{5.8}$$

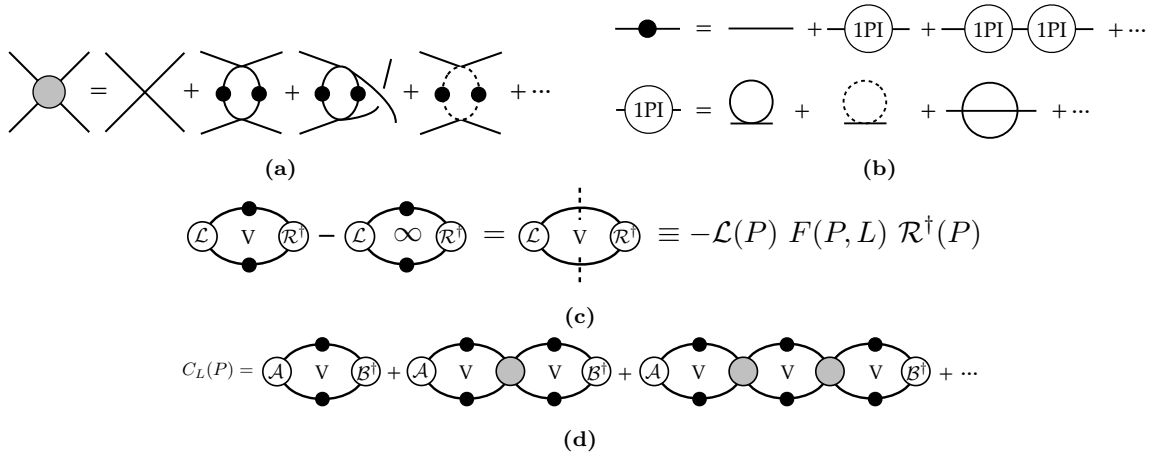

Figure 5.4: Diagrams of relevant scattering quantities. **(a)** Fully dressed single particle propagator. **(b)** Solid lines correspond to the particles in the primary channel being considered, while dashed lines indicate fluctuations due to particles that cannot go on-shell. **(c)** The finite-volume function, $\mathcal{F}(P, L)$, defined in Equation 5.8, expressed in terms of the difference between finite and infinite-volume two-particle loop. **(d)** The diagrammatic representation of the finite-volume two-point correlation function for energies where the two-particle states can go on-shell.

where R and $\mathcal{L}$ are arbitrary smooth functions and $\boldsymbol{k}$ is the discrete momentum $\boldsymbol{k} = (2\pi/L)\boldsymbol{n}$. The finite-volume diagrammatic equation can then be written as

$$C_L(t, \boldsymbol{P}) = L^3 \int \frac{dP_4}{2\pi} e^{iP_4 t} \left[C_\infty - \mathcal{O}_i^\star\, F(L) \sum_{n=0} \Big(-\mathcal{M}\, F(L) \Big)^n \mathcal{O}_j^\star \right], \tag{5.9}$$

$$= L^3 \int \frac{dP_4}{2\pi} e^{iP_4 t} \left[C_\infty - \mathcal{O}_i^\star \Big[F^{-1}(L) + \mathcal{M} \Big]^{-1} \mathcal{O}_j^\star \right], \tag{5.10}$$

where $\mathcal{O}_i$ are the hadronic operators, C_∞ is the infinite-volume correlation function, F^{-1} is related to $\mathcal{F}_L$ via $\mathcal{F}_L = -\mathcal{L}_{\ell m}(P)\, F_{\ell m;\ell' m'}(P, L)\, \mathcal{R}^\dagger_{\ell' m'}(P)$, and all matrices and operators have dependence on P.

To compare Equation 5.10 with Equation 5.7, the poles that appear when evaluating the integral in Equation 5.10 must cancel and create a similar exponential function as in Equation 5.7. These poles that arise due to the finite volume will appear in the $\big[F^{-1}(P, L) + \mathcal{M}(P)\big]^{-1}$ term in Equation 5.10. The term will diverge if the matrix $\big[F^{-1}(P, L) + \mathcal{M}(P)\big]$ is singular, leading to the coveted LQC found in Equation 5.6.

5.5 K-matrix/Box Matrix Form of Lüscher Quantization Condition

The current form of the LQC relates each individual energy to an infinite sum of partial waves. The equation also does not account for irreps in the finite-volume

energies instead of the angular momentum (recall Section 3.1.2). In order to solve the LQC, the infinite sum of partial waves must be truncated in a sensible way, and the basis of the energies needs to be subduced into irreps. To accomplish this, we start by rewriting Equation 5.6 in a more convenient form.

The elastic scattering matrix $\mathcal{M}$ is unitary and dimensionless. Because it is easier to manipulate a real symmetric matrix than a unitary one, the commonly used K-matrix can be introduced. Through some simple matrix algebra, one can use the relations $\mathcal{M} = S - 1$ and $S = (1 + iK)(1 - iK)^{-1}$, to replace $\mathcal{M}$ with K in the LQC

$$\det\left[F^{-1}(E, \boldsymbol{P}; L) + 2iK(\boldsymbol{P})(1 - iK(\boldsymbol{P}))^{-1}\right] = 0. \tag{5.11}$$

Next, it is prudent to establish a basis and include symmetries in the matrices F and K. We use the quantum numbers of the continuum to establish our basis $|Jm_J LSa\rangle$, where J is the total angular momentum of the two particles in the center-of-momentum frame, m_J is the projection of the total angular momentum of the two particles on the z-axis, L is the orbital angular momentum of the two particles in the center-of-momentum frame, and S is the total spin of the two particles. Index a, for convenience, will represent all other quantum numbers including strangeness and the species indicators for the two constituent particles: each particle will have spin, parity, isospin, isospin projection and occasionally G-parity. Note that L and S are also used for lattice length and the S-matrix everywhere else, but in the remainder of this section, these variables will indicate the quantum numbers for the system. In this basis, F is defined as

$$\begin{aligned}\langle J'm_{J'}L'S'a'|F^{(\mathbf{P})}|Jm_J LSa\rangle = \delta_{a'a}\delta_{S'S}\ \frac{1}{2}\{&\delta_{J'J}\delta_{m_{J'}m_J}\delta_{L'L} \\ &+\langle J'm_{J'}|L'm_{L'}Sm_S\rangle\langle Lm_L Sm_S|Jm_J\rangle W^{(\mathbf{P}a)}_{L'm_{L'};\ Lm_L}\},\end{aligned} \tag{5.12}$$

where $\langle j_1 m_1 j_2 m_2|JM\rangle$ are the Clebsch-Gordan coefficients. The matrix element $W^{(\mathbf{P}a)}$ includes a sum of Rummukainen-Gottlieb-Lüscher (RGL) shifted zeta functions $\mathcal{Z}_{lm}$ [46, 47, 66, 67].

For further convenience, we rewrite F and K into the box matrix, B, with elements defined as

$$\begin{aligned}\langle J'm_{J'}L'S'a'|\,B^{(\mathbf{P})}\,|Jm_J LSa\rangle = -i\delta_{a'a}\delta_{S'S}\ u_a^{L'+L+1}\ W^{(\mathbf{P}a)}_{L'm_{L'};\ Lm_L} \\ \times\langle J'm_{J'}|L'm_{L'}, Sm_S\rangle\langle Lm_L, Sm_S|Jm_J\rangle\end{aligned} \tag{5.13}$$

and $\widetilde{K}$, with elements defined as

$$K^{-1}_{L'S'a';\ LSa}(E_{\mathrm{cm}}) = u_{a'}^{-L'-\frac{1}{2}}\ \widetilde{K}^{-1}_{L'S'a';\ LSa}(E_{\mathrm{cm}})\ u_a^{-L-\frac{1}{2}}. \tag{5.14}$$

The box matrix is Hermitian, and $\widetilde{K}$ is real and symmetric and should behave smoothly in E. In this form, the LQC can be written as

$$\det\left(1 - B^{(\boldsymbol{P})}\widetilde{K}\right) = \det\left(1 - \widetilde{K}B^{(\boldsymbol{P})}\right) = 0. \tag{5.15}$$

There are some other physics consequences that have not yet been explicitly outlined: The LQC formulation in this section applies to both indistinguishable and distinguishable particles, although in the case of identical particles of isospin I_1, the value $L + S + I - 2I_1$ must be even, where I is the total isospin and L and S are quantum numbers of the basis. Also, rotational invariance implies that $\widetilde{K}$ must have the form

$$\langle J' m_{J'} L' S' a' | \ \widetilde{K} \ | J m_J L S a \rangle = \delta_{J'J} \delta_{m_{J'} m_J} \ \mathcal{K}^{(J)}_{L'S'a';\ LSa}(E_{\mathrm{cm}}). \tag{5.16}$$

Because $\widetilde{K}$ is analytic in E_{cm}, we can now set some parameterizations for $\mathcal{K}$. The simplest being a sum of polynomials

$$\mathcal{K}^{(J)-1}_{\alpha\beta}(E_{\mathrm{cm}}) = \sum_{k=0}^{N_{\alpha\beta}} c^{(Jk)}_{\alpha\beta} E^k_{\mathrm{cm}}, \tag{5.17}$$

where α and β are composite indices that each contain the quantum numbers orbital momentum L, total spin S, and channel a, and the $c^{(Jk)}_{\alpha\beta}$ form a real symmetric matrix for each k. Another common setup is to express the $\mathcal{K}$ matrix as a sum of poles with background

$$\mathcal{K}^{(J)}_{\alpha\beta}(E_{\mathrm{cm}}) = \sum_p \frac{g^{(Jp)}_\alpha g^{(Jp)}_\beta}{E^2_{\mathrm{cm}} - m^2_{Jp}} + \sum_k d^{(Jk)}_{\alpha\beta} E^k_{\mathrm{cm}}, \tag{5.18}$$

where the couplings $g^{(Jp)}_\alpha$ are real and the background coefficients $d^{(Jk)}_{\alpha\beta}$ form a real symmetric matrix for each k. These parametrizations can then be truncated later as needed.

A common parameterization used in our analyses, is the effective range expansion (ERE). The diagonal elements of the K-matrix are $K_L = \tan(\delta_L)$ where δ_L are the scattering phase shifts of the L-th partial wave. If one assumes a short-ranged potential in a single channel with spinless particles, the ERE is derived as

$$q^{-L-\frac{1}{2}}_{\mathrm{cm}} \mathcal{K}^{-1}_{\alpha\beta} = q^{-L-\frac{1}{2}}_{\mathrm{cm}} \cot \delta_L(q_{\mathrm{cm}}) = \sum_{n=0} c_{2n} q^{2n}_{\mathrm{cm}} = -\frac{1}{a_L} + \frac{r_L}{2} q^2_{\mathrm{cm}} + \mathcal{O}(q^4_{\mathrm{cm}}), \tag{5.19}$$

where $q_{\mathrm{cm}} = \sqrt{q^2_{\mathrm{cm}}}$, the constants a_L are the scattering lengths, and r_L are the effective ranges.

5.6 Block Diagonalization of LQC

Even in its new form, the LQC in Equation 5.15 still describes an infinite matrix with continuum quantum numbers. If, instead, we transform the basis into a basis in which both B and $\widetilde{K}$ are block diagonal and each block is truncated in the orbital angular momentum, then each block can be separately solved.

In order to block diagonalize, let us start with a symmetry transformation G which is defined as being a spatial rotation R or a spatial inversion I_s. The total momentum $\boldsymbol{P}$ changes to $G\boldsymbol{P}$ and if we define a unitary matrix $Q^{(G)}$ as

$$\left\langle J'm_{J'}L'S'a'|Q^{(G)}|Jm_JLSa\right\rangle = \begin{cases} \delta_{J'J}\delta_{L'L}\delta_{S'S}\delta_{a'a}D^{(J)}_{m_{J'}m_J}(R), & (G=R), \\ \delta_{J'J}\delta_{m_{J'}m_J}\delta_{L'L}\delta_{S'S}\delta_{a'a}(-1)^L, & (G=I_s), \end{cases} \tag{5.20}$$

where $D^{(J)}_{m'm}(R)$ are the Wigner rotation matrices, one can show that

$$B^{(G\boldsymbol{P})} = Q^{(G)}\ B^{(\boldsymbol{P})}\ Q^{(G)\dagger}. \tag{5.21}$$

Because $Q^{(G)}$ is unitary, $B^{(\boldsymbol{P})}$ is ensured to commute with $Q^{(G)}$ for all G in little group $\boldsymbol{P}$, and thus, we can simultaneously diagonalize $B^{(\boldsymbol{P})}$ and $Q^{(G)}$. By rotating into a basis constructed from the eigenvectors of $Q^{(G)}$, $B^{(\boldsymbol{P})}$ is consequently block diagonal because different eigenvectors of $Q^{(G)}$ must vanish within $B^{(\boldsymbol{P})}$.

A direct consequence of applying the symmetry transformations of G to the basis state $|Jm_JLSa\rangle$ is a projection into irreps. The symmetry transformations only mix indices of m_J and so the new basis-state indices will replace m_J,

$$|\Lambda\lambda nJLSa\rangle = \sum_{m_J} c^{J\eta;\,\Lambda\lambda n}_{m_J}\,|Jm_JLSa\rangle\,, \tag{5.22}$$

where $\eta = (-1)^L$ and n identifies each occurrence of Λ in $|Jm_JLSa\rangle$. The coefficients depend on irrep Λ, irrep row λ, J and η, and are independent of spin S and a. The method of calculating the transformation coefficients is outlined in [39], but I will note that B is diagonal in Λ, λ, spin S, and a:

$$\langle\Lambda'\lambda'n'J'L'S'a'|\,B^{(\boldsymbol{P})}\,|\Lambda\lambda nJLSa\rangle = \delta_{\Lambda'\Lambda}\delta_{\lambda'\lambda}\delta_{S'S}\delta_{a'a}\ B^{(\boldsymbol{P}\Lambda_B Sa)}_{J'L'n';\ JLn}(E). \tag{5.23}$$

Of course, we then want to represent $\widetilde{K}$ in the same basis. Due to orthonormality in the states between the bases m_J and Λ, $\widetilde{K}$ is diagonal in Λ, λ, n, and J. To identify the various blocks of B and $\widetilde{K}$, we can use a common diagonal index. In this case B and $\widetilde{K}$ share Λ and λ, and as I described earlier, the correlators of different irrep rows can be summed over, so our choice for labeling each block is to use Λ.

5.7 Minimization Methods

Finding the determinant of the LQC is not trivial. The techniques explored in our results are the *determinant residual method* and the *spectrum method*. Both utilize correlated-χ^2 minimization described in Section 4.3.

5.7.1 Determinant Residual Method

The determinant residual method uses the LQC itself to form residuals of a χ^2 function that is then minimized.

Using the LQC directly is not ideal because the determinant of large matrices can produce very large numbers. Using the principle that when one eigenvalue is zero, the determinant is zero, we can write a new function that is zero when the eigenvalue is zero, but is also limited to the range $[-1, 1]$

$$\Omega(\mu, A) \equiv \frac{\det(A)}{\det[(\mu^2 + AA^\dagger)^{1/2}]}. \tag{5.24}$$

Equation 5.24 renormalizes all eigenvalues such that the function is bounded. The scalar μ can be used to optimize minimization.

To minimize the LQC, we merely plug in the contents of the LQC

$$r_k = \Omega\Big(\mu, 1 - B^{(\boldsymbol{P})}(E^{(\text{obs})}_{\text{cm},k})\ \widetilde{K}(E^{(\text{obs})}_{\text{cm},k})\Big), \qquad (k = 1, \ldots, N_E), \tag{5.25}$$

where N_E is the number of energies in the given Λ and r_k are the residuals to be minimized. (Other variations of the LQC will also work as an input to Ω.) There is no advantage in introducing the energies, particle masses, and anisotropy as parameters, so they are left as lattice inputs. The only fit parameters needed are the parameters of the $\widetilde{K}$ or $\widetilde{K}^{-1}$ matrix elements which will generally be referenced as κ_j. The finite-volume spectrum can then be computed using the κ_j parameters and the LQC and compared to the original inputs.

This method has some advantages and disadvantages. One, the covariance matrix will need to be computed at each step of the minimization for the changing κ_j, but because the box matrix (dependent on finite-spectrum energies, particle masses, and anisotropy) will remain unchanged, the complicated RGL zeta functions are only computed at the initialization. Also, treating B as an observable can give physical insights into lattice QCD qualitative physics.

5.7.2 Spectrum Method

This method entails having the energies of the two-interacting particles in the center of mass $E_{\text{cm,k}}$, the masses of the particles m, the spatial length of the lattice L, and the anisotropy $\xi = a_s/a_t$ as both input to the model and as observables. The observations are either properties of the lattice or are measured from the correlators. The parameters are the same quantities but computed from the LQC.

The observations measured or set on the lattice are

$$\text{Observations } R_i\text{:} \quad \{E^{(\text{obs})}_{\text{cm},k},\ m^{(\text{obs})}_j,\ L^{(\text{obs})},\ \xi^{(\text{obs})}\ \}, \tag{5.26}$$

and the model parameters are,

$$\text{Model fit parameters } \alpha_k\text{:} \quad \{\ \kappa_i,\ m^{(\text{model})}_j,\ L^{(\text{model})},\ \xi^{(\text{model})}\ \}, \tag{5.27}$$

for $i = 1, \ldots, N_K$ and $j = 1, \ldots, N_p$, where N_K is the total number of parameters in the $\widetilde{K}$-matrix elements and N_p indicates the number of particle species. With each iteration, the model parameters are plugged into the LQC, then the energy E_{cm} is scanned until the determinant of the LQC is zero. These zero roots of the determinant must then be matched to the observed $E_{\text{cm},k}^{(\text{obs})}$. The roots are then defined as $E_{\text{cm},k}^{(\text{model})}$. The residuals for the minimization are

$$r_k = \begin{cases} E_{\text{cm},k}^{(\text{obs})} - E_{\text{cm},k}^{(\text{model})}, & (k = 1, \ldots, N_E), \\ m_{k'}^{(\text{obs})} - m_{k'}^{(\text{model})}, & (k = k' + N_E,\ k' = 1, \ldots, N_p), \\ L^{(\text{obs})} - L^{(\text{model})}, & (k = N_E + N_p + 1), \\ \xi^{(\text{obs})} - \xi^{(\text{model})}, & (k = N_E + N_p + 2). \end{cases} \tag{5.28}$$

In this case, both the RGL zeta functions and the covariance matrix are calculated throughout minimization, though to save computational cost, often an uncorrelated-χ^2 minimization is used instead.

Chapter 6

Computational Details

Both the $\Delta(1232)$ and $\Lambda(1405)$ were computed on a single lattice ensemble, the D200. Details are provided below. Due to the fine-tuning of the analysis process, there are some changes between the $\Delta(1232)$ and $\Lambda(1405)$ analyses. The way I determined the effect of autocorrelation on our results and the correlation functions used for the pion and kaon were both updated in the later $\Lambda(1405)$ analysis.

6.1 D200 Ensemble Computational Details

The D200 ensemble, generated by the Coordinated Lattice Simulations (CLS) consortium, utilizes the tree-level improved Lüscher-Weisz gauge action [24] and a non-perturbatively $O(a)$-improved Wilson fermion action [25]. This ensemble includes dynamical mass-degenerate u- and d-quarks, which are heavier than their physical counterparts, and an s-quark that is lighter than physical. This results in a pion mass $m_\pi \approx 200$ MeV and a kaon mass $m_\mathrm{K} \approx 487$ MeV, slightly different from their physical values of $m_\pi^\mathrm{phys} \approx 140$ MeV and $m_\mathrm{K}^\mathrm{phys} \approx 495$ MeV [68].

$(L/a)^3 \times T/a$	$64^3 \times 128$	af_π	0.04226(13)
N_meas	2000	af_K	0.04910(11)
am_η	0.1768(22)	$m_\pi L$	4.181(16)
a[fm]	0.0633(4)(6)		

Table 6.1: A summary of ensemble details and various decay constants (with normalization $f_\pi^\mathrm{phys} \approx 130$ MeV) for the CLS D200 gauge ensemble used in this work. The η mass is taken from Reference [69], and the decay constants of the pion and the kaon are obtained from Reference [70]. All other masses are determined in Figure 6.3.

This table also includes the η mass, as well as the pion and kaon decay constants. The hadrons used in this thesis are all stable under QCD and in the isospin limit with $m_u = m_d$. Due to the newly realized availability of some long-time single-hadron correlators that had been computed, the $\Lambda(1405)$ channel features a different

calculation of the single-hadron correlators.

To reduce the effect of autocorrelation on observables, open temporal boundary conditions are used [71]. All interpolating fields must be sufficiently distant from the boundaries to mitigate spurious contributions to the tail-end behavior of temporal correlation functions. An analysis of the single-pion at rest and ρ-meson correlators in Reference [72] indicates that a minimum distance of $m_\pi t_{\text{bnd}} \gtrsim 2$ is necessary to keep temporal boundary effects below the statistical errors in energy determinations. In both $\Delta(1232)$ and $\Lambda(1405)$ analyses, the correlator time ranges are such that $m_\pi t_{\text{bnd}} \gtrsim 2.3$.

The generation of the D200 ensemble, described in Reference [68], faces challenges due to low-lying eigenvalues of the Dirac matrix from either the light quark doublet or the strange quark, which can cause instabilities in the Hybrid Monte Carlo (HMC) or Rational Hybrid Monte Carlo (RHMC) algorithm [27]. This issue, addressed in Reference [73], is resolved by adding a "twisted mass" term to the action, the effect of which is removed through light- and strange-quark re-weighting [74]. Re-weighting factors, computed in Reference [75], are included in the analysis to convert the simulated action to the desired one. The lattice spacing is determined in Reference [76] and updated in Reference [77].

6.2 Rebin Analysis

For the D200 lattice, correlation function measurements are separated by four molecular dynamics units (MDUs). In the earlier study of the $\Delta(1232)$ resonance, I checked for signs of autocorrelation in the measurement of the variance of the correlators themselves, particularly, the most sensitive correlators, the pion and nucleon. To determine the effect of autocorrelations, the original measurements are rebinned by every N_{bin} samples. The dependence of the relative errors on N_{bin} for the single-nucleon and single-pion correlators is shown in Figure 6.1. Although evidence of autocorrelation was still found for $t/a \lesssim 8-10$ between $N_{\text{bin}} = 20$ and 40, these early timeslices are not used in the spectrum fits, suggesting that $N_{\text{bin}} = 20$ was sufficient to account for any autocorrelations in my energy determinations for the $\Delta(1232)$ study.

However, in the $\Lambda(1405)$ study, rather than using the variance of the correlators, I instead studied the variance on the results of the correlator fits. This analysis was shown as an example in Figure 2.3 of Section 2.3.4. There, I determined that $N_{\text{bin}} = 10$ was sufficient to account for autocorrelation effects in our results for the $\Lambda(1405)$ study.

Whenever applying the rebinning scheme, it was found that a negligible difference was observed on the mean and variance of the scattering amplitude calculations, but the χ^2 of the fits noticeably improved.

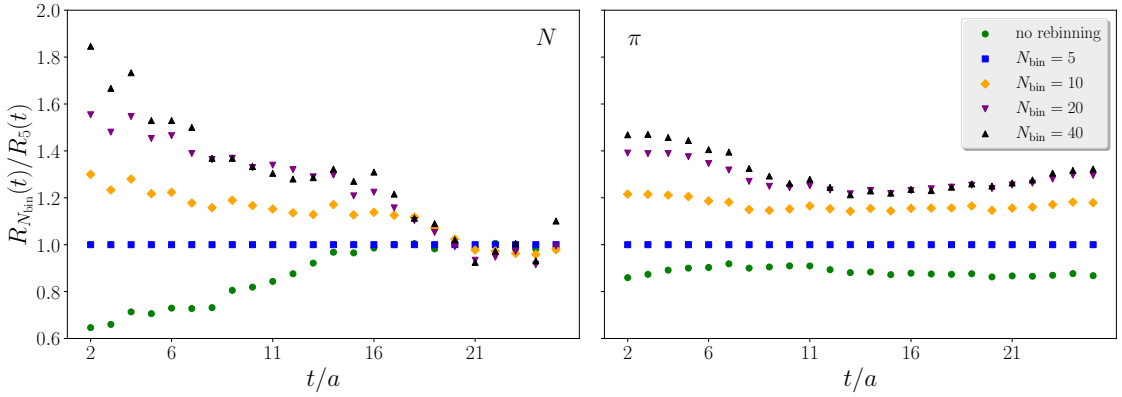

Figure 6.1: Relative error of the nucleon (left) and pion (right) correlators at rest, denoted $R_{N_{\rm bin}}(t)$, for several bin sizes $N_{\rm bin}$. All points are normalized by the $N_{\rm bin} = 5$ value with errors estimated using the bootstrap resampling method with $N_{\rm B} = 800$ resamples. $N_{\rm bin} = 20$ was chosen for the $\Delta(1232)$ analysis. Though there is still evidence of autocorrelation in the range $t/a \lesssim 8 - 10$, this range is not used in any subsequent fits.

6.3 Single Hadrons

The single hadrons for the pion and kaons were different between the $\Delta(1232)$ and $\Lambda(1405)$ analyses. For the $\Delta(1232)$, the correlators were calculated up to t/a-range of [2,25] and 4 sources were averaged over (sources referring to part of the quark line as described in Section 3.3) The single hadrons used for the $\Delta(1232)$ are shown in Figure 6.2. The fit choices were made according to the strategy described in Section 4.3.3, and the $t_{\rm min}$ plots used to aid this decision-making process are displayed along with the fits.

When beginning the $\Lambda(1405)$ analysis, I learned that longer time correlators for the kaon and pion had been computed (t/a=[2,40]) but only using 2 sources [36]. For forming the ratio correlators, the higher-precision short-time correlators were used, but to determine the masses, the longer time correlators provided us with valuable tail-end behavior. This led to slightly different determinations of the pion mass, and negligibly different fits for the other single-hadron masses. The fit differences are outlined in Table 6.2. Different fit preferences for the two analyses led to a nucleon with larger variance for the $\Lambda(1405)$ analysis. The single hadrons and the fit determinations used in the $\Lambda(1405)$ analysis are shown in Figure 6.3.

analysis	t-range	am_π	am_K	am_N	am_Σ	am_Λ
$\Delta(1232)$	[2a,25a]	0.06617(33)	0.15644(16)	0.3148(23)		
$\Lambda(1405)$	[2a,40a]	0.06533(25)	0.15602(16)	0.3143(37)	0.3830(19)	0.3634(14)

Table 6.2: Energy determinations for the resting single-hadron correlators for the two different sets of correlators used for the $\Delta(1232)$ and $\Lambda(1405)$ analyses.

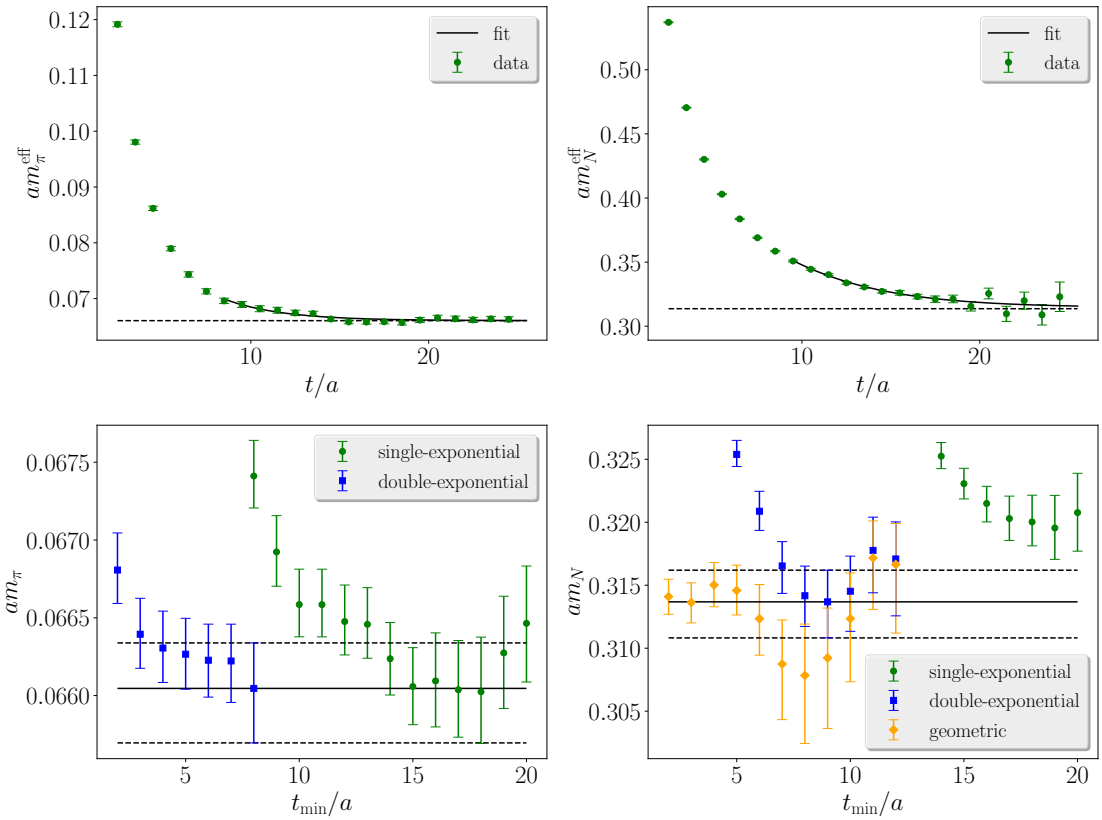

Figure 6.2: Fits to determine am_π and am_{N} for the $\Delta(1232)$ analysis. *Bottom row.* Variation of the fit range $[t_{\text{min}}, t_{\text{max}}]$ with $t_{\text{max}} = 25a$ for correlated-χ^2 fits. Both single- and two-exponential fits are shown and the horizontal band indicates the chosen fit and corresponding error. *Top row.* The effective masses of chosen two-exponential fits. *Left column.* Fit results associated with the pion. *Right column.* Fit results associated with the nucleon.

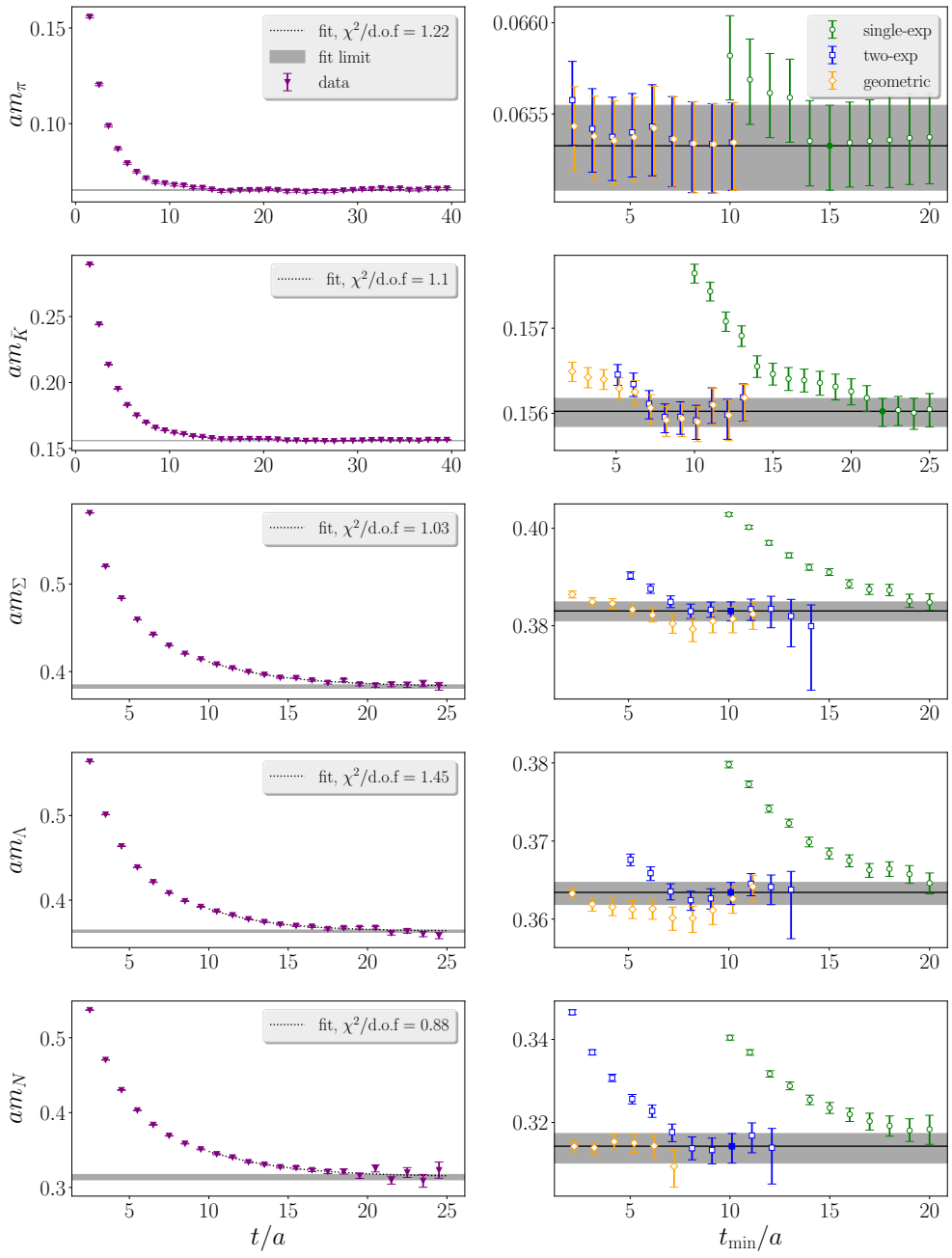

Figure 6.3: Determination of single-hadron masses for the $\Lambda(1405)$ analysis. Each row contains fit results to the single-hadron correlator indicated by the label on the vertical axis. *Left column.* The effective energy $\ln(C(t)/C(t+a))$ of the single hadron correlator overlayed by the chosen fit model (dashed lines). The horizontal band corresponds to the quoted mass and statistical error. *Right column.* A comparison of different fit forms and different t_{min} choices for fixed $t_{\mathrm{max}} = 35a$ for the pion and kaon and $t_{\mathrm{max}} = 25a$ for the other hadrons, with the chosen fit denoted by the horizontal band.

Chapter 7

$\Delta(1232)$ Resonance

High-precision calculations of the $\Delta(1232)$ resonance are of great interest for future neutrino-scattering physics and pose valuable constraints on effective field theories. Nucleon-pion interactions contribute largely to the long-range nuclear force and the binding of protons and neutrons in atomic nuclei. Due to the structure of future neutrino experiments, which will most likely rely on the scattering of neutrinos off of atoms with large nuclei, the nature of $N\pi$ scattering must be fully fleshed out for it will inevitably occur in these targets. The expected interactions include energies where the $\Delta(1232)$ can occur. Our study of this resonance, previously published in Reference [78], is presented in this chapter.

Although our focus was on the $\Delta(1232)$ resonance in the $I = 3/2$ $N\pi$ scattering channel, we also studied the $I = 1/2$ $N\pi$ scattering channel alongside it. To begin this process, operator bases must be decided to compute the correlation matrices. The operator bases used for this analysis included multihadron operators with constituents resembling π and N, and also baryon-type single-hadron operators resembling the channel quantum numbers were included. For the $I = 3/2$ $N\pi$ scattering channel, the single hadron resembled a Δ particle, and for the $I = 1/2$ $N\pi$ scattering channel, an N-type single hadron was used. All operators predicted to provide levels below the three-particle threshold plus a few more were included. A full detailed list of the operators is available in Appendix A. A deeper analysis of the finite-volume spectrum dependencies on the operators will be discussed in the next chapter.

7.1 Finite-Volume Spectrum

Ratio fits were chosen for all interacting levels. In my findings, they were stable in t_{min} and consistent with single- and double-exponential fits directly to the GEVP eigenvalues. They also had the benefit of generally providing more precise fit results. These t_{min}-plots are available in Figures B.1-B.6 in Appendix B.1.

In a similar vein to the stability analysis for the energy fits, I verified the choice of pivot parameters in the GEVP by analyzing and comparing to similar parameters.

Though the rule of thumb described in Section 4.2 tends to give accurate results, I verified this choice by varying the GEVP metric and diagonalization times (t_0, t_d) defined in Equation 4.9. The model and t-range for the fits for each energy level are kept the same. Furthermore, I also varied the dimension of the input correlation matrix N_{op}. Taking into account both GEVP stability and statistical precision, the parameters $(t_0, t_d) = (8a, 16a)$ are found to work well for both isospin channels. As shown in Figure 8.1, the spectrum is rather insensitive to variations in (t_0, t_d) and N_{op}.

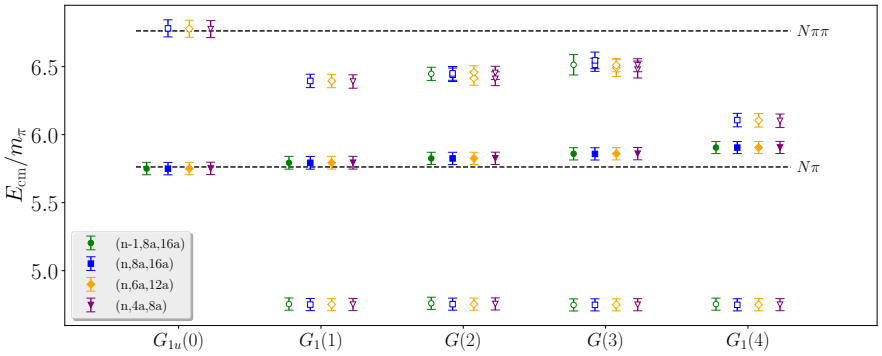

(a) the $I = 1/2$ spectrum.

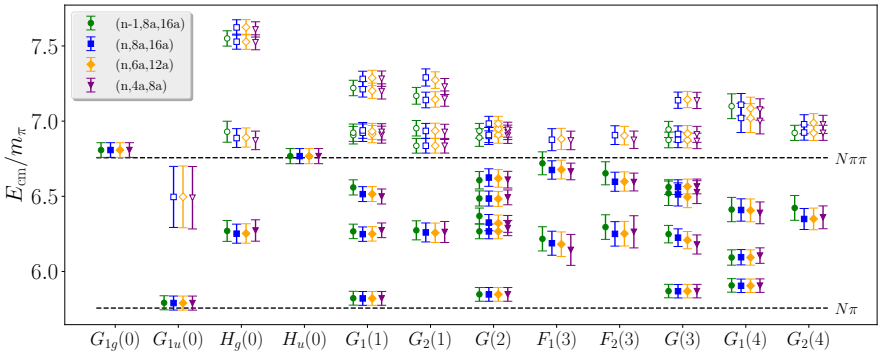

(b) the $I = 3/2$ spectrum.

Figure 7.1: Stability of the finite volume spectra calculated using the single pivot method with varying values for (N_{op}, t_0, t_d). Each irrep is shown in a column in the same manner as Figure 7.2 with n denoting the maximum N_{op}. Levels used in scattering-amplitude fits are indicated by solid symbols.

The spectra resulting from this analysis are shown in Figure 7.2b.

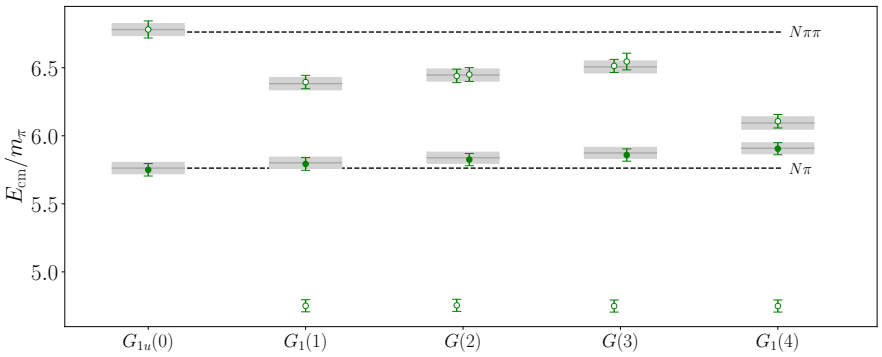

(a) The $I = 1/2$ spectrum.

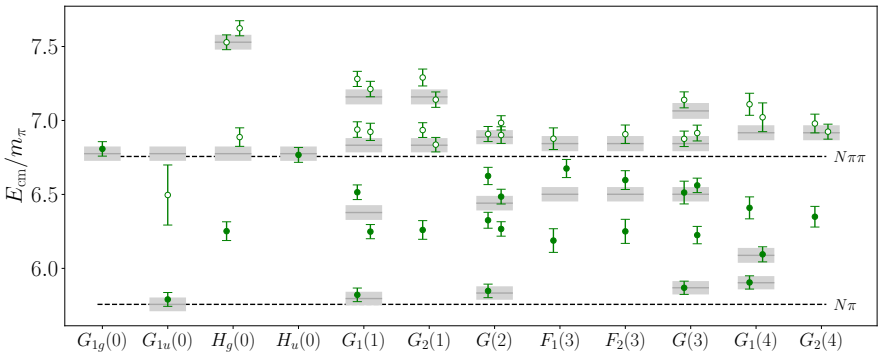

(b) The $I = 3/2$ spectrum.

Figure 7.2: The low-lying $I = 1/2$ and $I = 3/2$ nucleon-pion spectra in the center-of-momentum frame on the D200 ensemble described in Table 6.1. Each column corresponds to a particular irrep Λ of the little group of total momentum $\boldsymbol{P}^2 = (2\pi/L)^2\boldsymbol{d}^2$, denoted $\Lambda(\mathbf{d}^2)$. Dashed lines indicate the thresholds of the elastic region. Solid lines with grey bands represent non-interacting $N\pi$ levels and their associated statistical errors. Levels used in scattering-amplitude fits are indicated by solid symbols. For $I = 3/2$, all well-constrained levels with overlap below the $N\pi\pi$ threshold are included. For the $I = 1/2$ channel, due to limited information in the elastic region, we could only use the ground state in each irrep to determine the $I = 1/2$ amplitude near the $N\pi$ threshold.

7.2 Scattering Amplitudes

As explained in Section 5.6, the scattering fits can be truncated in ℓ for practical reasons. Based on the energy range and the number of available energy levels, we only consider energy levels associated with $\ell < 3$. The occurrence pattern of lowest-lying partial waves in the finite-volume irreps is given in Table 7.1.

Computing scattering results for nucleon-pion scattering presents additional difficulties compared to other scattering processes. First, due to the nonzero nucleon spin, two partial waves contribute for each non-zero ℓ, one with $J = \ell + 1/2$ and the other with $J = \ell - 1/2$. Secondly, the box matrix is not diagonal in ℓ, therefore there are mixings of different partial waves in the quantization condition. For $\ell_{\rm max} = 2$,

$\boldsymbol{d}$	Λ	dim.	contributing $(2J,\ell)^{n_{\text{occ}}}$ for $\ell_{\text{max}}=2$
$(0,0,0)$	$G_{1\text{u}}$	2	$(1,0)$
	$G_{1\text{g}}$	2	$(1,1)$
	H_{g}	4	$(3,1)$, $(5,2)$
	H_{u}	4	$(3,2)$, $5,2)$
	$G_{2\text{g}}$	2	$(5,2)$
$(0,0,n)$	G_1	2	$(1,0)$, $(1,1)$, $(3,1)$, $(3,2)$, $(5,2)$
	G_2	2	$(3,1)$, $(3,2)$, $(5,2)^2$
$(0,n,n)$	G	2	$(1,0)$, $(1,1)$, $(3,1)^2$, $(3,2)^2$, $(5,2)^3$
(n,n,n)	G	2	$(1,0)$, $(1,1)$, $(3,1)$, $(3,2)$, $(5,2)^2$
	F_1	1	$(3,1)$, $(3,2)$, $(5,2)$
	F_2	1	$(3,1)$, $(3,2)$, $(5,2)$

Table 7.1: A list of the lowest contributing partial waves for each irrep of the finite-volume little group Λ in the momentum class $\boldsymbol{d}$ used in this work. All partial waves with $\ell \leq \ell_{\text{max}}$ for $\ell_{\text{max}}=2$ are shown and each partial wave is denoted by $(2J,\ell)$. The superscript n_{occ} denotes the number of multiple occurrences (subductions) of the partial wave in the irrep. The pattern of partial-wave mixing is more complicated for irreps with non-zero total momentum as seen in this table.

energies E_{cm} in irreps with $\boldsymbol{d}^2=0$ determine the quantity $q_{\text{cm}}^{2\ell+1}\cot\delta_{J\ell}(E_{\text{cm}})$ for s- and p-waves, while these partial waves cannot be isolated for levels in irreps with non-zero total momentum. This complication requires global fits of all energies to determine the partial waves.

Our aim in this analysis is to describe the $J^P=1/2^-$ partial wave for both isospins and the $3/2^+$ wave with $I=3/2$. Conveniently, energies from irreps with zero total momentum directly provide points for these partial waves up to corrections from $\ell \geq 3$ contributions as seen in Table 7.1. However, mixing among various partial waves generally occurs for energies in irreps with non-zero total momentum. The zero-momentum points are therefore a useful guide when plotted together with the partial-wave fits.

Each partial wave is parametrized using the effective range expansion (ERE). For the $I=3/2$, $J^P=3/2^+$ wave, the next-to-leading order is included

$$\frac{q_{\text{cm}}^3}{m_\pi^3}\cot\delta_{3/2^+} = \frac{6\pi\sqrt{s}}{m_\pi^3 g_{\Delta,\text{BW}}^2}(m_\Delta^2 - s), \tag{7.1}$$

where $\sqrt{s}=E_{\text{cm}}=\sqrt{m_\pi^2+q_{\text{cm}}^2}+\sqrt{m_N^2+q_{\text{cm}}^2}$, and the standard effective range fit parameters are reorganized to conform to the conventional Breit-Wigner parameters of the $\Delta(1232)$ resonance, denoted $g_{\Delta,\text{BW}}^2$ and m_Δ. For all other waves, the leading-order effective range expansion is sufficient

$$\frac{q_{\text{cm}}^{2\ell+1}}{m_\pi^{2\ell+1}}\cot\delta_{J^P}^I = \frac{\sqrt{s}}{m_\pi A_{J^P}^I}, \tag{7.2}$$

where the overall $\sqrt{s}$ factors are adopted from standard continuum analysis [79], and the single fit parameter $A^I_{J^P}$ is related to the scattering length

$$m_\pi^{2\ell+1} a^I_{J^P} = \frac{m_\pi}{m_\pi + m_N} A^I_{J^P}. \tag{7.3}$$

For the $I = 3/2$ fits, the $J^P = 1/2^+$, $3/2^-$, and $5/2^-$ partial waves are added to the spectrum method fits along with lowest levels in the $G_{1g}(0)$ and $H_u(0)$ irreps. The $I = 3/2$ spectrum in the $G_{2g}(0)$ irrep and irreps in the $I = 1/2$ channel that do not contain the s-wave were not computed. This choice was made to reduce computational cost, although these irreps may be beneficial to further constrain higher partial waves in future work. The determinant residual method was found to be not as capable of constraining higher partial waves and was only used in fits that included just the $J^P = 1/2^-$, $3/2^+$ waves. Nonetheless, the consistency between these different fitting methods and those including higher partial waves indicates that uncertainties on amplitude parameters are dominated by statistics.

For the $I = 1/2$ channel, $\ell_{\max} = 0$ is employed. Although the small number of levels disallows a complicated model, the influence of higher waves can be explored by examining the influence of the highest-lying non-zero momentum energy level on the fit. Table 7.2 indicates that the effective range is insensitive to the omission of the $G_1(4)$ irrep level. These $I = 1/2$ fits were also insensitive to an additional term in the effective range expansion and showed no statistically significant difference between the spectrum and determinant-residual methods.

Fit	N_{pw}	$A_{1/2^-}$	χ^2	dofs
SP	1	0.82(12)	1.68	$5-1$
DR	1	0.92(22)	1.72	$5-1$
SP	1	0.82(13)	0.79	$4-1$

Table 7.2: Results for fits to the $I = 1/2$ spectrum in Figure 7.2a. N_{pw} is the number of partial waves included in the fit. Due to the small number of levels, all fits include only the $J^P = 1/2^-$ partial wave. Nonetheless, the effect of the omitted p-waves is estimated by removing the $G_1(4)$ level, which clearly has little influence on the result. 'SP' refers to the spectrum method, and 'DR' refers to the determinant-residual method.

Results from fits using both the spectrum and determinant-residual methods including various partial waves are given in Tables 7.2 and 7.3 for $I = 1/2$ and $I = 3/2$, respectively. In addition to the desired partial waves, fits using the spectrum method are mildly sensitive to the $J^P = 1/2^+$, $3/2^-$, and $5/2^-$ waves with $I = 3/2$. Although not included in the table, the fit results of the effective range parameter for both isospins are robust to the addition of the next term in the ERE. Results for the partial waves from the fit are shown with the points from the total-zero momentum irreps in Figures 7.3 and 7.4 for the $I = 3/2$ and $I = 1/2$ partial waves, respectively. The phase shift $\delta_{3/2^+}$ contains the characteristic profile of the $\Delta(1232)$ resonance and

Fit	N_{pw}	$A_{1/2^-}$	$g_{\Delta,\text{BW}}$	M_Δ/M_π	$A_{1/2^+}$	$A_{3/2^-}$	$A_{5/2^-}$	χ^2	dofs
SP	2	−1.56(4)	13.8(6)	6.281(16)	—	—	—	44.38	$23-3$
DR	2	−1.57(5)	14.4(5)	6.257(36)	—	—	—	14.91	$23-3$
SP	5	−1.53(4)	14.7(7)	6.290(18)	−0.19(6)	−0.46(12)	0.37(10)	30.17	$25-6$

Table 7.3: Results for the fits in the $I = 3/2$ channel. N_{pw} is the number of partial waves included in the fit. Two fit forms are presented, the one denoted $N_{\text{pw}} = 2$ includes only the desired partial waves, namely $J^P = 1/2^-$ and $3/2^+$, while the one with $N_{\text{pw}} = 5$ includes all s-, p-, and d-waves, adding two more energy levels from the $G_{1g}(0)$ and $H_u(0)$ irreps to the fit. For the $N_{\text{pw}} = 2$ fit, results from the determinant-residual method (DR) are shown in addition to the spectrum method (SP).

is shown in Figure 7.5. Because the s-wave scattering length was the only parameter of interest from the $I = 1/2$ spectrum, only the lowest nucleon-pion levels from each irrep are included in the fit, indicated by the solid symbols in Figure 7.2a. Investigation into the $J^P = 1/2^+$ wave containing the $N(1440)$ Roper resonance will likely require three-particle operators and the three-particle LQC for this particular pion mass.

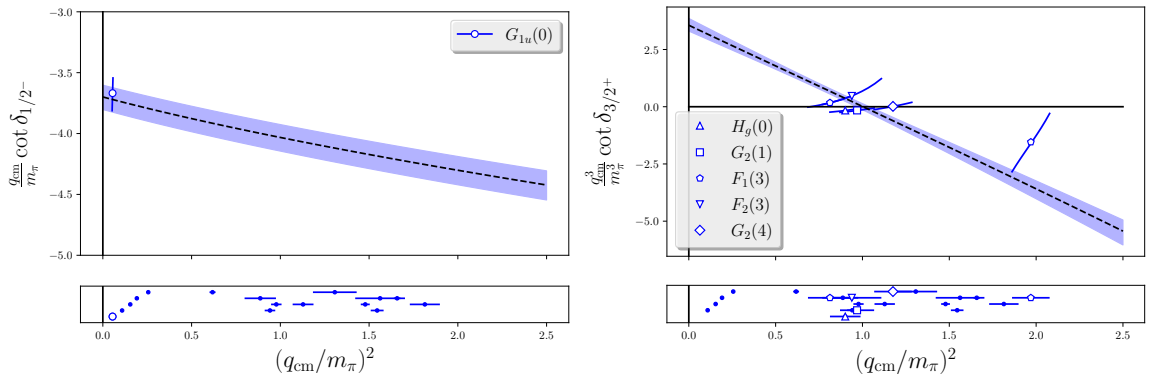

(a) $J^P = 1/2^-$ **(b)** $J^P = 3/2^+$

Figure 7.3: The results from fits to the $I = 3/2$ spectrum in Figure 7.2b using the spectrum method including the $J^P = 1/2^-, 3/2^+$ partial waves only, omitting the $H_u(0)$ and $G_{1g}(0)$ irreps. The lower panel of each partial wave shows the q^2_{cm} of the finite volume levels included in the fit, displaced vertically for visibility. Hollow symbols indicate energy levels that only couple to one partial wave. Solid symbols indicate energy levels that couple to more than one partial wave and therefore cannot be displayed in the upper plot (though it was used to constrain the fit).

Because the residuals of the spectrum method directly compare the E_{cm} of the finite volume and the E_{cm} of the LQC, the two resulting determinations of the spectrum can be compared. Such comparisons are shown in Figure 7.6 for both the $I = 1/2$ and $I = 3/2$ spectra. The ground states in the $G_{1g}(0)$ and $H_u(0)$ irreps are not shown on the plot and were only included in the $N_{\text{pw}} = 5$ fit in Table 7.3.

The final results for the scattering lengths in this work are taken from the deter-

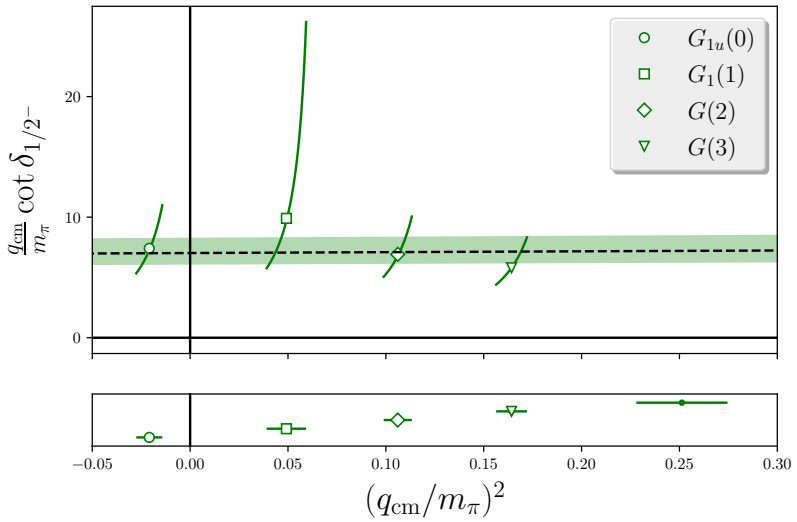

Figure 7.4: The result of fits to the $I = 1/2$ spectrum in Figure 7.2a to determine the scattering length of the $J^P = 1/2^-$ wave. As in Figure 7.3, the lower panel shows the input spectra, displaced vertically for visibility. For $\ell_{\rm max} = 0$, even levels with total non-zero momentum did not display any partial wave mixing and therefore could be added to the upper panel. The level with largest $q^2_{\rm cm}$ is not shown in the upper panel due to its large error.

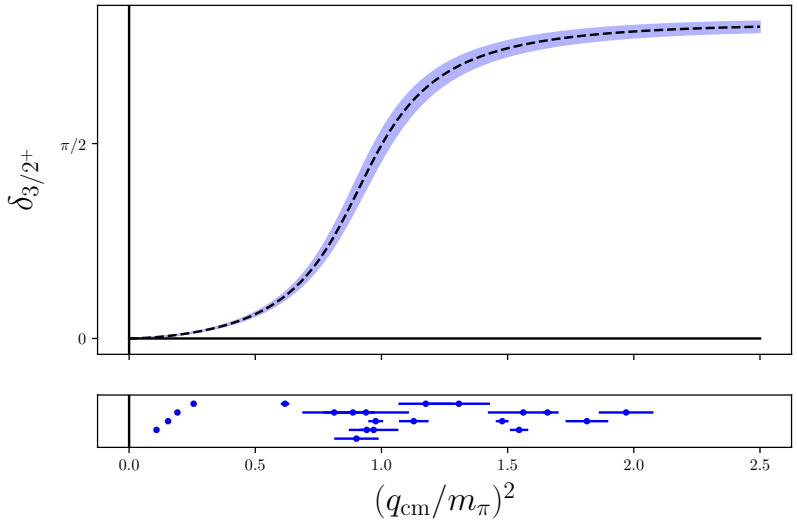

Figure 7.5: Scattering phase shift of the $I = 3/2$, $J^P = 3/2^+$ partial wave containing the $\Delta(1232)$ resonance. The curve is obtained from a fit of the finite-volume energies shown in the lower panel using the LQC and a Breit-Wigner form. Levels used in the fit are shown in the lower panel, similar to Figures 7.3 and 7.4, and omitted from the upper plot for clarity.

minant residual method fit in Table 7.3 with $N_{\rm pw} = 2$ for $I = 3/2$ and the spectrum

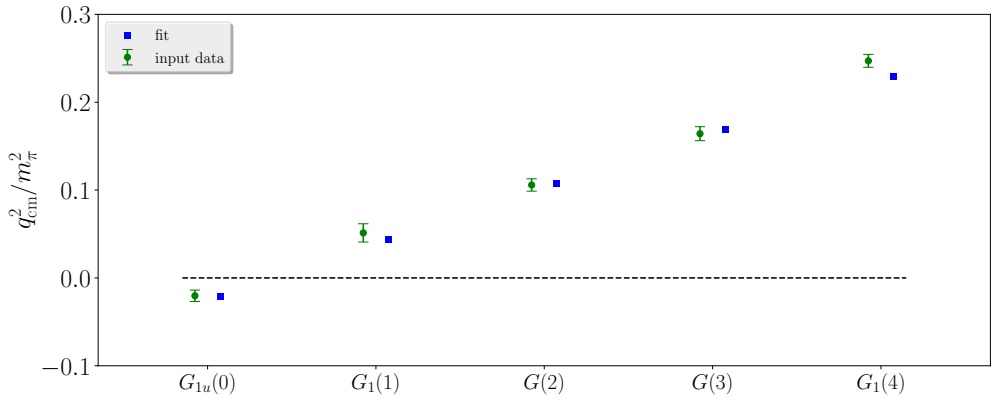

(a) The $I = 1/2$ spectrum compared with model values.

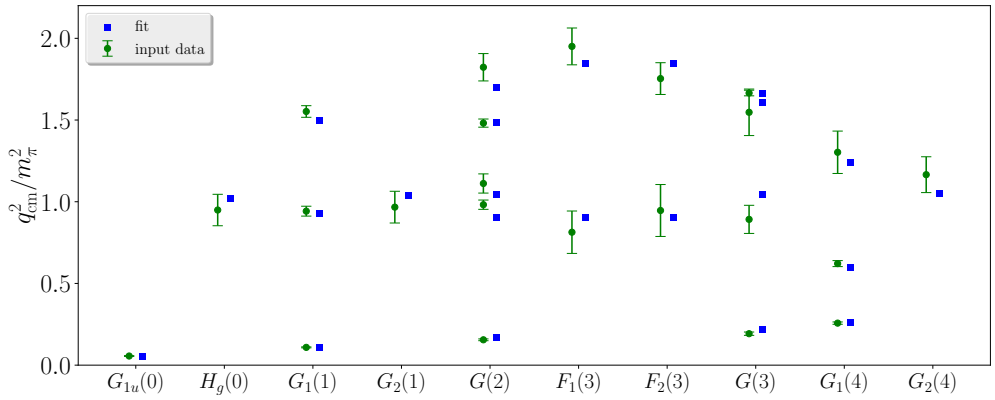

(b) The $I = 3/2$ spectrum compared with model values.

Figure 7.6: The center-of-mass momentum $q^2_{\rm cm}/m^2_\pi$ for the $I = 1/2$ and $I = 3/2$ spectra together with model values from spectrum method fits with $N_{\rm pw} = 2$ partial waves for $I = 3/2$. For $I = 1/2$, only the s-wave is included and the spectrum method fit to all five points is shown.

method fit for $I = 1/2$ including all five levels

$$m_\pi a_0^{3/2} = -0.2735(81)\,, \qquad m_\pi a_0^{1/2} = 0.142(22). \tag{7.4}$$

In Figure 7.7, the results from this work for the Breit-Wigner parameters of the $\Delta(1232)$ resonance in the $I = 3/2$, $J^P = 3/2^+$ partial wave are compared to the published numbers in References [5] and [80] where, as is customary, the definition of the $g_{\Delta N\pi}$ coupling from leading-order effective field theory is used, as defined in Equation 39 of Reference [80]. The quark mass trajectory in Figure 7.7 used in these results and in Reference [5] fixes the sum of the quark masses, and differs from that used in Reference [80], which fixes the strange quark mass to its physical value. The scattering lengths determined in this analysis are compared to past lattice QCD results in Figure 7.7.

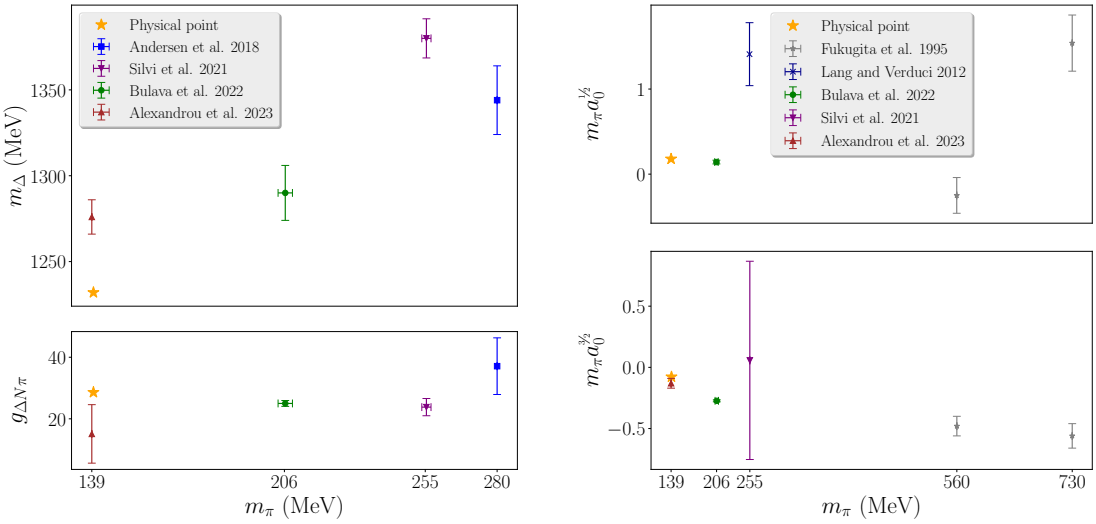

Figure 7.7: Comparison of results from the $\Delta(1232)$ analysis to previous lattice calculations. The work described in this thesis is indicated by 'Bulava et al. 2022'. Other results are indicated by 'Alexandrou et al. 2023' [81], 'Anderson et al. 2018' [5], 'Silvi et al. 2021' [80], 'Fukugita et al. 1995' [82], and 'Lang and Verduci 2012' [83]. Physical point values were calculated using References [9, 84, 85]. Error bars for the physical point were not calculated. Figure taken from Reference [86]. *Top left.* The Breit-Wigner mass m_Δ. *Bottom left.* The coupling $g_{\Delta N\pi}$ from leading-order effective field theory. *Top right.* The $N\pi$ isodoublet scattering length $m_\pi a_0^{1/2}$ in terms of the pion mass. *Bottom right.* The $N\pi$ isoquartet scattering length $m_\pi a_0^{3/2}$.

7.3 New Method for Detecting Missing Energies

Although the energy spectrum is independent of our choice of operators, our ability to extract the spectrum is strongly dependent on the operators used. The GEVP method must not only be linearly independent, but it must include enough operators such that when acting on the vacuum there is at least one operator that produces a state for each of the N lowest energies of the spectrum. Furthermore, the mappings between the energy levels produced and the operators associated with them must also be linearly independent. If any of these requirements are violated, then the resulting spectrum determination is incorrect and there will be levels missing. These cases will be outlined in the next section.

In order to robustly check for missing levels, it is recommended to add more operators to the operator basis and expand the correlator matrix. The states produced by the operator's action on the vacuum are generally predictable using the non-interacting levels as a reference. Though this method is the most robust method, it can also be computationally expensive, and for reasons later mentioned, the needed operators may not be straightforward or obvious.

Currently, the only method known to the author to determine if the spectrum is incorrect after one has already computed the correlators is if the scattering-amplitude

fits fail to capture well-determined physics. Because the volume dependence and quark-mass dependence of lattice QCD results are not always known for a quantity, and lattice QCD is continually searching beyond scattering channels where there is no experimental data, abnormalities in the scattering-amplitude fits cannot be relied upon for verification of the finite volume spectrum.

To ensure we obtain all of the levels in the energy range of interest, we generally calculate all possible single-hadron and multi-hadron operators (meson and baryon combinations) expected to be within the elastic scattering range plus a few more to be safe. A recent analysis [86] showed that a tetraquark operator is a vital operator in some two-meson scattering channels even where no tetraquark resonances were expected. This tetraquark study gives us another reminder that there is much we still have yet to understand about the nature of QCD.

In almost all meson-baryon scattering analyses, hadronic states with four or more quarks are ignored, including the ones presented in this thesis, but due to the limitless potential quark configurations for hadrons, there is a possibility that a complicated hadron could contribute in any channel. A robust method to test this is to compute the additional correlation matrices that include the hadron operator with the large number of quarks, but the exotic operator is both cumbersome to calculate and computationally expensive to compute compared to the simple mesons and baryons. Therefore, I thought I would experiment with the $\Delta(1232)$ $I = 3/2$ channel to better understand the effect of missing operators and find a way to detect it using the incomplete correlation matrix and spectrum. The $\Delta(1232)$ channel serves as a good test bed for such a method due to its relative simplicity (only one resonance and only one scattering channel) and high statistics.

7.3.1 Spectrum Extraction with Δ Operators Excluded

In this experiment, to understand the effects of missing operators, I studied the irreps in which the Δ operator contributed. For each of the bases, I used the same pivot parameters for solving the GEVP on the correlator matrices, one with the complete operator basis, and one truncated to only include the πN multi-hadron operators. The fit forms and t-ranges were also set to be the same for each resulting level. Those two spectrum determinations are compared in Figure 7.8. As one can see, when the Δ operators are excluded from the operator basis of the correlation matrix, then the resulting set of energy levels is missing levels in the elastic scattering range and appears to be more weakly interacting.

To illustrate how the GEVP solution is missing levels, I compared a few of the computed operator overlaps for $G_1(1)$ irrep for each set of operators in Figure 7.9. Figures 7.9b and 7.9c show that the diagonal correlators containing the $\pi(1)N(0)_0$ and Δ operators have contributions from the second and third energy levels of the spectrum. These two operators are the only ones with overlaps onto these two levels, so when the Δ is omitted, the $\pi(1)N(0)_0$ operator is the only operator with infor-

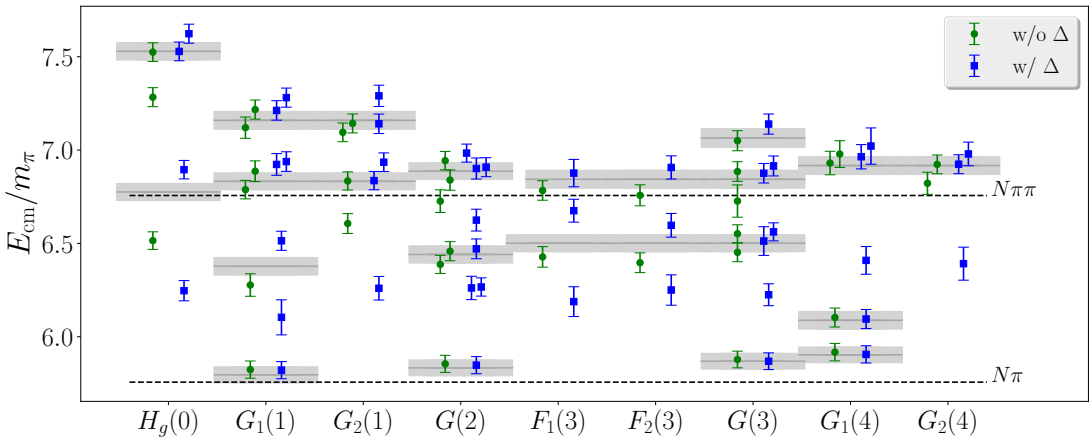

Figure 7.8: A comparison of the spectrum determinations where all operators are included in the operator basis and when the Δ operators are missing from the operator basis. The label 'w/ Δ' indicates that the Δ operators were included. The labels 'w/o Δ' indicates that all the Δ operators were removed from the operator bases.

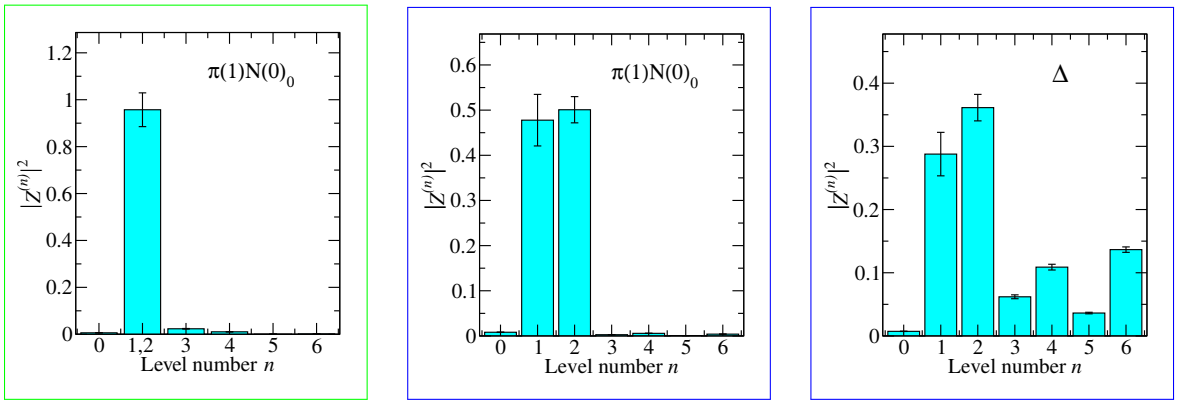

(a) Basis with no Δ. **(b)** Basis with Δ. **(c)** Basis with Δ.

Figure 7.9: Operator overlaps of operators where Δ operator was included and excluded in the basis. $I = 3/2$ $\pi(1)N(0)_0$ operator overlap factors without **(a)** and with **(b)** the Δ operator included in the operator basis of the correlation matrix. **(c)** Δ operator overlap factors. Magnitudes are normalized based on the sum of the level of each operator and level-number ordering is based on increasing final-energy fit values of the spectrum including the Δ operator.

mation about these two levels. Solving the GEVP cannot discern this, and thus it combines the information of these two levels, appearing as one.

In the provided example, the correlators associated with the $\pi(1)N(0)_0$ operator contain information about more than one level. Even if the Δ operator is not included, the information is still there. This may provide a means of detecting missing levels.

The example outlined in this section is not a universal rule. Many of the multi-hadron operators only overlap with one level; therefore, if omitted from the basis, the

information about that level would not appear anywhere in the correlation matrix. But when it comes to resonance operators, generally they mix with many levels and are not the sole operator that overlaps with any given level. This is also not a firm rule of behavior. In these cases, the only way to discover if there is a new level in the energy range of interest is to add the operator to the basis and test. Any test on the GEVP results cannot guarantee that the spectrum is complete, but it may increase confidence in the spectrum achieved.

The goal here is to try to generate a method that can alert us to the probability of a missing energy level for the case shown in Figure 7.9.

7.3.2 Toy Correlators

First, to confidently test any method and control the mitigating factors such as Monte Carlo fluctuations and higher-state contamination, based on the resulting operator overlaps and the finite volume energies from the solution of the GEVP, I generated toy correlators,

$$C_{\text{toy},ij} = \sum_{n}^{N} |Z_i^{(n)}||Z_j^{(n)}|e^{-E_n t}, \tag{7.5}$$

where $|Z_i^{(n)}|$ and E_n are the values determined using the GEVP solution determined in Section 7.1. This does not recreate the original correlator matrices of the $\Delta(1232)$ analysis, but it does serve as a test bed for new missing-operator detection methods. A couple examples of the GEVP solution's reconstructed correlators compared to the original data can be seen in Figure 7.10.

Using these zero-noise, uncontaminated toy correlators, I can repeat the steps in the last section and remove the Δ operators from the basis and then compare the resulting spectrum determination to the full-basis results. In this instance, I only remove one Δ operator from each basis to further control each test case. Though it is trivial to obtain the spectrum from the full set of toy correlators, the toy correlators with and without Δ operator are compared to the real calculations with and without a Δ operator in Figure 7.11.

After reproducing the spectrum determinations with the toy correlators using the full and truncated operator bases, we can repeat the reconstruction of the correlators using the GEVP solution again. Naturally, this is, again, trivial for the full basis, as it merely recreates the toy correlator. But for the case of the spectrum calculated from a truncated basis, there is a notable difference between the truncated recreation and the original toy correlator. Some examples are shown in Figures 7.12a-7.12c. This change in general slope does not occur for every correlator as seen in Figure 7.12d, but there is at least one correlator in every basis that sees the slope change.

This effect in the truncated basis results is promising, for it indicated that despite not having any information about the operator, there still seems to be a real effect of the missing operator on the resulting GEVP solutions. Whether or not this effect

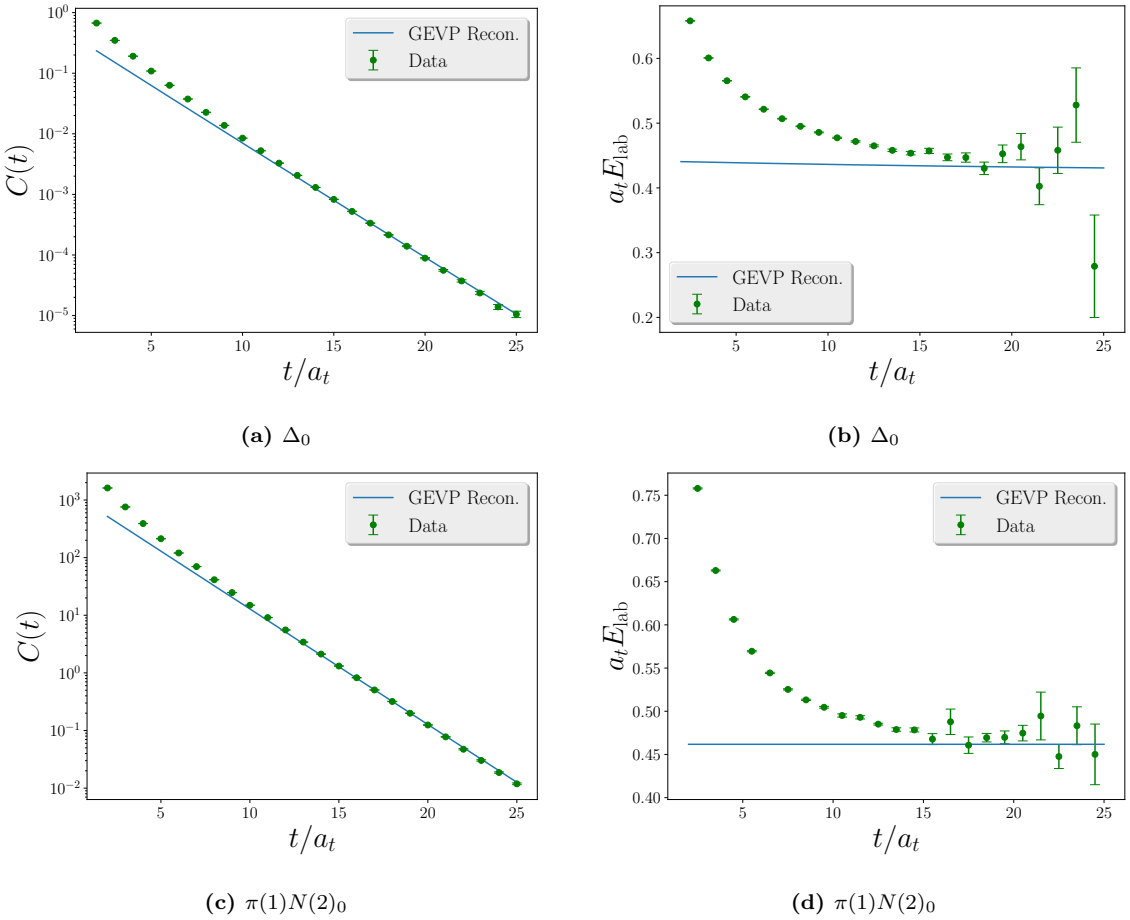

(a) Δ_0 **(b)** Δ_0

(c) $\pi(1)N(2)_0$ **(d)** $\pi(1)N(2)_0$

Figure 7.10: Example GEVP solution reconstructions of the diagonal correlators of the $G_2(1)$ irrep. The line indicates the reconstructed correlator and the markers with error bars indicate the original correlator data. **(a)** and **(b)** contain the diagonal single-hadron Δ_0 correlator. **(c)** and **(d)** contain the diagonal multi-hadron $\pi(1)N(2)_0$ correlator.

is discernible when contamination and noise is present is the more interesting question. It is simple enough to add either effect to the calculations, but I will limit my investigations to the noise.

To test whether the noise will influence this slope feature, I compared the GEVP solution reconstruction and then added noise to the correlator. The noise was generated using a normal distribution around zero with a spread of $R \min(C(t))$ for each correlator. The noisy correlator is then fitted with a simple linear regression to estimate the slope of the noisy correlator. Using the GEVP solution reconstruction with the full basis, the results can be seen in Figure 7.13. $R = 0.01$ suffices to simulate the average Monte Carlo noise seen in the resulting correlators of the $\Delta(1232)$ analysis. As shown in Figure 7.13, as the noise is increased, the estimation of the effective energy slope increasingly diverges from the true slope. Any slope deviation due to a

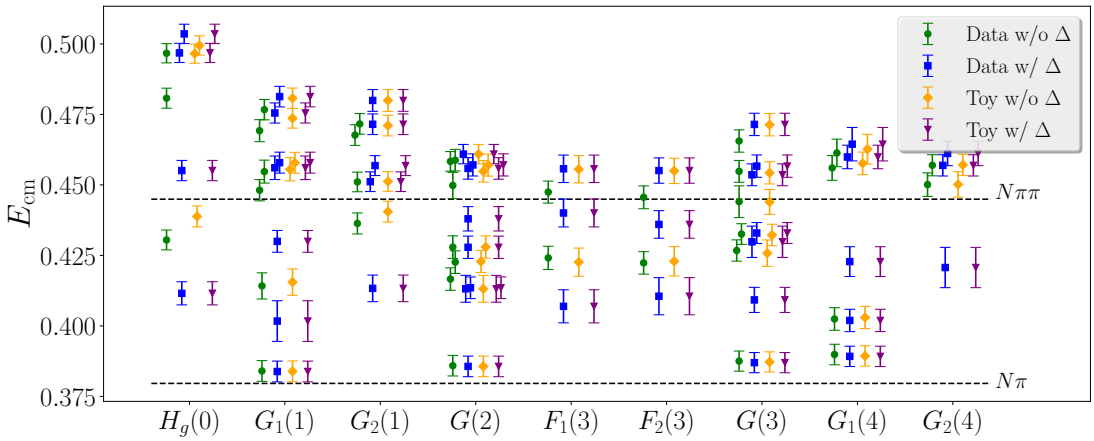

Figure 7.11: A comparison of the spectrum determinations where all operators are included in the operator basis and when one Δ operator is missing from the operator basis using both real correlator and the toy correlators. The label 'w/ Δ' indicates that the Δ operators were included. The labels 'w/o Δ' indicates that *one* Δ operator was removed from each operator basis. The label 'Data' indicates that the spectrum was computed from the Monte Carlo correlators. The label 'Toy' indicates that the spectrum was computed from the GEVP solution reconstructed correlators.

missing level is likely to be misrepresented due to the noise.

7.3.3 Spectrum Check Fits

Another method I developed and tested was a fitting scheme. Based on the expectation when there is a missing operator, the GEVP solution of a basis with N operators is estimating the contribution of two levels as

$$A_m e^{-E_m t} + A_{m+1} e^{-E_{m+1} t} \approx A_{\text{sum}} e^{-E_{\text{sum}}} \tag{7.6}$$

where index $0 \leq m < N-1$ and A_{sum} and E_{sum} are some composite of the original parameters. Using this premise, I constructed the fit form in assumption that there are two levels being approximated as one,

$$C(t) = A_m \left(R e^{-(E_m - \delta)t} + (1-R) e^{-(E_m + \delta)t} \right) + \sum_{n=0, n\neq m}^{N-1} A_n e^{-E_n t}, \tag{7.7}$$

where $0 \leq m < N-1$, δ and R are parameters, and A_i and E_i are the operator overlaps and energies of the GEVP solution. R is bounded within the range $[0, 1]$.

Though Equation 7.7 would not be able to accurately determine the true levels and overlaps (for this is impossible without the needed operator in the basis), it may be able to determine flexibility in the spectrum. To verify this test, I will fit the toy correlators using the solution generated with and without a Δ operator included. The

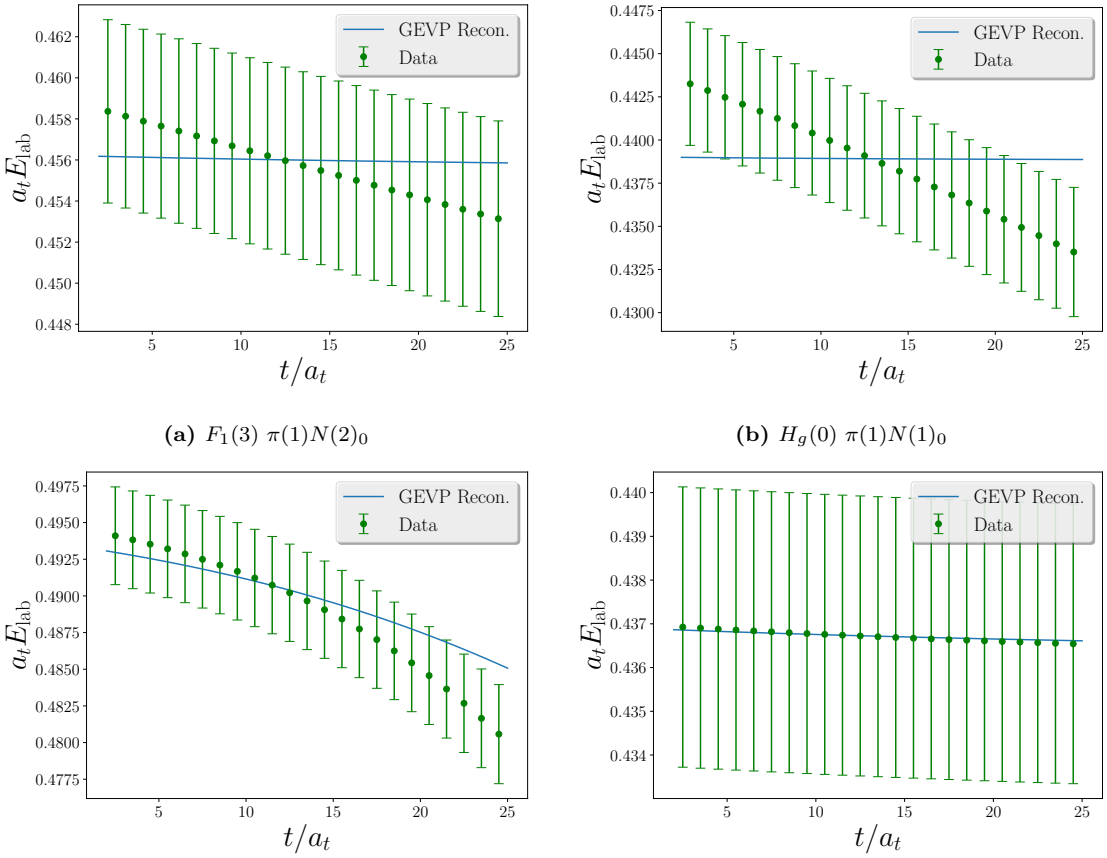

(a) $F_1(3)$ $\pi(1)N(2)_0$

(b) $H_g(0)$ $\pi(1)N(1)_0$

(c) $H_g(0)$ $\pi(2)N(2)_0$

(d) $G_1(4)$ $\pi(0)N(4)_0$

Figure 7.12: A comparison of the GEVP reconstruction using the full basis of the original diagonal correlators to a reconstruction of the toy correlator using the GEVP solution of the toy correlators using the truncated operator bases. The label 'Data' in this plot indicates the toy correlators (error bars are estimated by resampling). The label 'GEVP Recon.' indicates the reconstruction using the truncated operator basis. Captions include the irrep and then the name of the original diagonal correlator being reconstructed.

results of the fit to toy correlators from the $G(3)$ irrep are shown in Figure 7.14, where the fitted energy spectrum for each available operator is shown. The level m chosen for each fit to a given diagonal correlator was chosen based on the level at which the operator maximally overlaps. The diagonal correlator corresponding to the operator with maximal overlap to the highest level $N-1$ was omitted, for the highest levels of the spectrum are poorly determined anyway. The results for all operators of all bases are available in Appendix D. In the $G(3)$ irrep and all the others, the flexibility δ was found to be large (larger than the estimated resampling error of the mth energy level) in at least one of the fits to a given diagonal correlator of the truncated GEVP solution. For the GEVP solution with the full basis, there was no instance of a large δ.

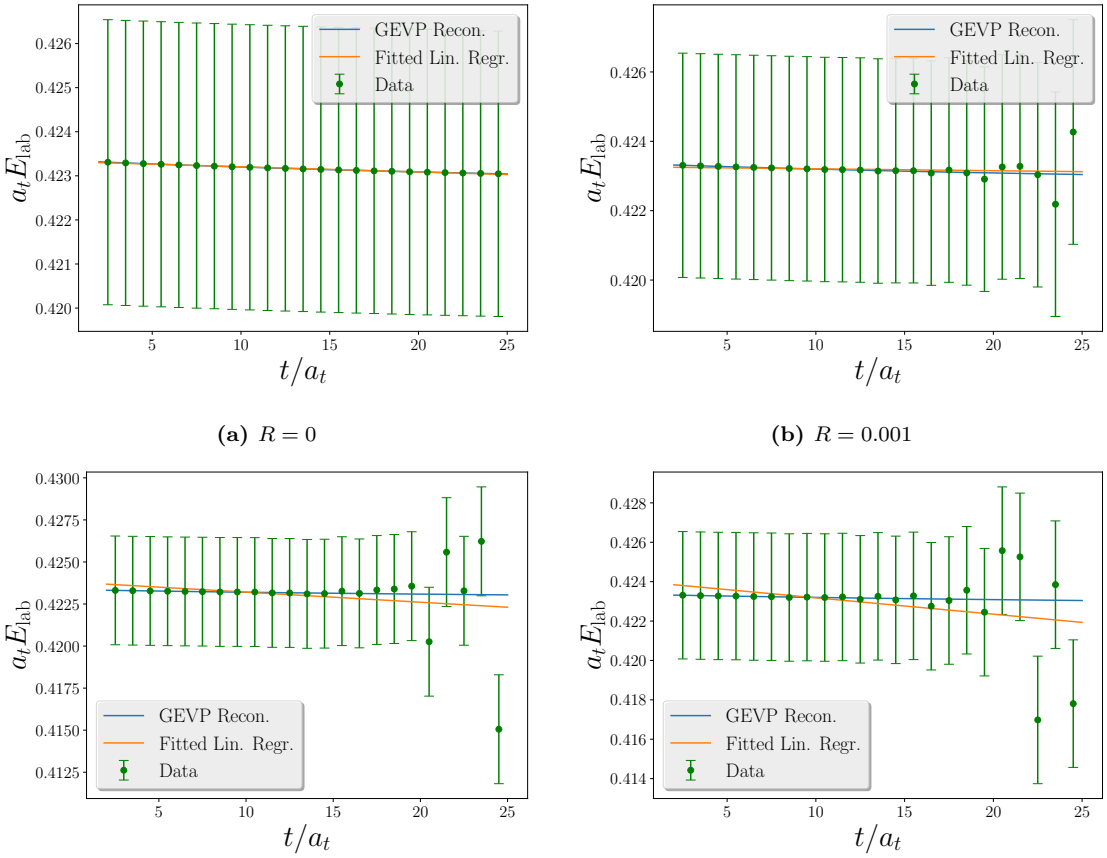

(a) $R = 0$ **(b)** $R = 0.001$

(c) $R = 0.005$ **(d)** $R = 0.01$

Figure 7.13: Effective energy of GEVP solution reconstruction of the $\pi(0)N(3)_0$ operator with irrep $G(3)$. The exact reconstruction is represented by the blue line and plot label 'GEVP Recon.' The GEVP solution reconstruction with added noise is indicated by markers (with errors estimated by resampling) and labeled as 'Data'. A linear regression fit to the GEVP solution reconstruction with added noise is labeled by 'Fitted Lin. Regr.'

Though the test is successful for the ideal toy correlators, when noise is introduced, the fit test begins to fail. In Figure 7.15, noise is introduced to the toy correlators being fitted to with $R = 0.001$ and 0.01. Though at $R = 0.001$, δ is still small, Figure 7.15b shows false positives within the full-basis toy spectrum at $R = 0.01$.

Despite these two tests working thoroughly in the ideal case, they begin to fail as soon as noise is introduced. The probability of successful or unsuccessful detection should be determined by the magnitude of noise present in the correlator, though this determination is saved for a future study. It would be preferable to improve upon this test or develop another such that it maintains accuracy with larger noise fluctuations.

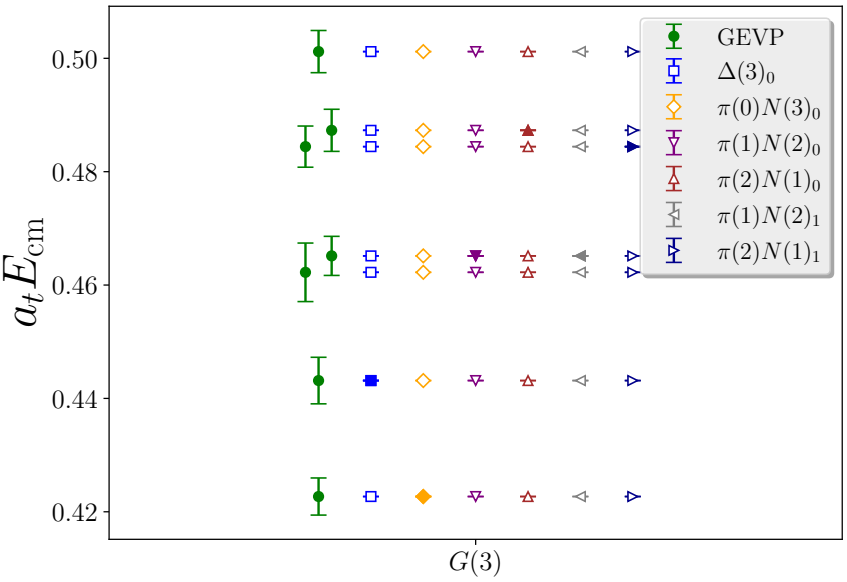

(a) Spectrum and fit results calculated from the full basis of toy correlators.

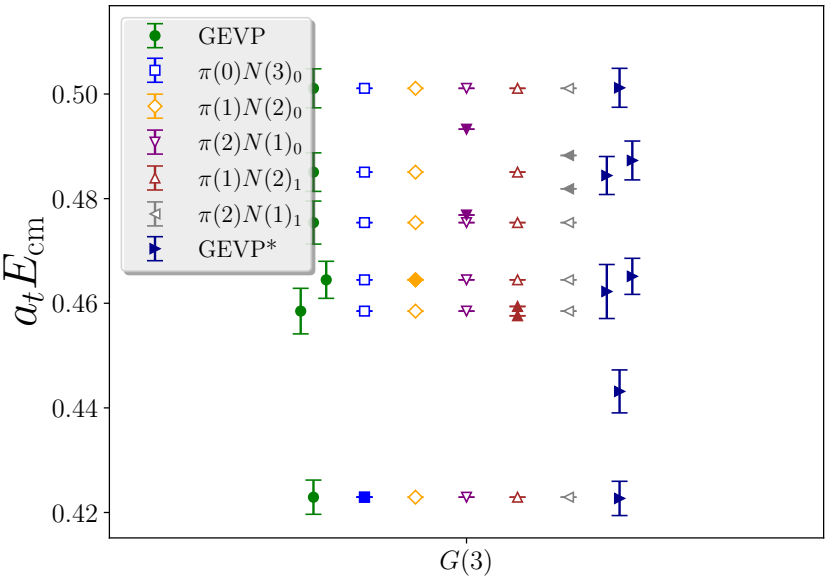

(b) Spectrum and fit results calculated from the truncated basis of toy correlators. Label 'GEVP*' is the original spectrum for reference.

Figure 7.14: Fits to the toy correlators using spectrum determinations calculated from the full and truncated correlation matrices. The fit form is Equation 7.7 and levels $E_m - \delta$ and $E_m + \delta$ are indicated by the filled symbols for each spectrum. The operator names indicate the flavor structure and the projected momentum on each constituent hadron. The index attached to each operator corresponds to its Clebsch-Gordan index.

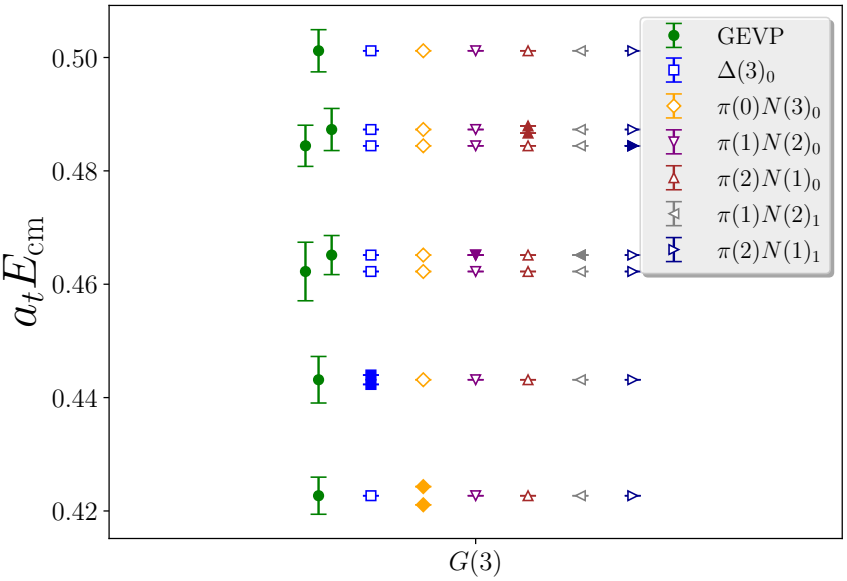

(a) Spectrum and fit results calculated from the full basis of toy correlators with $R = 0.001$.

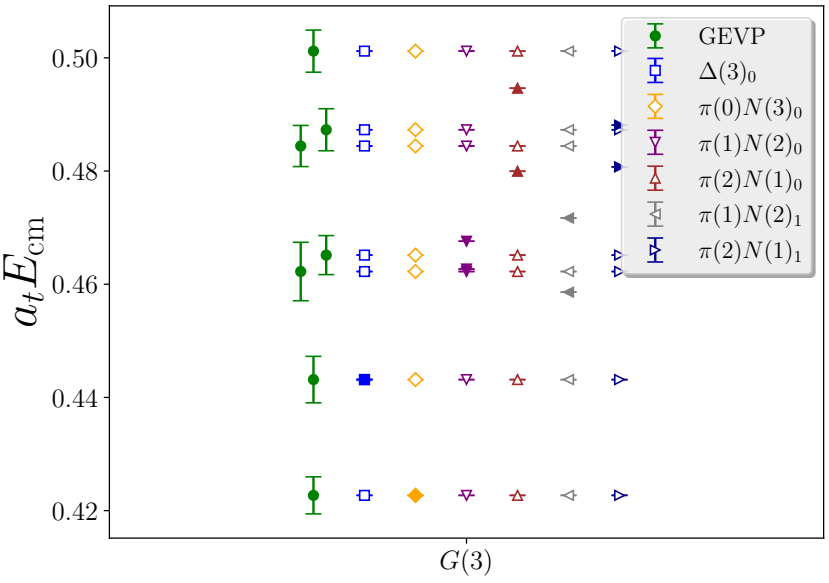

(b) Spectrum and fit results calculated from the full basis of toy correlators with $R = 0.01$

Figure 7.15: Fits to the toy correlators using spectrum determinations calculated from the full and truncated correlation matrices with added noise. The fit form is Equation 7.7 and levels $E_m - \delta$ and $E_m + \delta$ are indicated by the filled symbols for each spectrum.

Chapter 8

$\Lambda(1405)$ Resonance

The $\Lambda(1405)$ resonance is a difficult resonance to study because it appears in both $\pi\Sigma$ scattering and $\bar{K}N$ scattering. In order to understand the properties of $\Lambda(1405)$, we must incorporate both scattering channels into our analysis beginning with the operator basis used for our correlator matrices. The interacting operators used in our correlators included $\pi\Sigma$ and $\bar{K}N$ multi-hadron operators as well as the Λ single hadron operator. A detailed list is provided in Appendix A.

Including all of the possible single- and multi-hadron operators makes us confident that we have enough operators that map onto all levels below the three-particle threshold. The complete procedure for this analysis of the $\Lambda(1405)$ resonance is described in great detail in the previous chapters of this text, and specific details about the ensemble and calculation can be found in Section 6.1. This work was simultaneously published in References [18, 19].

8.1 Finite-Volume Spectrum

Figure 8.1 shows center-of-mass-frame energy determinations in four symmetry channels for various GEVP methods. I compare two different choices of t_d in the single pivot method alongside the "Rolling Pivot M" which is the rolling pivot described in Section 4.2.2. To confirm my results, a collaborator computed the spectrum using the "Rolling Pivot B" method. The distinction between "Rolling Pivot M" and "Rolling Pivot B" is that the former computes the GEVP on the mean of every time slice, but then the pivot computed there is applied to the bootstrap samples. In the latter case, the GEVP is solved on every time slice as well as on every sample. The simplest single-pivot method produces nearly identical results to the other two more complicated methods as long as the variables t_0 and t_d are stable with variation. Based on these requirements, the choice of pivot for final results was the single-pivot method with $t_0 = 4a$ and $t_\mathrm{d} = 16a$, though it is reassuring that the more intensive methods confirm our findings.

To select a final result for each finite-volume spectrum level, I applied several

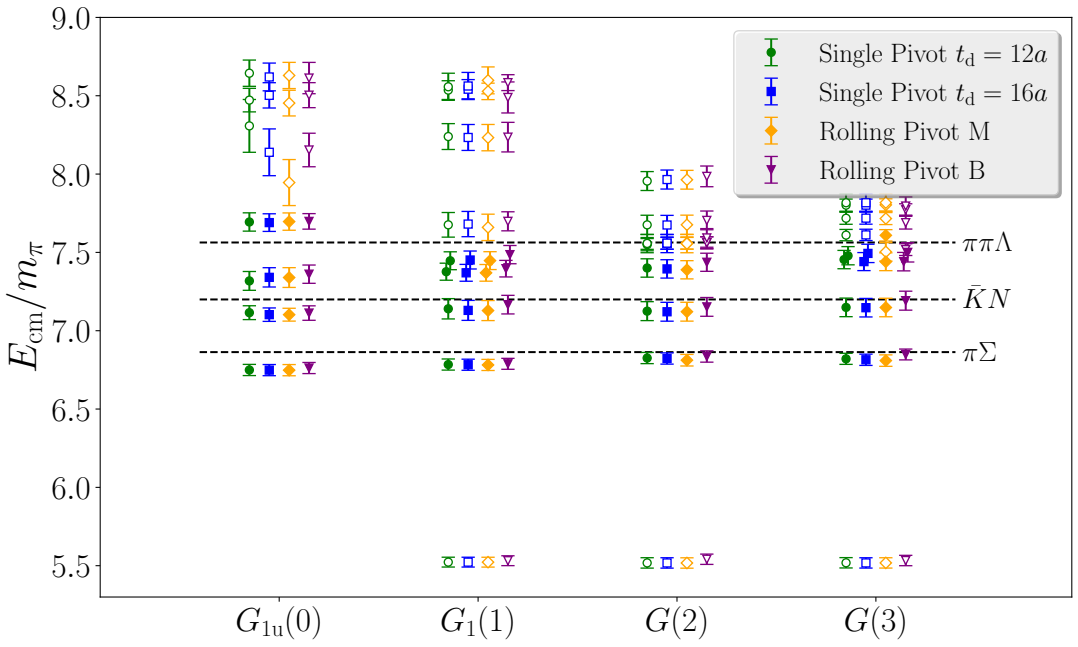

Figure 8.1: Stability of the finite-volume spectra under variation of the correlation matrix rotation method using the GEVP for four different irreps. The metric time is set to $t_0 = 4a$. "Rolling Pivot M" refers to the second approach that uses eigenvectors determined using the mean values of the correlation matrix, and "Rolling Pivot B" is where the GEVP is solved on all of the bootstrap samples as well as the mean of every time slice.

rules of thumb. First, the selected fit must have a p-value greater than 0.1 and/or $\chi^2/\text{dof} < 1.5$. Agreement of the fit result with those from nearby $t_{\rm min}$ values was also considered. When choosing a final fit, I also looked for consistency with the other fit methods. From these considerations, a single-exp ratio fit was selected for all levels, and I required that the final fit is within 2σ of the other ratio fit of the same $t_{\rm min}$. Consistency with the plateau regions of the two-exponential and geometric-exp fits was also required. The final fit is chosen such that it is stable between nearby $t_{\rm min}$ values and maintains consistency between methods. The same fitting strategy to extract the energies from the interacting correlators was used for the single hadron energies, only two-exponential fits were preferred.

An example energy determination of the lowest level of the $G_{1u}(0)$ irrep is shown in Figure 8.2. After comparing the four fit forms described in the figure caption and Section 4.3, the single-exponential ratio fit for $t_{\rm min} = 15a$ is selected as the final estimate. The plots used for the determination of all other levels are given in Appendix B.2.

The final spectra with total isospin $I = 0$ and strangeness $S = -1$ in the center-

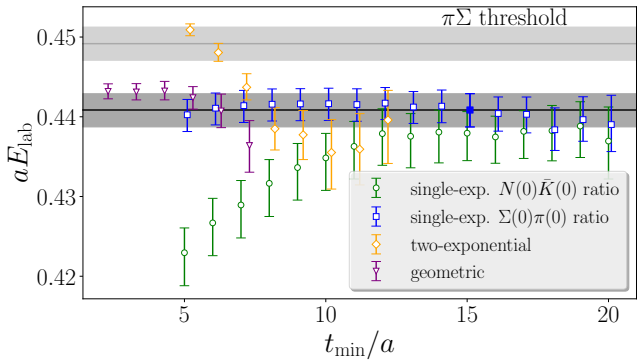

Figure 8.2: Results of different fit models and fit ranges for fits to the rotated correlator associated with the lowest level of the $G_{1u}(0)$ irrep. Each point is the direct result of different fits using temporal range t_{min}, shown on the horizontal axis, to $t_{\text{max}} = 25a$. The fit results compared include two-exponential and geometric-series model fits to the direct rotated correlator, as well as single-exponential fits to the ratio of the rotated correlator over the product of single-hadron correlators where the denominator was either $\bar{K}(0)N(0)$ or $\pi(0)\Sigma(0)$ the zeroes in parentheses referring to $\boldsymbol{d}^2$ of each hadron. The dark horizontal band and filled symbol indicate the final chosen fit selected as described in the text. Error bars in fit-stability plots are determined by binning the samples on either side of the mean to include the nearest 68% of the samples.

of-mass frame for all available symmetry channels are presented in Figure 8.3. The solid lines and gray bands indicate non-interacting two-particle combinations.

8.2 Scattering Amplitudes

8.2.1 Coupled-Channel Fits

Using the finite-volume spectrum, my collaborators computed results for the scattering transition amplitudes using coupled-channel parametrizations. The pole locations for each of the fits in Tables C.1 to C.6 are shown in Figure 8.4a. The transition amplitudes are shown in the upper panel, and the resulting poles from the analytic continuations are shown in the middle panel of Figure 8.4a. Each line in the upper panel is a different fit in Tables C.1 to C.6, with the corresponding pole positions represented as points in the middle panel. The transparency of each fit result is directly related to the value of the AIC[1], darker implying a lower AIC. The variations between the results of the transition amplitudes and the S-matrix poles of the different fits are no longer large.

For $\ell_{\text{max}} = 0$, the finite-volume spectrum shown in Figure 8.3 constrains the coupled-channel scattering amplitude via Equation 5.15 and center-of-mass energies

[1]As described in Section 4.3.

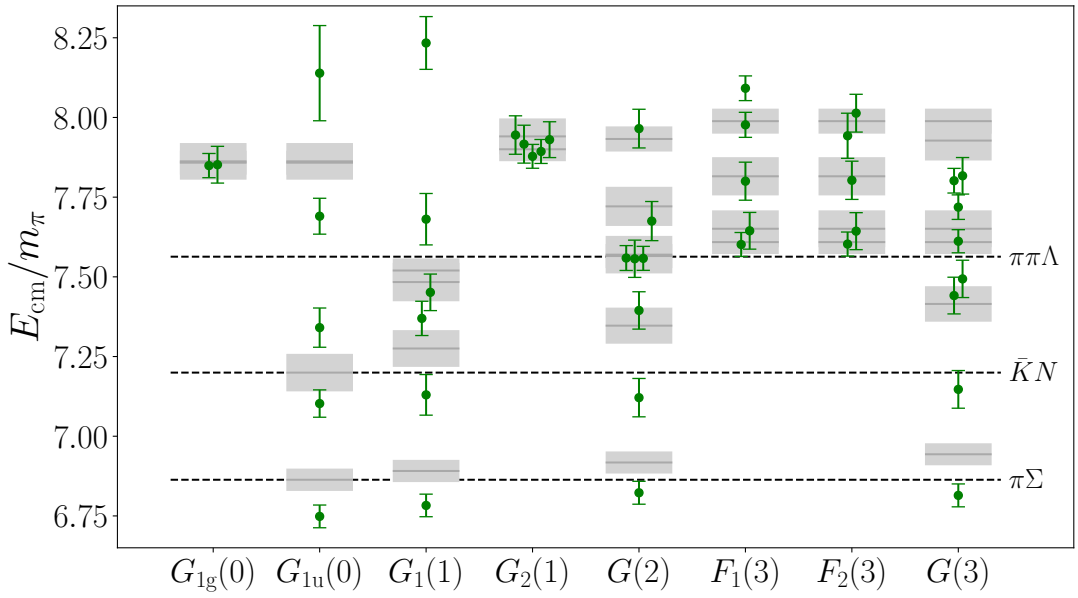

Figure 8.3: Finite-volume stationary-state energy spectrum (circles with error bars) in the center-of-mass frame for total isospin $I = 0$, strangeness $S = -1$, for various irreps indicated along the horizontal axis. The gray bands show the values and variances of energy sums for non-interacting two-particle combinations. Various two- and three-particle thresholds are shown as dashed horizontal lines. Energies are shown in units of the pion mass m_π.

near the $\pi\Sigma$ and $\bar{K}N$ thresholds. All irreps in Table 1 of Reference [78] to which the $J^P = 1/2^-$ partial wave contributes are included.

Six different types of parametrizations of $\widetilde{K}$ with $\ell_{\rm max} = 0$ are tested and presented. In the expressions below, the subscripts i and j denote either of the two scattering channels (channel 0 is $\pi\Sigma$ and channel 1 is $\bar{K}N$). The matrices A, B, $\widehat{A}$, $\widehat{B}$, $\widetilde{A}$, $\widetilde{B}$, $\widehat{C}$, A' and B' below are real and symmetric. The six forms of parametrizations studied are defined as:

1. An effective range expansion (ERE) of the form

$$\widetilde{K}_{ij} = \frac{m_\pi}{E_{\rm cm}}\Big(A_{ij} + B_{ij}\Delta_{\pi\Sigma}(E_{\rm cm})\Big). \tag{8.1}$$

2. A variation of the first parametrization without the factor of $m_\pi/E_{\rm cm}$:

$$\widetilde{K}_{ij} = \widehat{A}_{ij} + \widehat{B}_{ij}\Delta_{\pi\Sigma}(E_{\rm cm}). \tag{8.2}$$

3. An ERE of $\widetilde{K}^{-1}$ of the form

$$\widetilde{K}^{-1}_{ij} = \frac{E_{\rm cm}}{m_\pi}\left(\widetilde{A}_{ij} + \widetilde{B}_{ij}\Delta_{\pi\Sigma}(E_{\rm cm})\right). \tag{8.3}$$

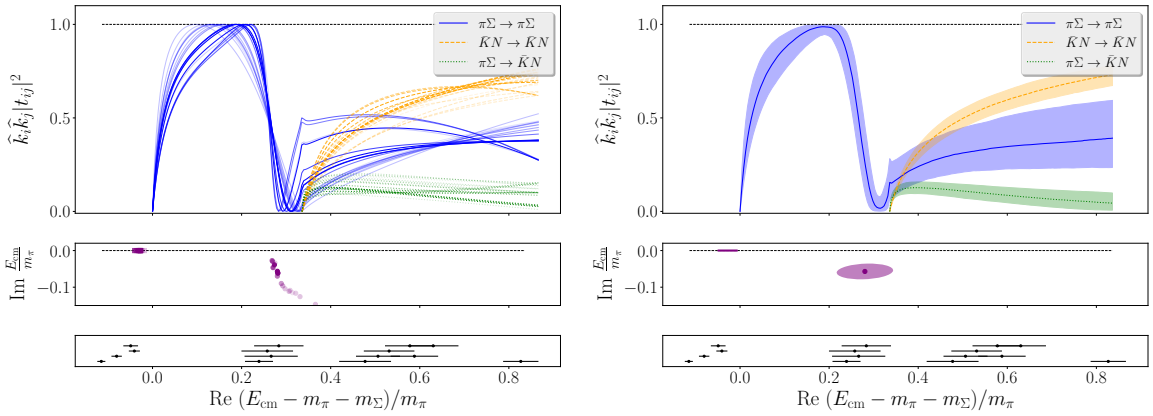

(a) **(b)**

Figure 8.4: The isospin $I = 0$ and strangeness $S = -1$ coupled-channel $\pi\Sigma - \bar{K}N$ transition amplitudes as a function of the center-of-mass energy difference to the $\pi\Sigma$ threshold. The quantities t and $\hat{k}$ are defined in Equation 8.10, and the subscripts i, j indicate the flavor channels. The middle panel in each figure displays the S-matrix poles corresponding to each fit result displayed in the upper panels. The bottom panel in each figure shows the finite-volume spectrum used to constrain the fits involving the transition amplitudes. **(a)** Scattering amplitudes and S-matrix pole locations against center-of-mass energy difference to the $\pi\Sigma$ threshold for various fits. The means of various fit results detailed in Tables C.1 to C.6 are shown in the upper panel. The transparency parameter in matplotlib [87] of each line and corresponding pair of points is set to be $\texttt{alpha} = \exp(-\left(\mathrm{AIC} - \mathrm{AIC}_{\mathrm{min}}\right)/2)$. **(b)** Results are obtained using the best fit specified by Equations 8.12 and 8.1, with uncertainties estimated by bootstrap resampling.

4. A Blatt-Biederharn [88] parametrization:

$$\widetilde{K} = C\ F\ C^{-1}, \tag{8.4}$$

where

$$C = \begin{pmatrix} \cos\epsilon & \sin\epsilon \\ -\sin\epsilon & \cos\epsilon \end{pmatrix}, \tag{8.5}$$

$$F = \begin{pmatrix} f_0(E_{\rm cm}) & 0 \\ 0 & f_1(E_{\rm cm}) \end{pmatrix}, \tag{8.6}$$

and

$$f_i(E_{\rm cm}) = \frac{m_\pi}{E_{\rm cm}} \frac{a_i + b_i \Delta_{\pi\Sigma}(E_{\rm cm})}{1 + c_i \Delta_{\pi\Sigma}(E_{\rm cm})}. \tag{8.7}$$

5. A parametrization based on the leading-order Weinberg-Tomozawa term [89]:

$$\widetilde{K}_{ij} = \frac{\widehat{C}_{ij}}{m_\pi} \left(2E_{\rm cm} - M_i - M_j\right), \tag{8.8}$$

where $M_0 = m_\Sigma$ and $M_1 = m_N$.

6. An expansion that is linear in the energy around the $\pi\Sigma$ threshold:

$$\widetilde{K}_{ij} = A'_{ij} + \frac{B'_{ij}}{m_\pi}\left(E_{\text{cm}} - m_\pi - m_\Sigma\right). \tag{8.9}$$

Using these forms for $\widetilde{K}$, fits are carried out to determine the best-fit values of the above parameters using the spectrum method [60]. The correlated-χ^2 minimized in these fits is defined similar to Equation 14 in Reference [78], except that the residuals are formed in terms of differences between the center-of-mass energy interaction shifts ΔE_{cm} obtained from the quantization condition using the $\widetilde{K}$-matrix parametrization and the interaction shifts determined from the Monte Carlo computations.

Based on the six parametrizations defined above, even more variations were tested by setting various parameters to zero. Tables C.1 to C.6 of Appendix C contain a summary of the results of all fits using the aforementioned parametrizations. In these tables, statistical uncertainties are estimated using the derivative method rather than the resampling method. This method is sufficient for the purposes of illustrating model dependence as well as reduced computational costs. Each fit in these tables also shows the value of the AIC. In Tables C.1-C.6, it can be seen that several of the best-fit results for the $\widetilde{K}$-matrix parameters vary widely, though we see consistency in the physically relevant quantities such as the scattering amplitudes and the S-matrix pole positions.

We define a quantity $t_{ij}^{(J^P)}(E_{\text{cm}})$ that is proportional to the amplitude of the scattering transition and is related to $\widetilde{K}$ by

$$t^{-1} = \widetilde{K}^{-1} - i\widehat{k}, \tag{8.10}$$

where $m_\pi\widehat{k} = \text{diag}\,(k_{\pi\Sigma}, k_{\bar{K}N})$ and k indicates the center-of-mass momentum for the $\pi\Sigma$ particles or for the $\bar{K}N$ particles. The different parameterizations give us information about the energy dependence of the amplitudes near the finite-volume energies. Knowledge over this limited range enables the analytic continuation of $t_{ij}(E_{\text{cm}})$ to complex E_{cm} and the identification of poles close to the real axis on sheets adjacent to the physical one. Analytic continuation of the coupled-channel $\pi\Sigma - \bar{K}N$ scattering amplitude involves four different Riemann sheets ($\text{Im}(k_{\pi\Sigma}) > 0$, $\text{Im}(k_{\pi\Sigma}) < 0$, $\text{Im}(k_{\bar{K}N}) > 0$, $\text{Im}(k_{\bar{K}N}) < 0$), each labelled by the sign of the imaginary parts of $(k_{\pi\Sigma}, k_{\bar{K}N})$, with $(+,+)$ denoting the physical sheet. Complex poles in the scattering amplitudes correspond to vanishing eigenvalues in the right-hand side of Equation 8.10 and are determined numerically. In the vicinity of a pole, the divergent part of the amplitude is

$$t = \frac{m_\pi}{E_{\text{cm}} - E_{\text{pole}}}\begin{pmatrix} c_{\pi\Sigma}^2 & c_{\pi\Sigma}\,c_{\bar{K}N} \\ c_{\pi\Sigma}\,c_{\bar{K}N} & c_{\bar{K}N}^2 \end{pmatrix} + \ldots, \tag{8.11}$$

where the (complex) residues $c_{\pi\Sigma}$, $c_{\bar{K}N}$ represent the coupling of the resonance pole to each channel.

For the fit with the lowest AIC, the errors were more accurately determined using a bootstrap procedure with 800 samples. The fit with the lowest AIC value is a four-parameter fit of the form of Equation 8.1, and the best-fit parameter values are

$$\begin{aligned} A_{00} &= 4.1(1.8), \quad & A_{11} &= -10.5(1.1), \\ A_{01} &= 10.3(1.5), \quad & B_{01} &= -29(18), \end{aligned} \tag{8.12}$$

with fixed $B_{00} = B_{11} = 0$ and $\chi^2 = 10.52$ for 11 degrees of freedom. This fit is shown in Figure 8.4b. The finite-volume energies that are used in this fit are shown in Figure 8.5. The green circles show the center-of-mass energies obtained from the Monte Carlo lattice QCD computations, and the blue squares show the energies obtained from the fit using the LQC and the $\widetilde{K}$-matrix parametrization of Equation 8.1 with best-fit values given in Equation 8.12.

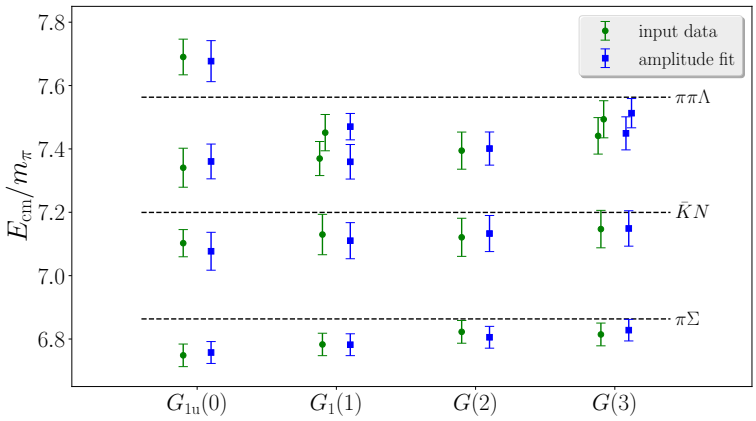

Figure 8.5: finite-volume spectrum in the center-of-mass frame used as input data to constrain parametrizations of the coupled-channel $\pi\Sigma$-$\bar{K}N$ scattering amplitude (green circles). Each column corresponds to a particular irrep $\Lambda(\boldsymbol{d}^2)$ of the little group of total momentum $\boldsymbol{P}^2 = (2\pi/L)^2\boldsymbol{d}^2$. Only irreps where the $\ell = 0$ partial wave contributes are included. Dashed lines indicate various thresholds, as labeled. Model energies from the resultant fit are shown as blue squares.

For this preferred fit, two poles are found on the $(-,+)$ sheet, which is the one closest to physical scattering in the region between the two thresholds, with energies

$$\begin{aligned} E_1/m_\pi &= 6.856(45)_{\rm st}(06)_{\rm md}, \\ E_2/m_\pi &= 7.144(63)_{\rm st}(07)_{\rm md} - i\,0.057(22)_{\rm st}(17)_{\rm md}, \end{aligned}$$

$$\begin{aligned} E_1 &= 1392(9)_{\rm st}(2)_{\rm md}(16)_a \text{ MeV} \\ E_2 &= [1455(13)_{\rm st}(2)_{\rm md}(17)_a \\ &\quad - i \times 11.5(4.4)_{\rm st}(4)_{\rm md}(0.1)_a] \text{ MeV}, \end{aligned} \tag{8.13}$$

while their couplings are

$$\begin{aligned} c^{(1)}_{\pi\Sigma} &= i\,0.52(10)_{\rm st}(2)_{\rm md}, \\ c^{(1)}_{\bar{K}N} &= i\,0.28(8)_{\rm st}(6)_{\rm md}, \\ c^{(2)}_{\pi\Sigma} &= 0.26(9)_{\rm st}(5)_{\rm md} - i\,0.13(3)_{\rm st}(3)_{\rm md}, \\ c^{(2)}_{\bar{K}N} &= 0.12(6)_{\rm st}(4)_{\rm md} - i\,0.53(4)_{\rm st}(2)_{\rm md}. \end{aligned} \tag{8.14}$$

The ratios of these couplings (with correlated uncertainties) show that the lower pole is more strongly coupled to the $\pi\Sigma$ channel, while the pole at a larger real energy is more strongly coupled to the $\bar{K}N$ channel:

$$\begin{aligned} \left| \frac{c^{(1)}_{\pi\Sigma}}{c^{(1)}_{\bar{K}N}} \right| &= 1.9(4)_{\rm st}(6)_{\rm md}, \\ \left| \frac{c^{(2)}_{\pi\Sigma}}{c^{(2)}_{\bar{K}N}} \right| &= 0.53(9)_{\rm st}(10)_{\rm md}. \end{aligned} \tag{8.15}$$

In the above results, the first uncertainty is statistical, the second is derived from model variation, and when the pole positions are quoted in physical units, the third comes from the scale-setting uncertainty in Table 6.1. The systematic uncertainty due to the parametrization dependence is estimated by considering all models that satisfy $\mathrm{AIC} - \mathrm{AIC}_{\rm min} < 1$, and taking half the difference in the maximal spread of values as the model uncertainty.

As shown in Figure 8.4b, the $\widetilde{K}$-matrix parametrizations described in this analyis make no assumptions about the number or locations of the S-matrix poles, and can fit zero, one, or two poles. The best-fit results indicate that E_1 is a virtual bound state (though a few fits produced a bound state), while the one at E_2 is a resonance. The first pole couples more strongly to $\pi\Sigma$, and the second, to $\bar{K}N$.

The scattering amplitude related to the scattering phase shifts δ_i and the inelasticity η through t by

$$\begin{aligned} t_{00} &= \frac{m_\pi(\eta e^{2i\delta_{\pi\Sigma}} - 1)}{2ik_{\pi\Sigma}}, \\ t_{11} &= \frac{m_\pi(\eta e^{2i\delta_{\bar{K}N}} - 1)}{2ik_{\bar{K}N}}, \\ t_{01} &= \frac{m_\pi\sqrt{1-\eta^2}e^{i(\delta_{\pi\Sigma}+\delta_{\bar{K}N})}}{2\sqrt{k_{\pi\Sigma}k_{\bar{K}N}}}, \end{aligned} \tag{8.16}$$

where the indices again indicate the flavor channel: 0 for $\pi\Sigma$ and 1 for $\bar{K}N$. The results are shown in Figure 8.6. The sharp increase in the $\delta_{\pi\Sigma}$ at the $\pi\Sigma$ threshold is indicative of a virtual bound state, and the sharp decrease of $\delta_{\bar{K}N}$ just below the $\bar{K}N$ threshold is indicative of a bound state.

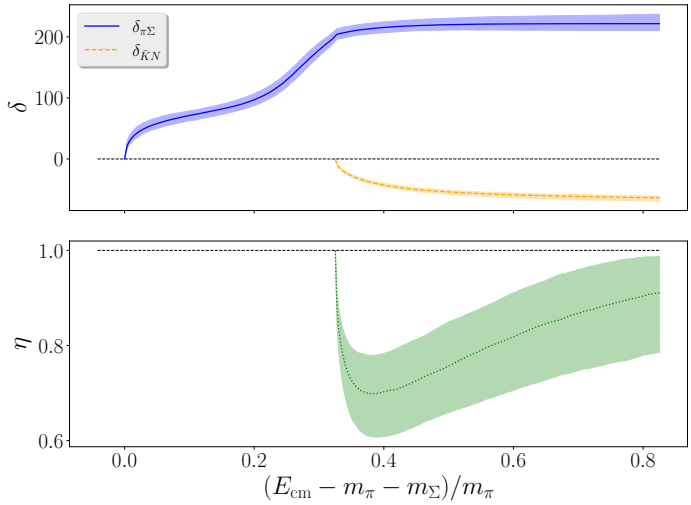

Figure 8.6: Inelasticity η and phase shifts $\delta_{\pi\Sigma}$ and $\delta_{\bar{K}N}$ against center-of-mass energy difference to the $\pi\Sigma$ threshold. These quantities are defined in Equation 8.16. Results are obtained using the best fit specified by Equations 8.12 and 8.1, with uncertainties estimated by resampling.

8.2.2 Single-Channel Fits

Below the $\bar{K}N$ threshold, the standard single-channel Lüscher formalism can be used to calculate the $\pi\Sigma$ scattering amplitude up to effects that are exponentially suppressed with respect to the distance to the $\bar{K}N$ threshold. To verify the existence of the lower pole, the single-channel Lüscher analysis was performed in this regime.

The elastic-scattering phase shift can be parametrized by

$$\frac{k_{\pi\Sigma}}{m_\pi}\cot\delta_{\pi\Sigma} = \frac{E_{\mathrm{cm}}}{m_\pi}(a_{\pi\Sigma} + b_{\pi\Sigma}\Delta_{\pi\Sigma}), \tag{8.17}$$

where $a_{\pi\Sigma}$ and $b_{\pi\Sigma}$ are fit parameters where the quantity

$$\Delta_{\pi\Sigma}(E_{\mathrm{cm}}) = \frac{E_{\mathrm{cm}}^2 - (m_\pi + m_\Sigma)^2}{(m_\pi + m_\Sigma)^2}, \tag{8.18}$$

is related to the center-of-mass energy gap above $\pi\Sigma$ threshold.

The s-wave fit with $\ell_{\max} = 0$, is equivalent to the fit performed to the πN $I = 1/2$ spectrum. In this case, the only available irreps are $G_{1\mathrm{u}}(0), G_1(1)$, $G(2)$ and $G(3)$ irreps, but there is sufficient effect in the spectra of nonzero momentum frames to use the next-to-leading-order ERE. The fit performed using these levels is shown in Figure 8.5 using the parametrization in Equation 8.17. The results are

$$a_{\pi\Sigma} = 0.047(14), \quad b_{\pi\Sigma} = 0.65(50), \quad \chi^2 = 5.04, \tag{8.19}$$

with two degrees of freedom and is shown in Figure 8.7, along with a comparison to the elastic phase shift from the multi-channel analysis in Equation 8.12. One observes

that the phase-shift curve (blue band) intersects the virtual-bound-state condition (black dashed line). That is,

$$k_{\pi\Sigma} \cot \delta_{\pi\Sigma} - i k_{\pi\Sigma} = 0, \tag{8.20}$$

for purely imaginary and negative $k_{\pi\Sigma}$. The position of the virtual bound state is found at

$$\begin{aligned} E_1/m_\pi &= 6.822(37), \\ E_1 &= 1389(8)_{\text{st}}(16)_a \text{ MeV}. \end{aligned} \tag{8.21}$$

Thus, the results are consistent with those obtained in the multi-channel analysis.

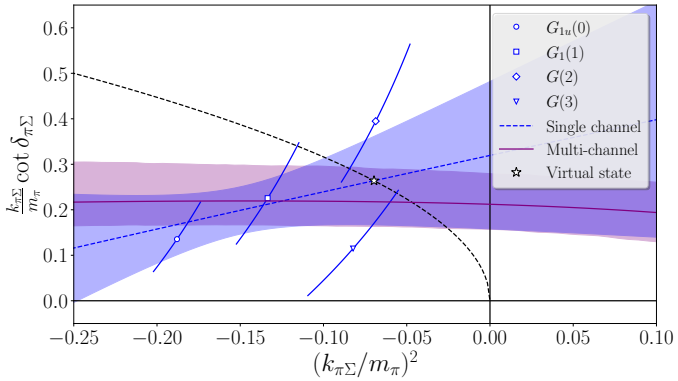

Figure 8.7: The $\pi\Sigma$ elastic phase shift as a function of the center-of-mass momentum squared, determined in a single-channel analysis and compared against the multi-channel result. The dashed black line corresponds to the virtual bound state condition in Equation 8.20. The blue dashed line and corresponding band show the fit to an ERE with statistical errors. The star highlights the position of the virtual-bound-state in the single-channel analysis. The solid purple line and the associated band show the result from the multi-channel fit with lowest AIC value. The scattering phase shifts from each energy level are shown by the hollow blue symbols.

Chapter 9

Conclusions

In summary, my collaborators and I were successful in calculating high-precision scattering observables using lattice QCD to precisely determine resonance properties of the $\Delta(1232)$ and the $\Lambda(1405)$ resonances. These scattering observables demonstrate that the stochastic LapH methods are successful in reducing computation time while maintaining high-precision results. Throughout the analyses, our methodologies improved and new ones are in development.

This work presents a computation of the lowest partial waves for the elastic nucleon-pion scattering amplitude. The s-wave scattering lengths are determined for isospins $I = 1/2$ and $I = 3/2$. The results reviewed in this thesis were the first unquenched lattice QCD determinations of both nucleon-pion scattering lengths for $m_\pi < 250$ MeV. The Breit-Wigner resonance parameters of the $\Delta(1232)$ in the $J^P = 3/2^+$ partial wave with $I = 3/2$ are also determined. The main results of the πN study are in Figures 7.3-7.5 and Tables 7.2-7.3 using Equations 7.1-7.4.

Using the finite-volume spectrum of the πN of $I = 3/2$ channel, two tests were developed to detect potential missing levels from the spectrum due to insufficient operators. Both of these tests were successful when using the toy correlators, but as soon as noise was introduced, both tests led to false positives. Further analysis is required to determine the probability of success based on the magnitude of fluctuations. If modifications to these tests overcome the noise problem, the other mitigating factor, contamination from higher-lying energies, should also be investigated and addressed.

Similar to the $\Delta(1232)$ analysis, hermitian correlation matrices using single baryon and meson-baryon interpolating operators for a variety of different total momenta and irreducible representations were used to determine the finite volume stationary-state energies in the isospin $I = 0$, strangeness $S = -1$ sector with lattice QCD and the stochastic LapH method. Various K-matrix parameterizations restricted to s-waves were then used in the quantization condition to fit the finite-volume spectrum obtained from lattice QCD. The resulting best-fit parameter values from the K-matrix parametrization yielding the lowest AIC produced the $\pi\Sigma$-$\bar{K}N$ transition amplitudes shown in Fig. 8.4b. The best scattering-amplitudes fit as well as all other successful

fits revealed two poles, a virtual bound state below the $\pi\Sigma$ threshold and a resonance just below the higher $\bar{K}N$ threshold. A single-channel fit of $\pi\Sigma$ scattering support the coupled-channel findings of the lower pole. Higher-wave contributions were examined and found to be negligible at the current statistical precision. The main results of our $\Lambda(1405)$ study are in Figures 8.4b and 8.6 using Equation 8.13.

The scattering results reviewed in this thesis are not computed at the physical pion mass and are only computed on one lattice size. In order to produce usable data for future experiments, these calculations will need to be repeated on multiple lattice sizes and for multiple pion masses to determine the true continuum scattering results. In the meantime, the results can still give us meaningful insight into QCD physics.

With recent developments of the three-particle Lüscher formalism, new resonances and new physics can be explored above the three-particle threshold. For three-particle scattering, there can easily be upward of a hundred levels in the finite-volume spectrum, requiring magnitudes more correlators to extract them. With the stochastic LapH method, the computation time to calculate these is feasible, and the resulting analysis can hopefully gain further confidence and efficiency with the continued development of the new analysis processes discussed in this work.

The processes used in this thesis will also be applied to three-point functions to facilitate matrix-element evaluations of important currents, as well as various physical transition amplitudes important for near-future experiments such as DUNE.

Appendix A

$\Delta(1232)$ and $\Lambda(1405)$ Operator Selection

All operators used in this study are single-site operators. The notation for the irreps follows the conventions in Reference [32]. The subscripts g/u indicate even/odd parity, and the superscripts $+/-$ indicate even/odd G-parity. Whenever there is more than one independent Clebsch-Gordan combination, the multiplicity is indicated by an integer to the right of the operator identification. The Clebsch-Gordan coefficients that fully define each operator are not given, but are available upon request.

The single- and two-hadron operators used for the $\Delta(1232)$ study are specified in Tables A.1-A.2 in this section. The single- and two-hadron operators used for the $\Lambda(1405)$ study are specified in Tables A.3-A.4. We utilize multi-hadron operators made up of individual constituent hadrons, each corresponding to a definite momentum. Each single-hadron operator is specified by its flavor structure, such as Λ, Σ, N, π, $\bar{K}$, then in square brackets, the irrep of its little group, with the squared spatial momentum, in units of $(2\pi/L)^2$, shown in parentheses. The subscript indicates an identification number for the multiple variations of the single-site configuration. The spin and orbital structure associated with each identification number can be obtained from the author upon request.

$\Lambda(\boldsymbol{d}^2)$	Operators
$G_{1u}(0)$	$\pi[A_{1u}^-(0)]_0\ N[G_{1g}(0)]_0$
	$\pi[A_2^-(1)]_1\ N[G_1(1)]_0$
$G_1(1)$	$N[G_1(1)]_0$
	$\pi[A_{1u}^-(0)]_0\ N[G_1(1)]_0$
	$\pi[A_2^-(1)]_1\ N[G_{1g}(0)]_0$
$G(2)$	$N[G(2)]_0$
	$\pi[A_{1u}^-(0)]_0\ N[G(2)]_0$
	$\pi[A_2^-(1)]_1\ N[G_1(1)]_0\ (2)$
$G(3)$	$N[G(3)]_0$
	$\pi[A_{1u}^-(0)]_0\ N[G(3)]_0$
	$\pi[A_2^-(1)]_1\ N[G(2)]_0\ (2)$
$G_1(4)$	$N[G_1(4)]_0$
	$\pi[A_{1u}^-(0)]_0\ N[G_1(4)]_0$
	$\pi[A_2^-(1)]_1\ N[G_1(1)]_0$

Table A.1: Single- and two-hadron operators used in each symmetry sector of the $I = 1/2$ channel of the $\Delta(1232)$ analysis. Operator notation is described in the text.

$\Lambda(\boldsymbol{d}^2)$	Operators
$G_{1u}(0)$	$\pi[A_{1u}^-(0)]_0\ N[G_{1g}(0)]_0$
	$\pi[A_2^-(1)]_1\ N[G_1(1)]_0$
$H_g(0)$	$\Delta[H_g(0)]_0$
	$\pi[A_2^-(1)]_1\ N[G_1(1)]_0$
	$\pi[A_2^-(2)]_0\ N[G(2)]_0\ (2)$
$G_1(1)$	$\Delta[G_1(1)]_0$
	$\pi[A_{1u}^-(0)]_0\ N[G_1(1)]_0$
	$\pi[A_2^-(1)]_1\ N[G_{1g}(0)]_0$
	$\pi[A_2^-(1)]_1\ N[G(2)]_0\ (2)$
	$\pi[A_2^-(2)]_0\ N[G_1(1)]_0\ (2)$
$G_2(1)$	$\Delta[G_2(1)]_0$
	$\pi[A_2^-(1)]_1\ N[G(2)]_0\ (2)$
	$\pi[A_2^-(2)]_0\ N[G_1(1)]_0\ (2)$
$G(2)$	$\Delta[G(2)]_0$
	$\Delta[G(2)]_1$
	$\pi[A_{1u}^-(0)]_0\ N[G(2)]_0$
	$\pi[A_2^-(1)]_1\ N[G_1(1)]_0\ (2)$
	$\pi[A_2^-(1)]_1\ N[G(3)]_0\ (2)$
	$\pi[A_2^-(2)]_0\ N[G_{1g}(0)]_0$

(a) $\boldsymbol{d}^2 = 0, 1, 2$

$\Lambda(\boldsymbol{d}^2)$	Operators
$F_1(3)$	$\Delta[F_1(3)]_0$
	$\pi[A_2^-(1)]_1\ N[G(2)]_0$
	$\pi[A_2^-(2)]_0\ N[G_1(1)]_0$
$F_2(3)$	$\Delta[F_2(3)]_0$
	$\pi[A_2^-(1)]_1\ N[G(2)]_0$
	$\pi[A_2^-(2)]_0\ N[G_1(1)]_0$
$G(3)$	$N[G(3)]_0$
	$\pi[A_{1u}^-(0)]_0\ N[G(3)]_0$
	$\pi[A_2^-(1)]_1\ N[G(2)]_0\ (2)$
	$\pi[A_2^-(2)]_0\ N[G_1(1)]_0\ (2)$
	$\pi[A_2^-(3)]_0\ N[G_{1g}(0)]_0$
$G_1(4)$	$\Delta[G_1(4)]_0$
	$\pi[A_{1u}^-(0)]_0\ N[G_1(4)]_0$
	$\pi[A_2^-(1)]_1\ N[G_1(1)]_0$
	$\pi[A_2^-(2)]_0\ N[G(2)]_0\ (2)$
$G_2(4)$	$\Delta[G_2(4)]_0$
	$\pi[A_2^-(2)]_0\ N[G(2)]_0\ (2)$

(b) $\boldsymbol{d}^2 = 3, 4$

Table A.2: Single- and two-hadron operators used in each symmetry sector of the $I = 3/2$ channel of the $\Delta(1232)$ analysis. Operator notation is described in the text.

$\Lambda(\boldsymbol{d}^2)$	Operators
$H_{\mathrm{u}}(0)$	$\pi[A_{1u}^{-}(0)]_0\ \Sigma[Hg(0)]_0$
	$\pi[A_2^{-}(1)]_1\ \Sigma[G_1(1)]_0$
	$\bar{K}[A_2(1)]_1\ N[G_1(1)]_0$
$G_{1\mathrm{g}}(0)$	$\Lambda[G_{1g}(0)]_0$
	$\Lambda[G_{1g}(0)]_1$
	$\Lambda[G_{1g}(0)]_3$
	$\bar{K}[A_2(1)]_1\ N[G_1(1)]_0$
	$\pi[A_2^{-}(1)]_1\ \Sigma[G_1(1)]_0$
$G_{1\mathrm{u}}(0)$	$\Lambda[G_{1u}(0)]_0$
	$\Lambda[G_{1u}(0)]_1$
	$\Lambda[G_{1u}(0)]_2$
	$\Lambda[G_{1u}(0)]_3$
	$\bar{K}[A_{1u}(0)]_0\ N[G_{1g}(0)]_0$
	$\pi[A_{1u}^{-}(0)]_0\ \Sigma[G_{1g}(0)]_0$
	$\bar{K}[A_2(1)]_1\ N[G_1(1)]_0$
	$\pi[A_2^{-}(1)]_1\ \Sigma[G_1(1)]_0$

(a) $\boldsymbol{d}^2 = 0$

$\Lambda(\boldsymbol{d}^2)$	Operators
$G_1(1)$	$\Lambda[G_1(1)]_0$
	$\Lambda[G_1(1)]_1$
	$\Lambda[G_1(1)]_2$
	$\Lambda[G_1(1)]_4$
	$\Lambda[G_1(1)]_6$
	$\bar{K}[A_{1u}(0)]_0\ N[G_1(1)]_0$
	$\pi[A_{1u}^{-}(0)]_0\ \Sigma[G_1(1)]_0$
	$\bar{K}[A_2(1)]_1\ N[G_1g(0)]_0$
	$\pi[A_2^{-}(1)]_1\ \Sigma[G_1g(0)]_0$
$G_2(1)$	$\Lambda[G_2(1)]_0$
	$\Lambda[G_2(1)]_1$
	$\pi[A_{1u}^{-}(0)]_0\ \Sigma[G_2(1)]_0$
	$\pi[A_2^{-}(1)]_1\ \Sigma[G(2)]_0 \quad (2)$
	$\bar{K}[A_2(1)]_1\ N[G(2)]_0 \quad (2)$

(b) $\boldsymbol{d}^2 = 1$

Table A.3: Single- and two-hadron operators used in the $\Lambda(1405)$ analysis in each symmetry sector with total momentums $\boldsymbol{d}^2 = 0$ and $\boldsymbol{d}^2 = 1$. Operator notation is described in the text.

$\Lambda(\boldsymbol{d}^2)$	Operators
$G(2)$	$\Lambda[G(2)]_0$
	$\Lambda[G(2)]_1$
	$\Lambda[G(2)]_2$
	$\Lambda[G(2)]_3$
	$\Lambda[G(2)]_5$
	$\Lambda[G(2)]_6$
	$\bar{K}[A_{1u}(0)]_0\ N[G(2)]_0$
	$\pi[A^-_{1u}(0)]_0\ \Sigma[G(2)]_0$
	$\bar{K}[A_2(1)]_1\ N[G_1(1)]_0$ (2)
	$\pi[A^-_2(1)]_1\ \Sigma[G_1(1)]_0$ (2)
	$\bar{K}[A_2(2)]_0\ N[G_{1g}(0)]_0$
	$\pi[A^-_{1u}(0)]_0\ \Sigma[G(2)]_1$
	$\pi[A^-_{1u}(0)]_0\ \Sigma[G(2)]_7$

(a) $\boldsymbol{d}^2 = 2$

$\Lambda(\boldsymbol{d}^2)$	Operators
$F_1(3)$	$\Lambda[F_1(3)]_0$
	$\pi[A^-_2(1)]_1\ \Sigma[G(2)]_0$
	$\bar{K}[A_2(1)]_1\ N[G(2)]_0$
	$\pi[A^-_2(2)]_0\ \Sigma[G_1(1)]_0$
	$\bar{K}[A_2(2)]_0\ N[G_1(1)]_0$
	$\pi[A^-_{1u}(0)]_0\ \Sigma[F_2(3)]_0$
$F_2(3)$	$\Lambda[F_2(3)]_0$
	$\pi[A^-_2(1)]_1\ \Sigma[G(2)]_0$
	$\bar{K}[A_2(1)]_1\ N[G(2)]_0$
	$\pi[A^-_2(2)]_0\ \Sigma[G_1(1)]_0$
	$\bar{K}[A_2(2)]_0\ N[G_1(1)]_0$
	$\pi[A^-_{1u}(0)]_0\ \Sigma[F_1(3)]_0$
$G(3)$	$\Lambda[G(3)]_0$
	$\Lambda[G(3)]_1$
	$\Lambda[G(3)]_4$
	$\Lambda[G(3)]_5$
	$\bar{K}[A_{1u}(0)]_0\ N[G(3)]_0$
	$\pi[A^-_{1u}(0)]_0\ \Sigma[G(3)]_0$
	$\bar{K}[A_2(1)]_1\ N[G(2)]_0$ (2)
	$\pi[A^-_2(1)]_1\ \Sigma[G(2)]_0$ (2)
	$\bar{K}[A_2(2)]_0\ N[G_1(1)]_0$ (2)
	$\bar{K}[A_2(2)]_0\ N[G_{1g}(0)]_0$

(b) $\boldsymbol{d}^2 = 3$

Table A.4: Same as Table A.3 with $\boldsymbol{d}^2 = 2$ and $\boldsymbol{d}^2 = 3$.

Appendix B

Fit-Stability Analysis for Finite-Volume Spectrum

B.1 $\Delta(1232)$

As discussed in Sec. 7, multiple fit ranges and fit forms are compared for every energy level to ensure systematic errors associated with excited-state contamination are smaller than the statistical errors. Ultimately, single-exponential fits to the correlator ratios are chosen because of their mild sensitivity to t_{min} and good statistical precision. The fit range is chosen to be consistent with the double-exponential t_{min} plateau, defined as the range of t_{min} for which the fitted energy does not exhibit statistically significant variation. Most levels are also consistent with the single-exponential fit plateau, although as shown in Figure 6.2 for m_{N}, these fits may not describe the correlators that have significant excited-state contamination. Figure B.1 contains t_{min}-plots for each of the $I = 1/2$ levels and the $I = 3/2$ levels in Figures B.2-B.6.

B.2 $\Lambda(1405)$

The energy determinations are shown in Figures B.7 in this section. The results of four different fit methods are shown: two-exponential and geometric series fits to the rotated correlator, and single-exponential fits to the ratio of the rotated diagonal correlator over the product of single-hadron correlators for either $\bar{K}(\boldsymbol{d}^2_{\bar{K}})N(\boldsymbol{d}^2_N)$ or $\pi(\boldsymbol{d}^2_\pi)\Sigma(\boldsymbol{d}^2_\Sigma)$. The dark horizontal band and the filled symbol denote the final chosen fit for each level selected as described in Section 8.1. Bootstrap samples for extracted energies are available in Reference [90].

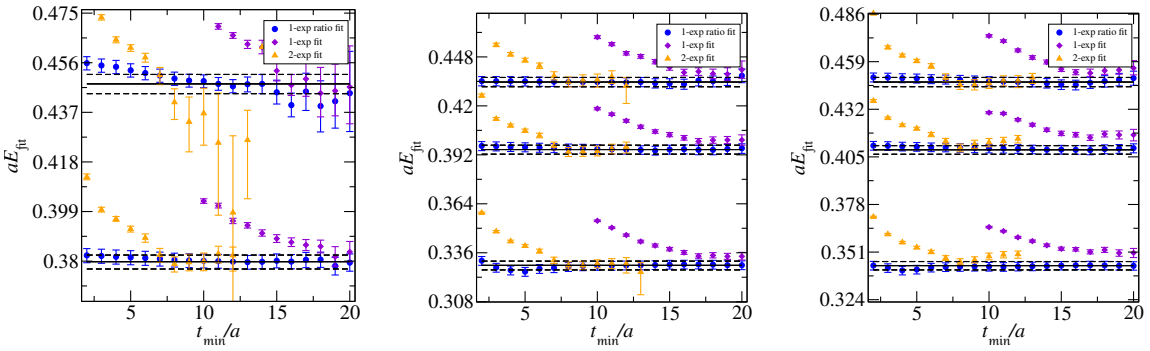

(a) $G_{1u}(0)$ **(b)** $G_1(1)$ **(c)** $G(2)$

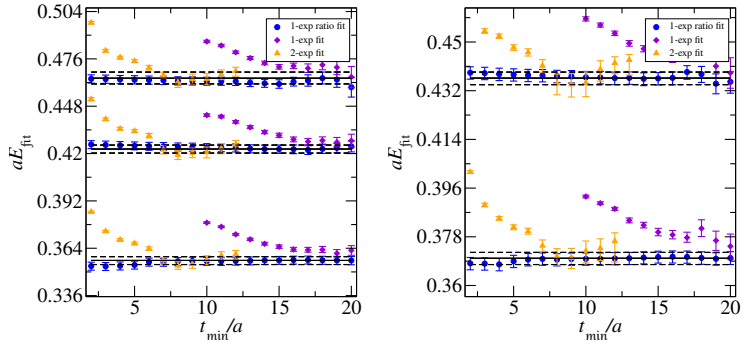

(d) $G(3)$ **(e)** $G_1(4)$

Figure B.1: Stability of the $I = 1/2$ spectrum illustrated by varying the fit range and fit form. The chosen fit for each level is indicated by the solid black line and the corresponding errors are indicated by dotted lines. Each subplot contains the spectrum for a single irrep labeled in the same manner as Figure 7.2. The chosen values are taken from ratio fits and compared to both single- and double-exponential fits over a range of $t_{\rm min}$ with $t_{\rm max} = 25a$.

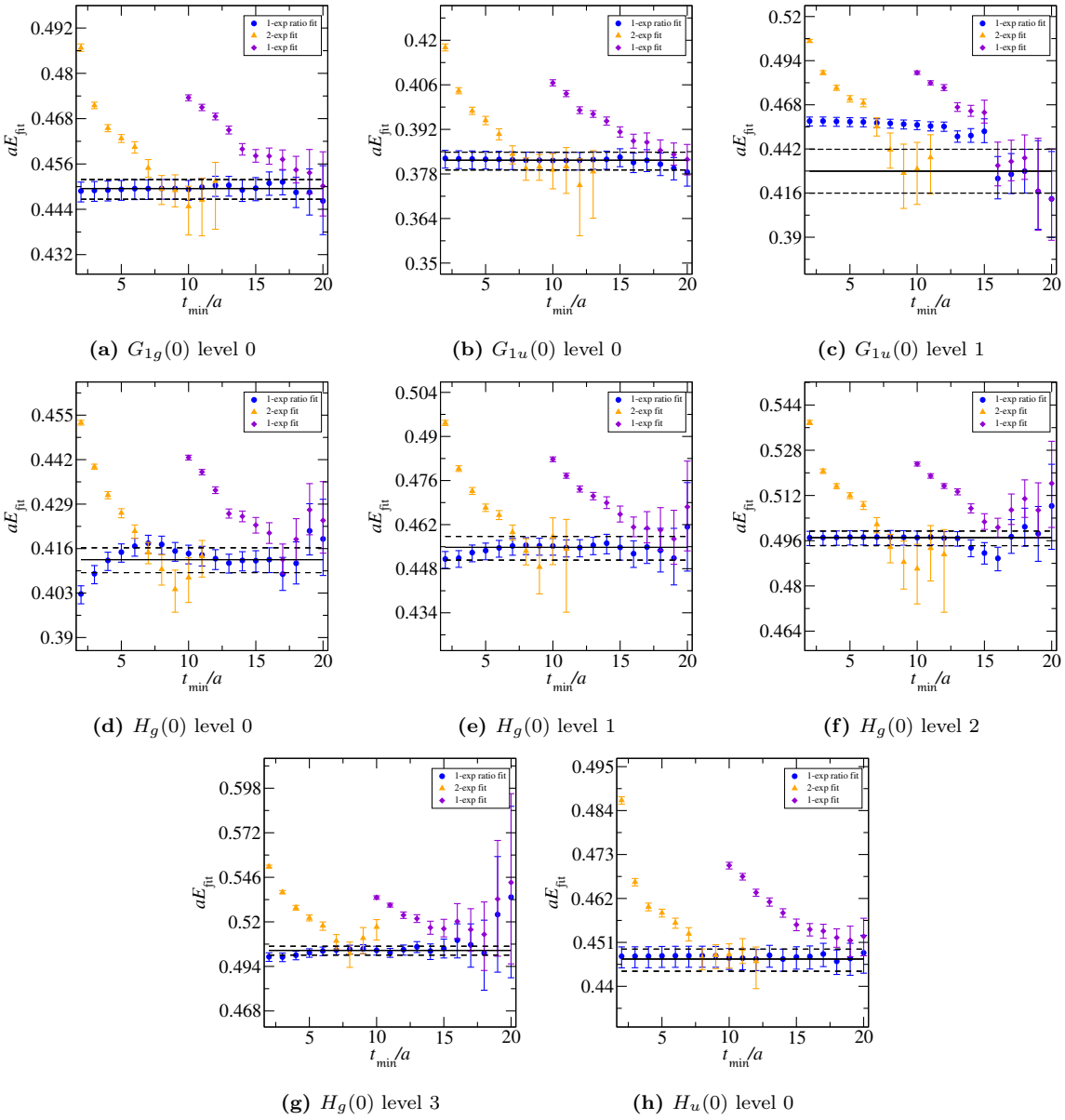

(a) $G_{1g}(0)$ level 0 **(b)** $G_{1u}(0)$ level 0 **(c)** $G_{1u}(0)$ level 1

(d) $H_g(0)$ level 0 **(e)** $H_g(0)$ level 1 **(f)** $H_g(0)$ level 2

(g) $H_g(0)$ level 3 **(h)** $H_u(0)$ level 0

Figure B.2: Stability of fits to determine the $I = 3/2$ spectrum for total momentum having $\boldsymbol{d}^2 = 0$. As in Figure B.1, a variety of fit ranges and fit forms is compared for each level. Each plot contains all fits for a single level in a particular irrep. Indexing for the levels begins at zero for the lowest and increases with increasing energy.

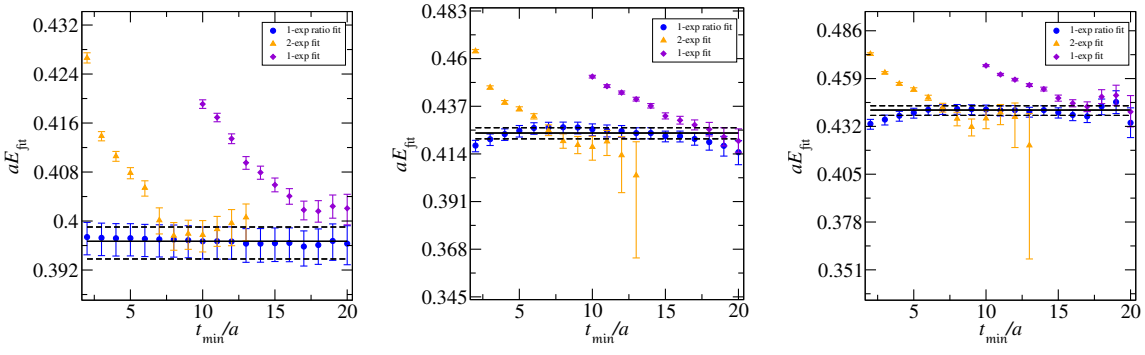

(a) $G_1(1)$ level 0 **(b)** $G_1(1)$ level 1 **(c)** $G_1(1)$ level 2

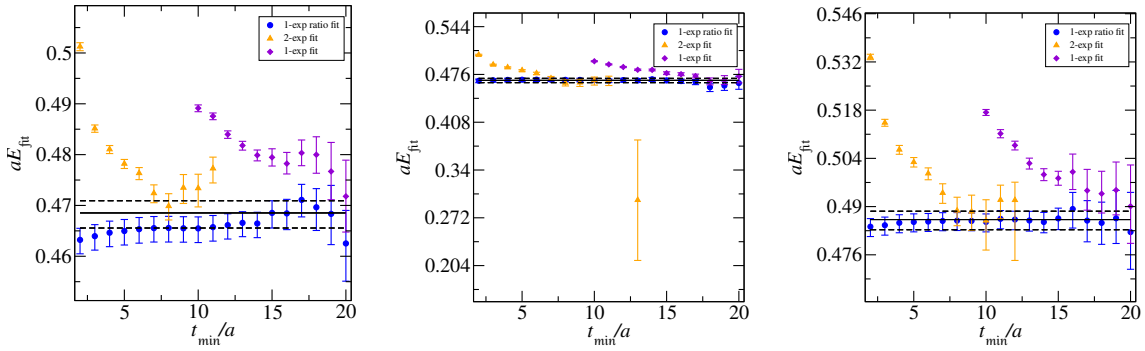

(d) $G_1(1)$ level 3 **(e)** $G_1(1)$ level 4 **(f)** $G_1(1)$ level 5

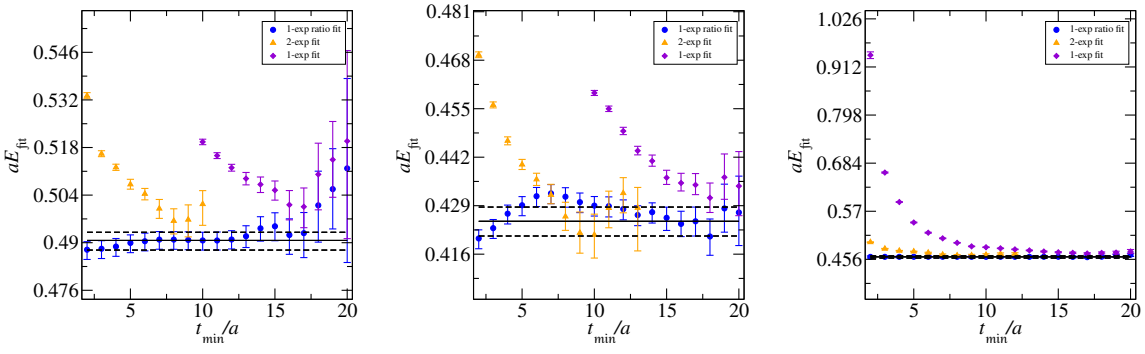

(g) $G_1(1)$ level 6 **(h)** $G_2(1)$ level 0 **(i)** $G_2(1)$ level 1

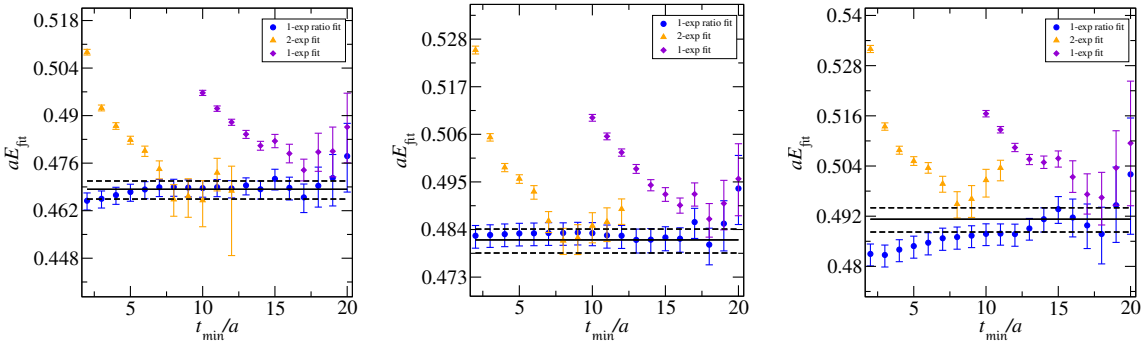

(j) $G_2(1)$ level 2 **(k)** $G_2(1)$ level 3 **(l)** $G_2(1)$ level 4

Figure B.3: Same as Figure B.2 for $I = 3/2$ except that $\boldsymbol{d}^2 = 1$.

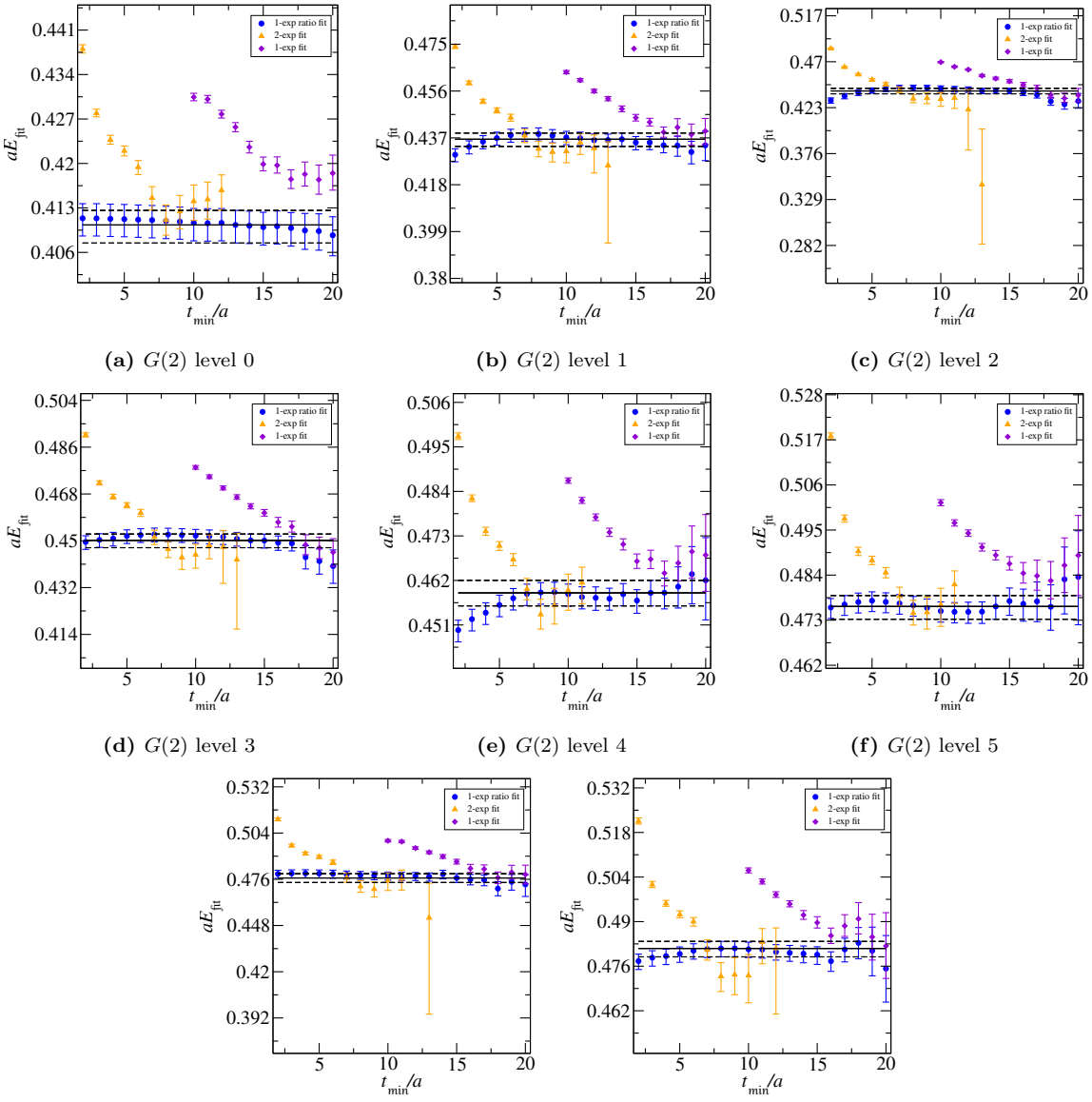

(a) $G(2)$ level 0 **(b)** $G(2)$ level 1 **(c)** $G(2)$ level 2

(d) $G(2)$ level 3 **(e)** $G(2)$ level 4 **(f)** $G(2)$ level 5

(g) $G(2)$ level 6 **(h)** $G(2)$ level 7

Figure B.4: Same as Figure B.2 for $I = 3/2$ except that $\boldsymbol{d}^2 = 2$.

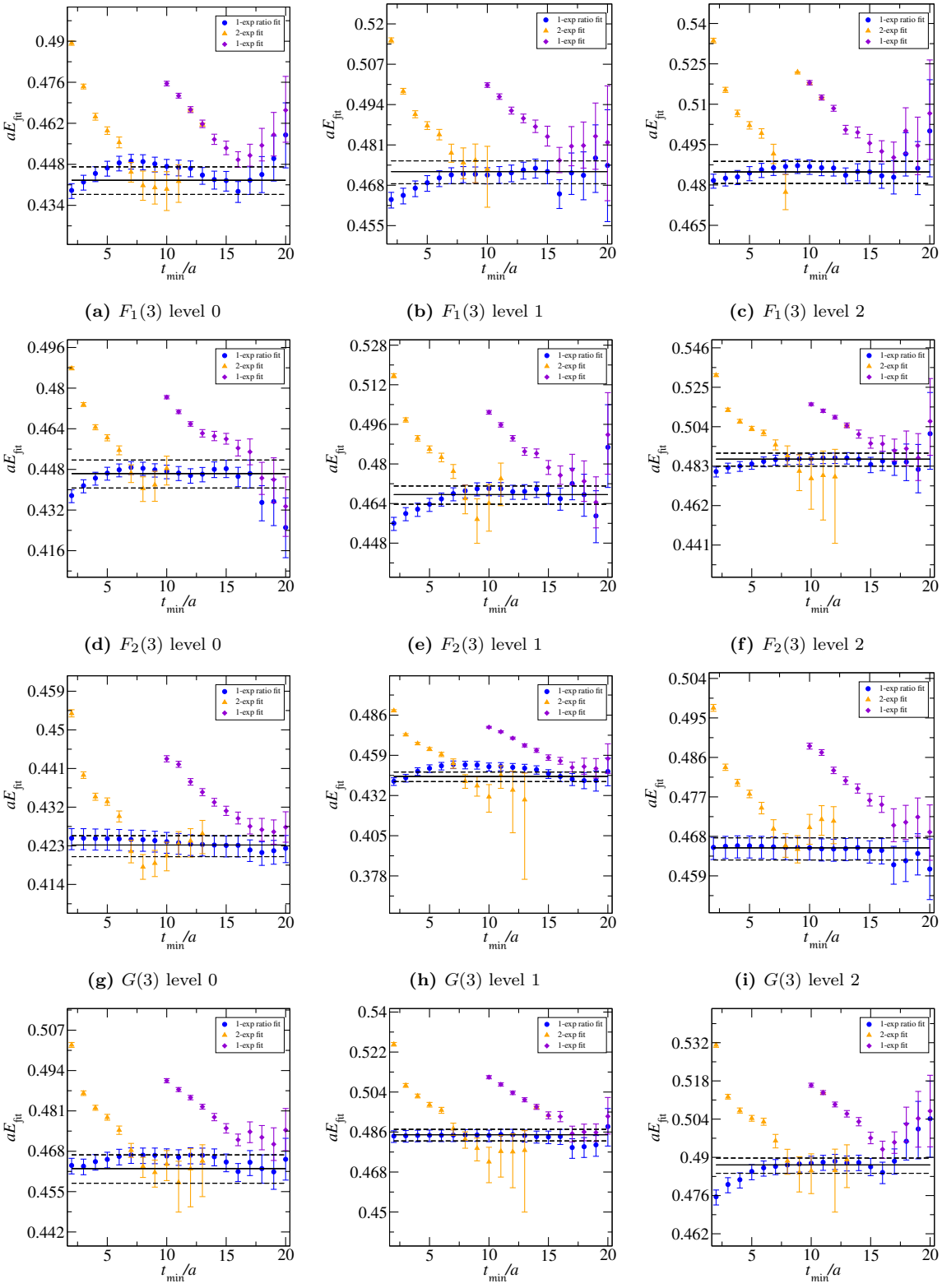

(a) $F_1(3)$ level 0 **(b)** $F_1(3)$ level 1 **(c)** $F_1(3)$ level 2

(d) $F_2(3)$ level 0 **(e)** $F_2(3)$ level 1 **(f)** $F_2(3)$ level 2

(g) $G(3)$ level 0 **(h)** $G(3)$ level 1 **(i)** $G(3)$ level 2

(j) $G(3)$ level 3 **(k)** $G(3)$ level 4 **(l)** $G(3)$ level 5

Figure B.5: Same as Figure B.2 for $I = 3/2$ except that $\boldsymbol{d}^2 = 3$.

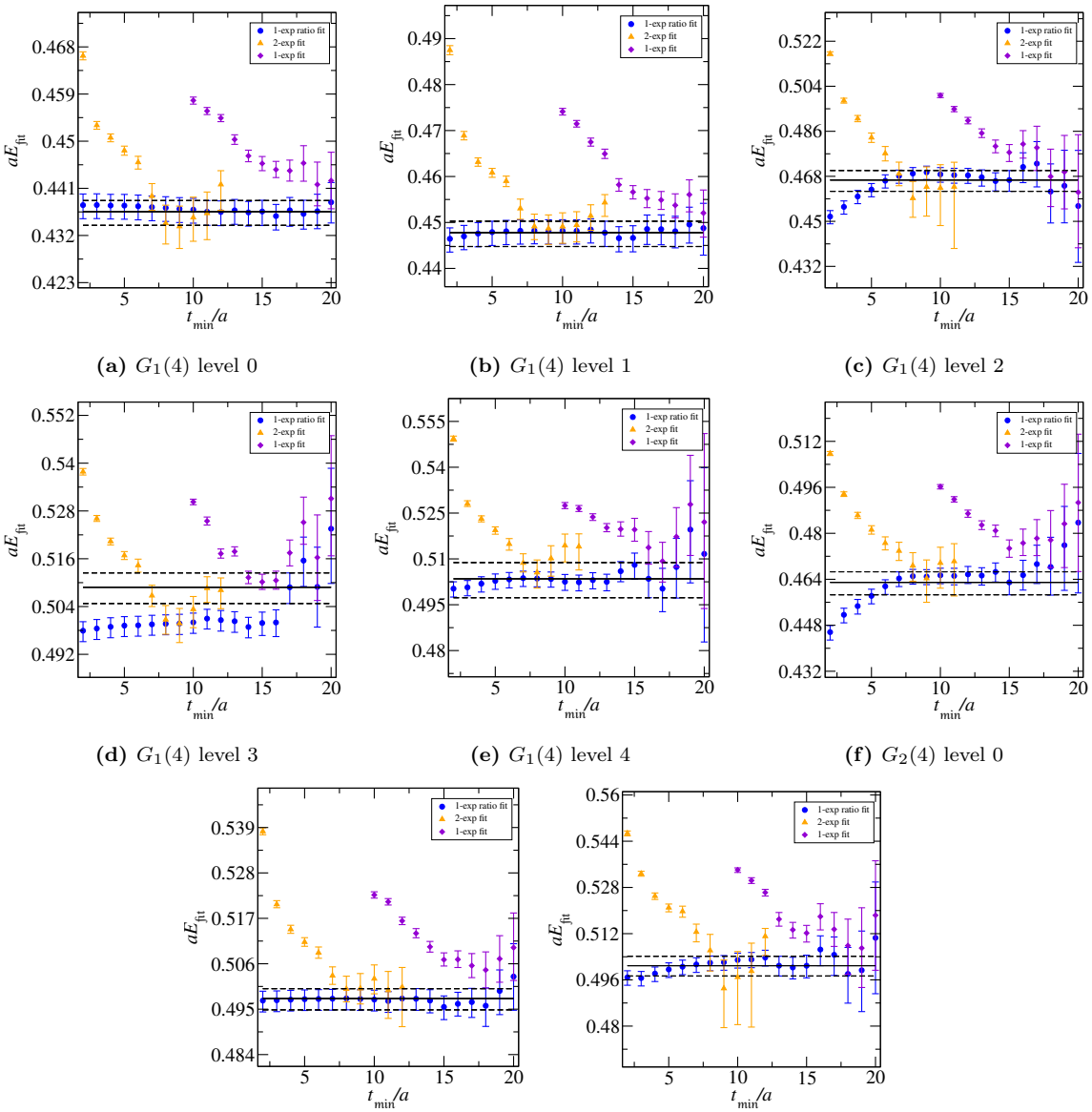

(a) $G_1(4)$ level 0 **(b)** $G_1(4)$ level 1 **(c)** $G_1(4)$ level 2

(d) $G_1(4)$ level 3 **(e)** $G_1(4)$ level 4 **(f)** $G_2(4)$ level 0

(g) $G_2(4)$ level 1 **(h)** $G_2(4)$ level 2

Figure B.6: Same as Figure B.2 for $I = 3/2$ except that $\boldsymbol{d}^2 = 4$.

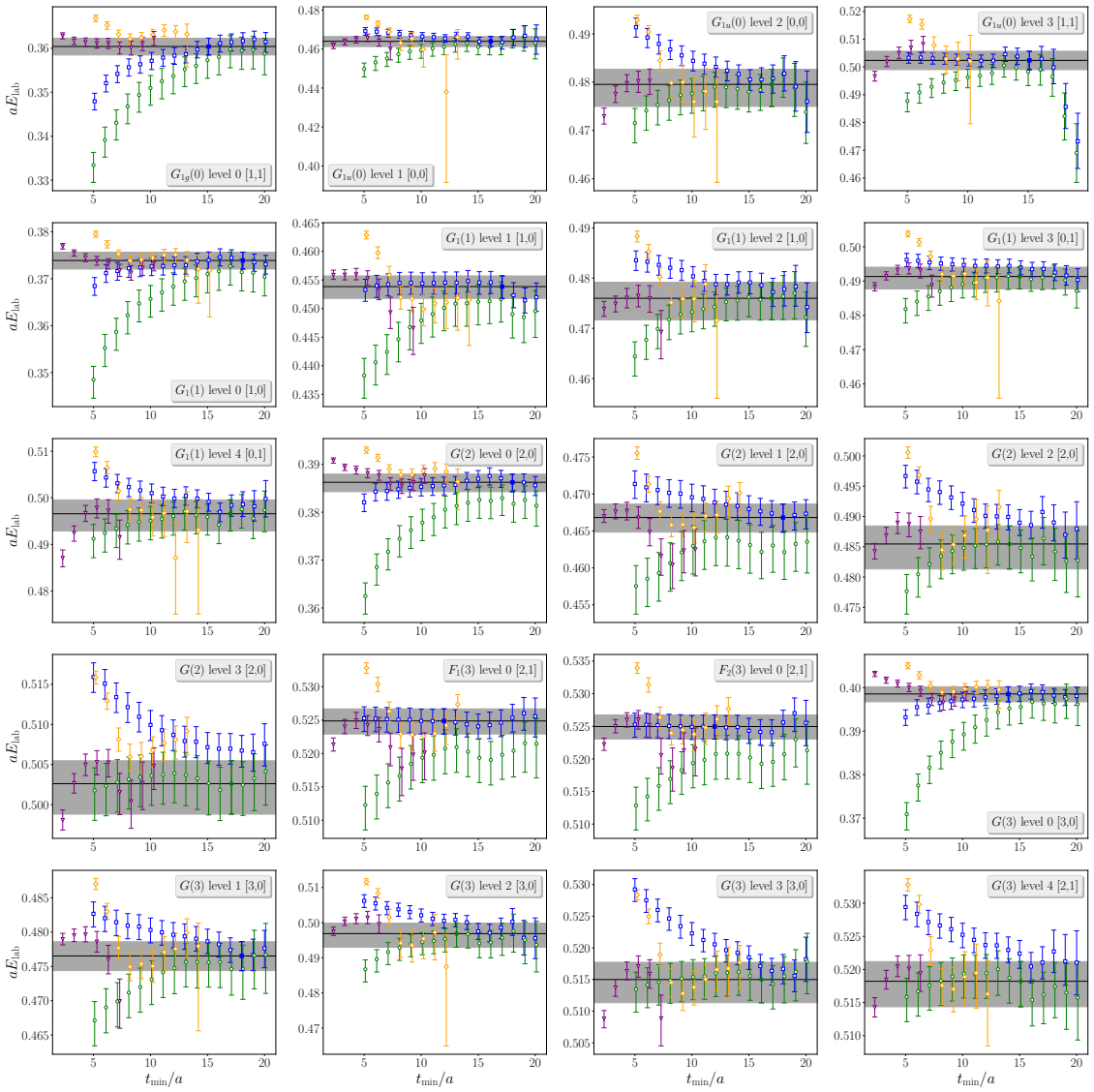

Figure B.7: Fit results for the stationary-state energies in the $\Lambda(1405)$ channel ($I = 0$). These plots are similar to those shown in Figure 8.2. Orange diamonds and purple triangles indicate results from fits using a two-exponential and a geometric-exp series, respectively. Green circles and blue squares indicate results from single-exponential fits to ratios of the rotated diagonal correlator over the product of $N(\boldsymbol{d}_1^2)$ $\overline{K}(\boldsymbol{d}_2^2)$ and $\Sigma(\boldsymbol{d}_1^2)$ $\pi(\boldsymbol{d}_2^2)$ single-hadron correlators, respectively, as described in Section 4.3.1. In each plot, the integers in square brackets in the legend show the values $[\boldsymbol{d}_1^2, \boldsymbol{d}_2^2]$. The dark horizontal band and the filled symbol denote the final chosen fit selected as described in Section 8.1.

Appendix C

$\Lambda(1405)$ Amplitude Fit Results

Best-fit results for the parameters in the various $\widetilde{K}$-matrix parameterizations are presented here. The results are obtained by fitting the spectrum obtained from the $\widetilde{K}$-matrix parametrizations and the quantization condition to the spectrum determined in the lattice QCD computations. Tables C.1-C.6 contain results from fits using $\ell_{\text{max}} = 0$.

Fit	A_{00}	A_{11}	A_{01}	B_{00}	B_{11}	B_{01}	χ^2/dof	AIC
a	1.5(1.4)	-8.78(72)	8.30(65)				15.68/(15-3)	-8.32
b	4.1(1.2)	-10.5(1.1)	10.3(1.3)			-29(15)	10.52/(15-4)	-11.48
c	2.3(1.3)	-8.62(58)	7.60(80)		-18(11)		12.29/(15-4)	-9.71
d	15.1(5.3)	-11.8(1.3)	7.6(1.3)	-56(19)			11.48/(15-4)	-10.52
e	9.6(6.2)	-12.7(3.4)	11.1(2.8)	-23(26)	18(31)	-37(29)	9.70/(15-6)	-8.30

Table C.1: Fit results for $\widetilde{K}$ parametrization class 1 shown in Eq. (8.1). Errors are propagated through the derivative method. Empty entries indicate parameters set to zero in a fit. AIC refers to Akaike Information Criterion.

Fit	$\widehat{A}_{00}$	$\widehat{A}_{11}$	$\widehat{A}_{01}$	$\widehat{B}_{00}$	$\widehat{B}_{11}$	$\widehat{B}_{01}$	χ^2/dof	AIC
a	0.16(19)	-1.229(91)	1.140(88)				15.44/(15-3)	-8.56
b	0.52(18)	-1.45(15)	1.42(18)			-3.9(2.0)	10.73/(15-4)	-11.27

Table C.2: Fit results for $\widetilde{K}$ parametrization class 2 shown in Eq. (8.2). Errors are propagated through the derivative method. Empty entries indicate parameters set to zero in a fit. AIC refers to Akaike Information Criterion.

Fit	$\widetilde{A}_{00}$	$\widetilde{A}_{11}$	$\widetilde{A}_{01}$	$\widetilde{B}_{00}$	$\widetilde{B}_{11}$	$\widetilde{B}_{01}$	χ^2/dof	AIC
a	0.092(21)	-0.036(15)	0.082(20)	0.28(15)			11.73/(15-4)	-10.27
b	0.114(25)	-0.041(24)	0.096(19)		0.19(16)		14.57/(15-4)	-7.43
c	0.137(33)	-0.019(14)	0.119(21)			-0.142(85)	13.10/(15-4)	-8.90

Table C.3: Fit results for $\widetilde{K}$ parametrization class 3 shown in Eq. (8.3). Errors are propagated through the derivative method. Empty entries indicate parameters set to zero in a fit. AIC refers to Akaike Information Criterion.

Fit	a_0	a_1	b_0	b_1	c_0	c_1	ϵ	χ^2/dof	AIC
a	5.7(1.2)	-11.4(1.2)		-27(15)			0.451(56)	13.27/(15-4)	-8.73
b	13.7(4.1)	-14.06(86)	-37(17)				0.349(75)	10.63/(15-4)	-11.37
c	5.8(1.2)	-11.8(1.1)				-1.62(95)	0.468(48)	13.54/(15-4)	-8.46
d	12.2(3.4)	-14.06(87)			5.8(3.2)		0.360(82)	11.13/(15-4)	-10.87

Table C.4: Fit results for $\widetilde{K}$ parametrization class 4 shown in Eq. (8.4). Errors are propagated through the derivative method. Empty entries indicate parameters set to zero in a fit. AIC refers to Akaike Information Criterion.

Fit	$\widehat{C}_{00}$	$\widehat{C}_{11}$	$\widehat{C}_{01}$	χ^2/dof	AIC
a	0.005(58)	-0.270(12)	-0.295(22)	15.28/(15-3)	-8.72

Table C.5: Fit results for $\widetilde{K}$ parametrization class 5 shown in Eq. (8.8). Errors are propagated through the derivative method. Empty entries indicate parameters set to zero in a fit. AIC refers to Akaike Information Criterion.

Fit	A'_{00}	A'_{11}	A'_{01}	B'_{00}	B'_{11}	B_{01}	χ^2/dof	AIC
a	2.11(77)	-1.64(19)	1.08(17)	-2.51(88)			11.88/(15-4)	-10.12
b	0.27(18)	-1.222(75)	1.05(11)		-0.69(44)		12.63/(15-4)	-9.37
c	0.51(18)	-1.46(15)	1.43(18)			-1.18(62)	10.76/(15-4)	-11.24

Table C.6: Fit results for $\widetilde{K}$ parametrization class 6 shown in Eq. (8.9). Errors are propagated through the derivative method. Empty entries indicate parameters set to zero in a fit. AIC refers to Akaike Information Criterion.

Appendix D

$\Delta(1232)$ Operator Analysis

As described in Section 7.3, it is essential to include all the operators that act on the eigenstates with energies in the elastic scattering range (for two-to-two scattering). If any of these operators are assumed to have no relation to such energies and are omitted, then the resulting spectrum may be incorrect. A test to detect missing levels using the method described in Section 7.3.3 is shown in Figures D.1-D.8. In each of these tests, I am considering a positive detection in which one of the fits to a diagonal correlator of the toy matrix produces a Δ greater than the variance of energy E_m. More details on the operators can be found in Appendix A.

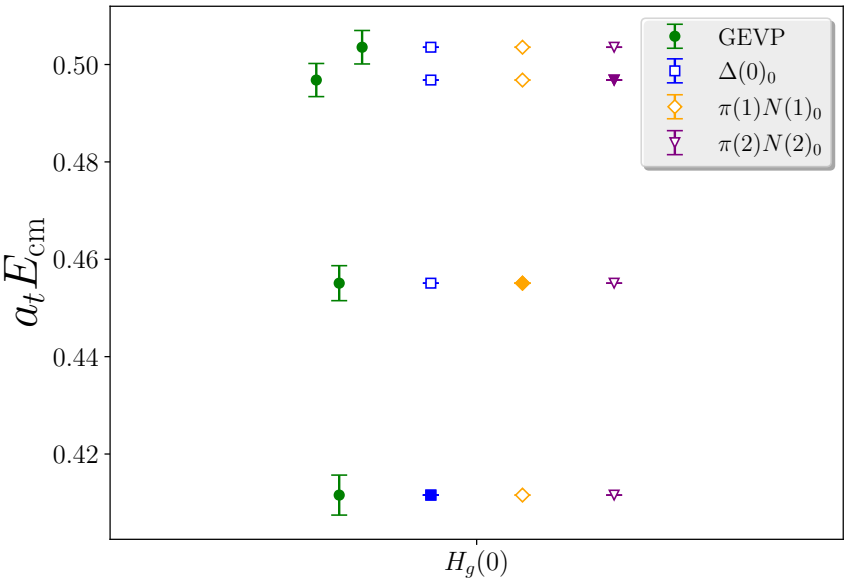

(a) Spectrum and fit results calculated from the full basis of toy correlators.

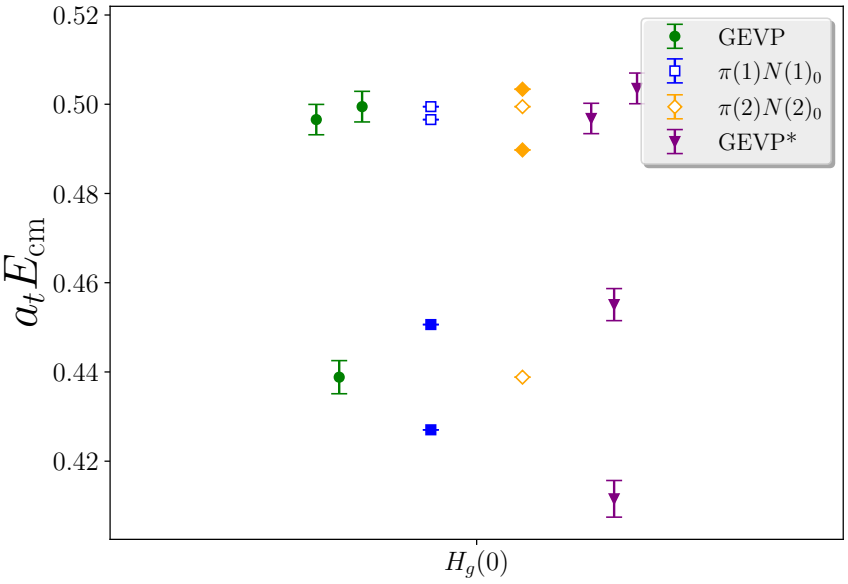

(b) Spectrum and fit results calculated from the truncated basis of toy correlators. Label 'GEVP*' is the original spectrum for reference.

Figure D.1: Fits to the toy correlators using spectrum determinations from the full and truncated correlation matrices. The fit form is Equation 7.7 and levels $E_m - \delta$ and $E_m + \delta$ are indicated by the filled symbols for each spectrum. The operator names indicate the flavor structure and the projected momentum on each constituent hadron. The index attached to each operator corresponds to its Clebsch-Gordan index.

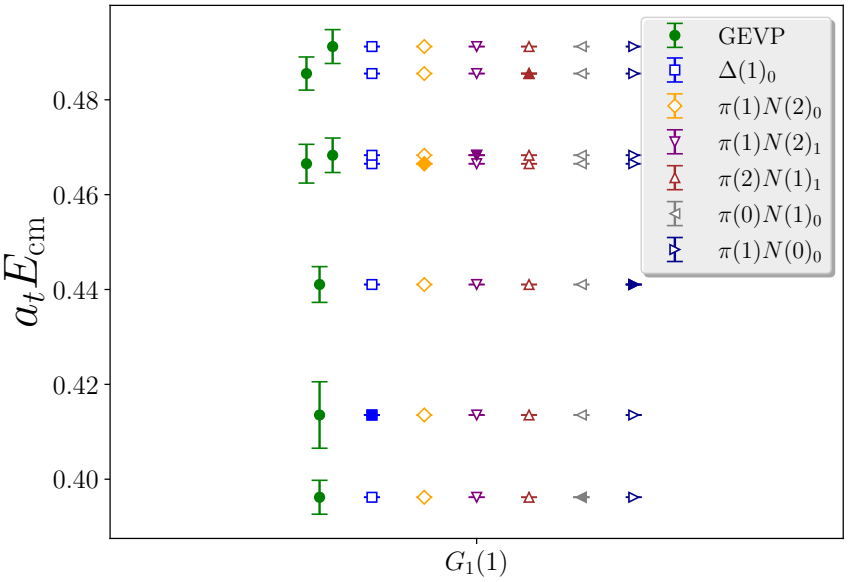

(a) Spectrum and fit results calculated from the full basis of toy correlators.

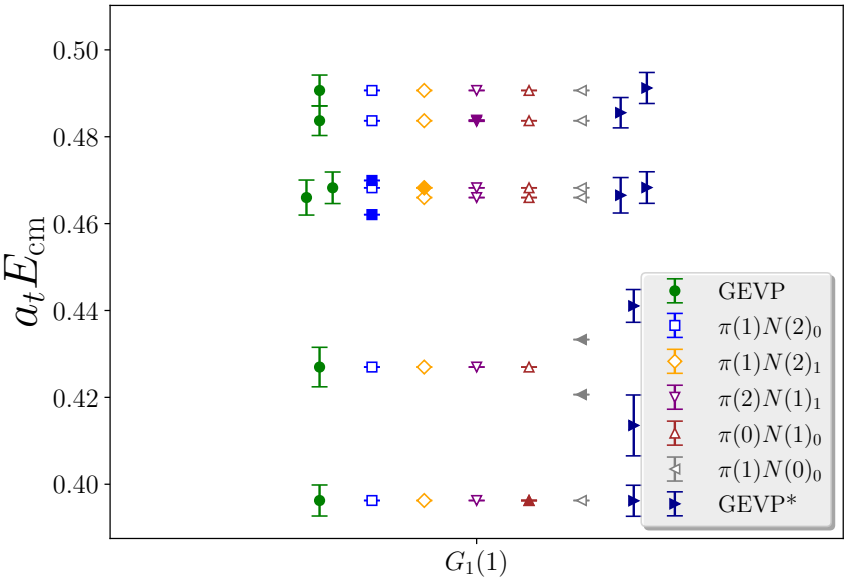

(b) Spectrum and fit results calculated from the truncated basis of toy correlators.

Figure D.2: Fits to the toy correlators using spectrum determinations from the full and truncated correlation matrices. Labels are the same as in Figure D.1.

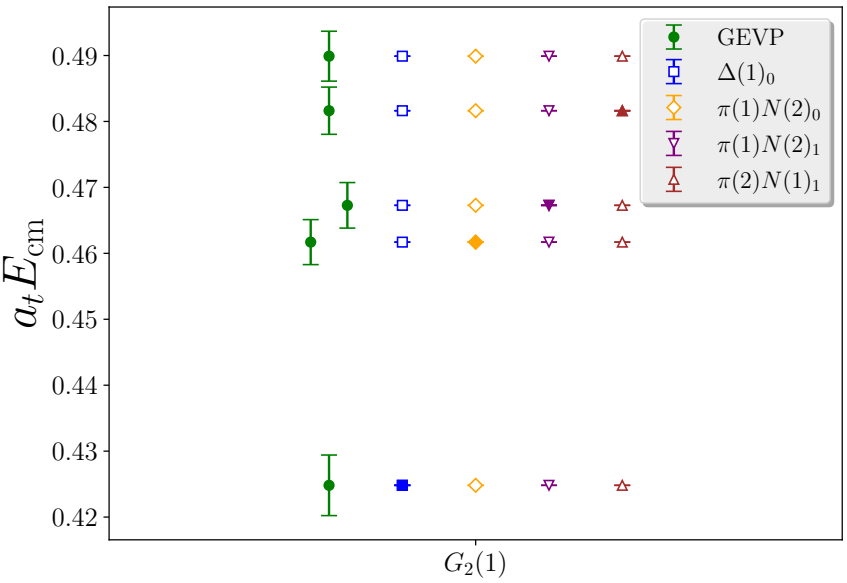

(a) Spectrum and fit results calculated from the full basis of toy correlators.

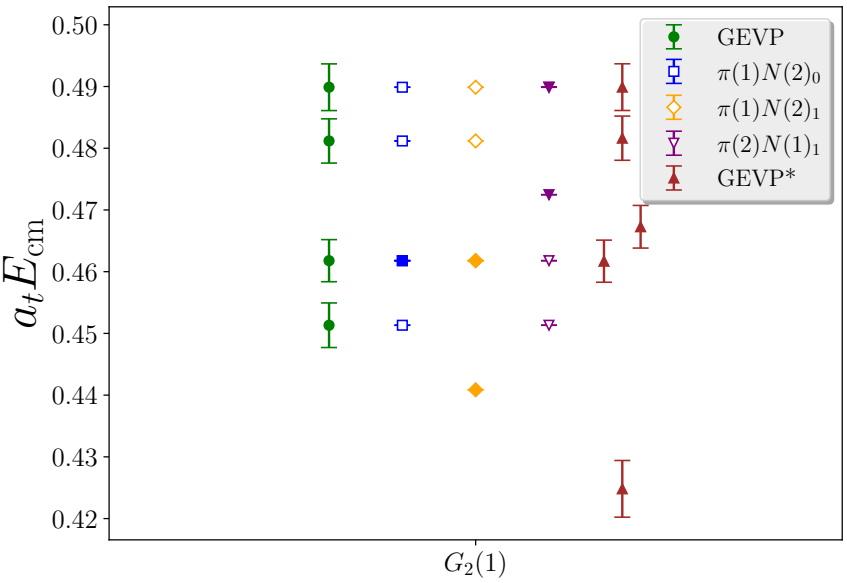

(b) Spectrum and fit results calculated from the truncated basis of toy correlators. Label 'GEVP*' is the original spectrum for reference.

Figure D.3: Fits to the toy correlators using spectrum determinations from the full and truncated correlation matrices. Labels are the same as in Figure D.1.

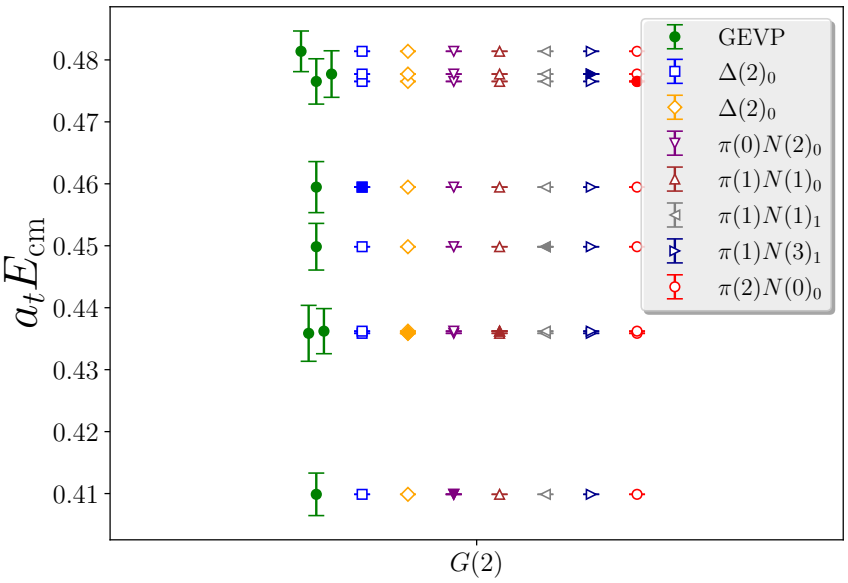

(a) Spectrum and fit results calculated from the full basis of toy correlators.

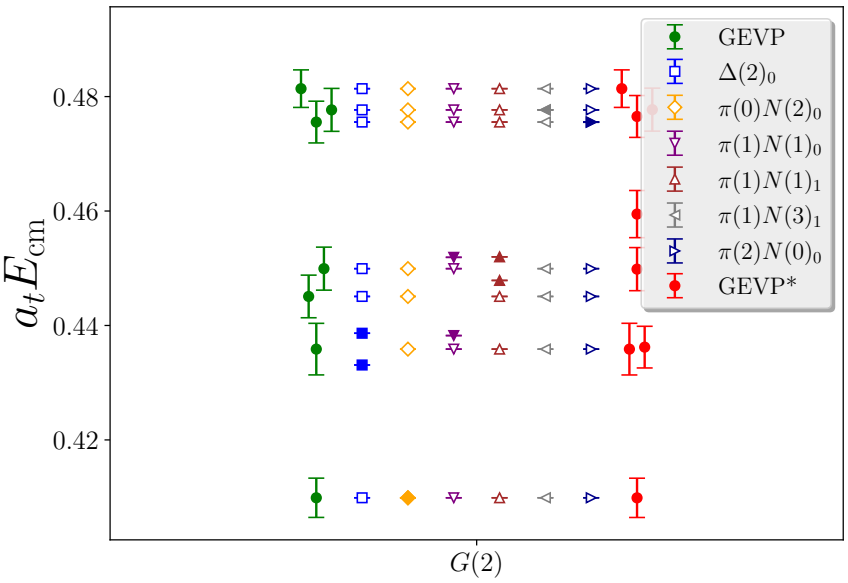

(b) Spectrum and fit results calculated from the truncated basis of toy correlators. Label 'GEVP*' is the original spectrum for reference.

Figure D.4: Fits to the toy correlators using spectrum determinations from the full and truncated correlation matrices. Labels are the same as in Figure D.1.

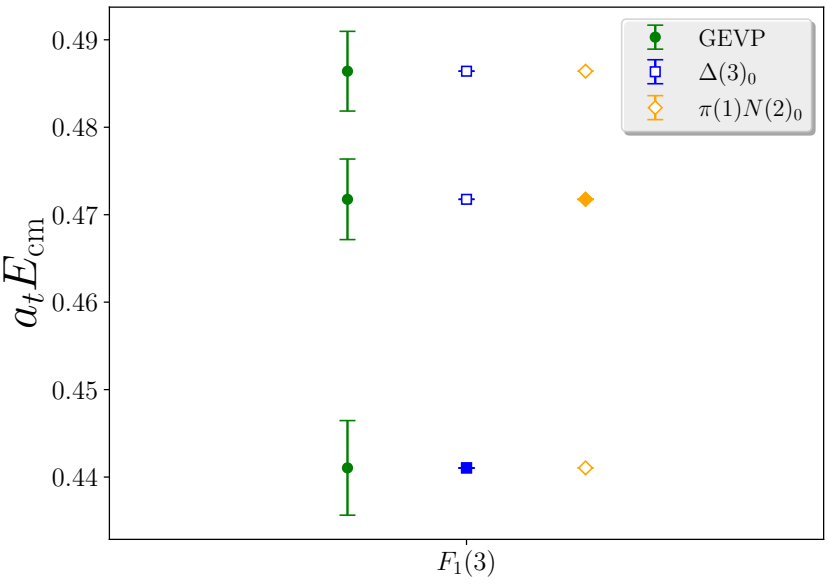

(a) Spectrum and fit results calculated from the full basis of toy correlators.

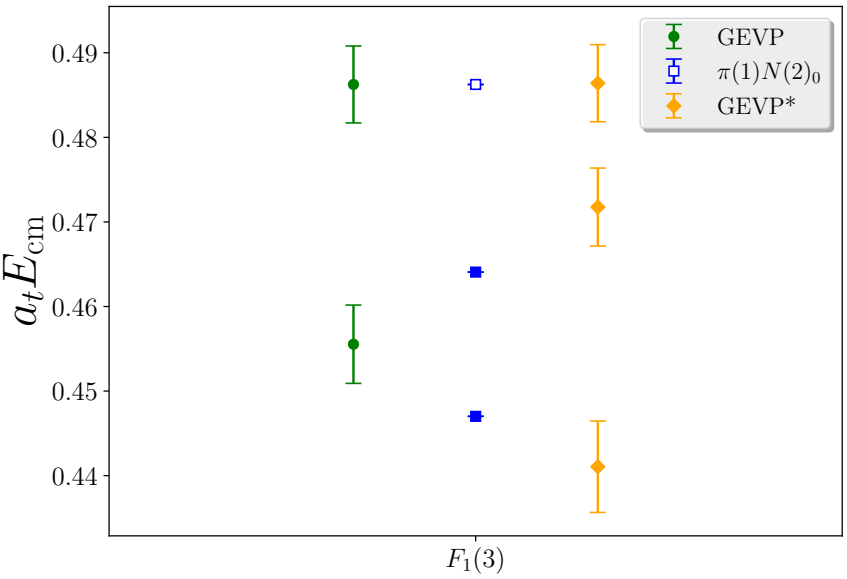

(b) Spectrum and fit results calculated from the truncated basis of toy correlators. Label 'GEVP*' is the original spectrum for reference.

Figure D.5: Fits to the toy correlators using spectrum determinations from the full and truncated correlation matrices. Labels are the same as in Figure D.1.

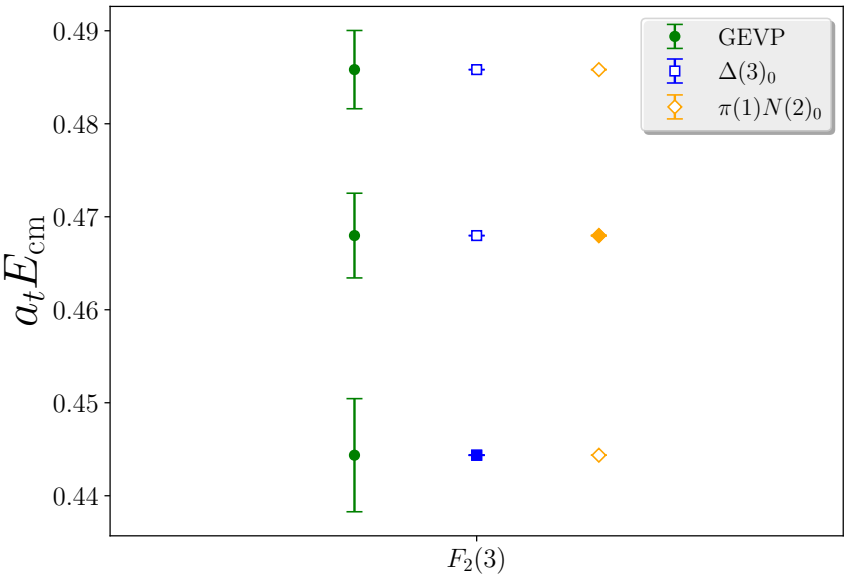

(a) Spectrum and fit results calculated from the full basis of toy correlators.

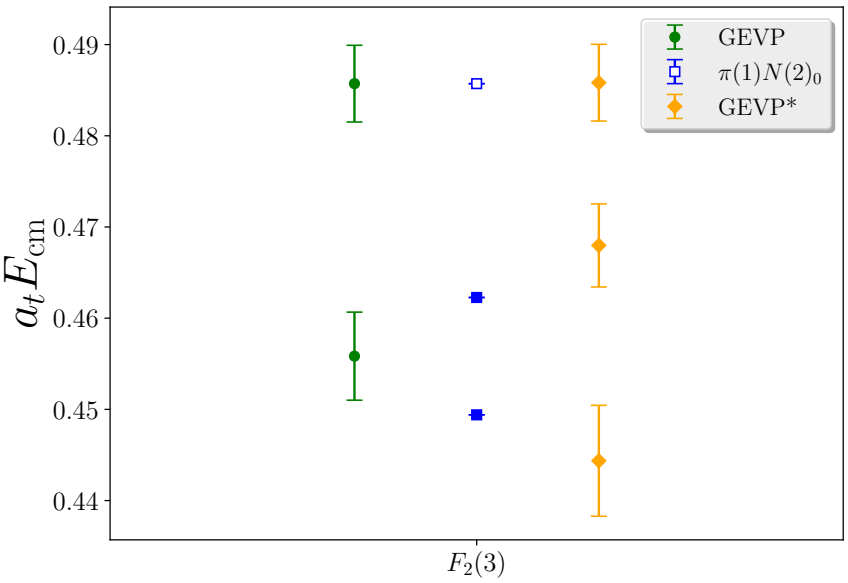

(b) Spectrum and fit results calculated from the truncated basis of toy correlators. Label 'GEVP*' is the original spectrum for reference.

Figure D.6: Fits to the toy correlators using spectrum determinations from the full and truncated correlation matrices. Labels are the same as in Figure D.1.

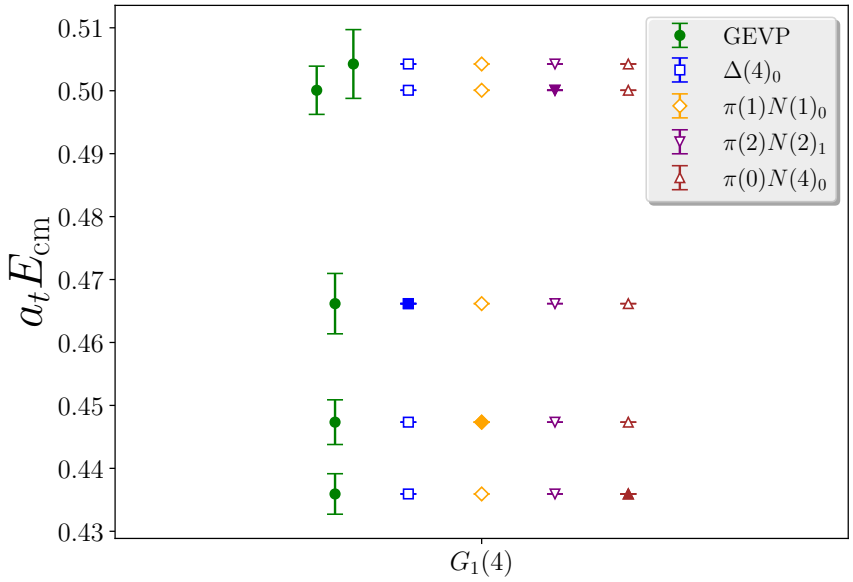

(a) Spectrum and fit results calculated from the full basis of toy correlators.

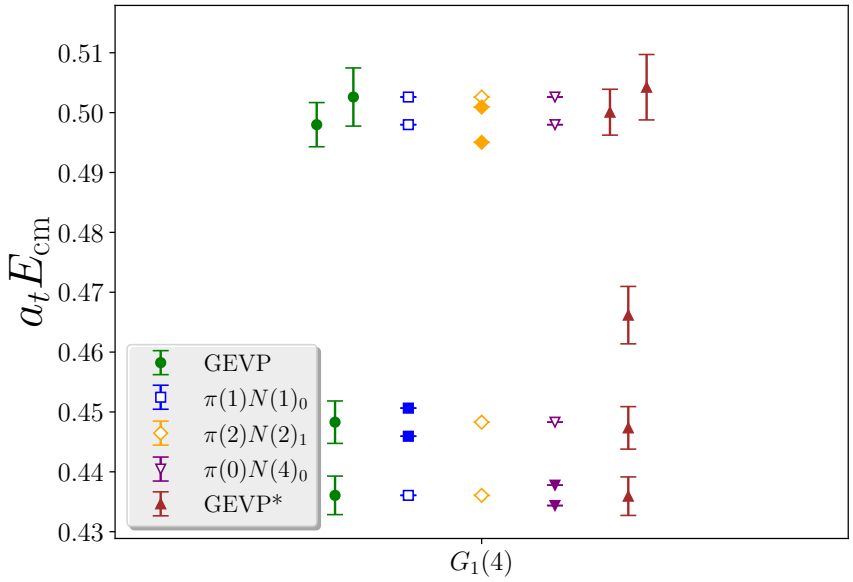

(b) Spectrum and fit results calculated from the truncated basis of toy correlators.

Figure D.7: Fits to the toy correlators using spectrum determinations from the full and truncated correlation matrices. Labels are the same as in Figure D.1.

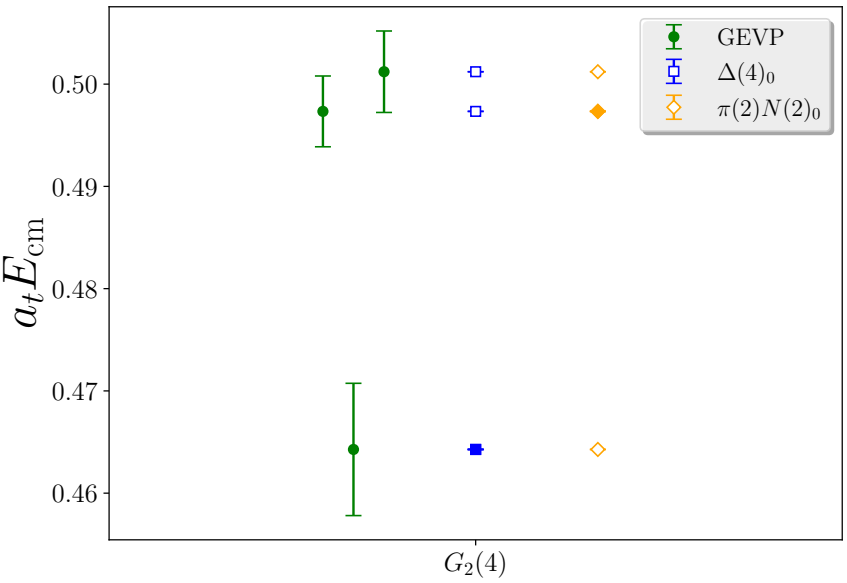

(a) Spectrum and fit results calculated from the full basis of toy correlators.

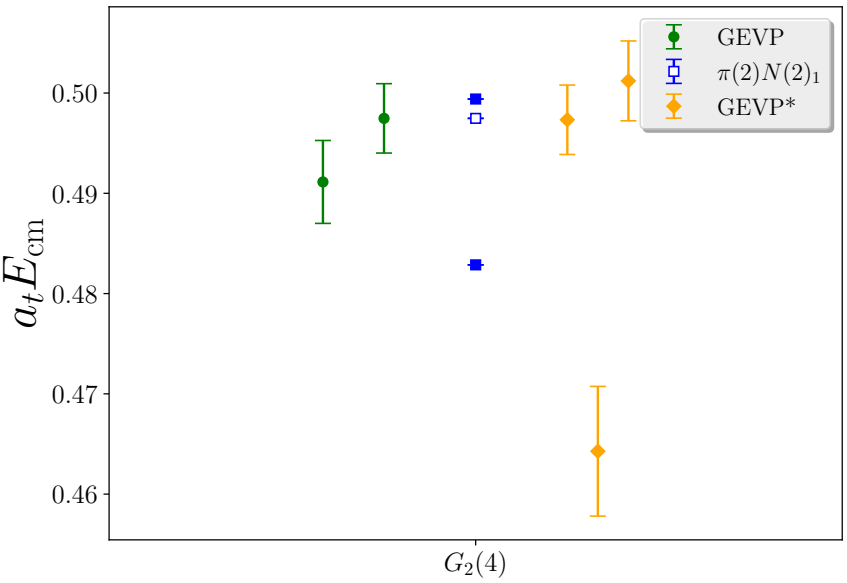

(b) Spectrum and fit results calculated from the truncated basis of toy correlators. Label 'GEVP*' is the original spectrum for reference.

Figure D.8: Fits to the toy correlators using spectrum determinations from the full and truncated correlation matrices. Labels are the same as in Figure D.1.

Bibliography

[1] *Texas Advanced Computing Center*, `https://www.tacc.utexas.edu/systems/frontera`.

[2] H. Fritzsch, M. Gell-Mann, and H. Leutwyler, "Advantages of the Color Octet Gluon Picture", Phys. Lett. B **47**, 365–368 (1973).

[3] M. Peardon, J. Bulava, J. Foley, C. Morningstar, J. Dudek, R. G. Edwards, B. Joo, H.-W. Lin, D. G. Richards, and K. J. Juge (Hadron Spectrum), "A Novel quark-field creation operator construction for hadronic physics in lattice QCD", Phys. Rev. **D80**, 054506 (2009).

[4] C. Morningstar, J. Bulava, J. Foley, K. J. Juge, D. Lenkner, M. Peardon, and C. H. Wong, "Improved stochastic estimation of quark propagation with Laplacian Heaviside smearing in lattice QCD", Phys. Rev. **D83**, 114505 (2011).

[5] C. W. Andersen, J. Bulava, B. Hörz, and C. Morningstar, "Elastic $I = 3/2$, p-wave nucleon-pion scattering amplitude and the $\Delta(1232)$ resonance from N_f=2+1 lattice QCD", Phys. Rev. **D97**, 014506 (2018).

[6] C. B. Lang, L. Leskovec, M. Padmanath, and S. Prelovsek, "Pion-nucleon scattering in the Roper channel from lattice QCD", Phys. Rev. **D95**, 014510 (2017).

[7] B. Abi et al. (DUNE), "Deep Underground Neutrino Experiment (DUNE), Far Detector Technical Design Report, Volume I Introduction to DUNE", JINST **15**, T08008 (2020).

[8] K. Abe et al. (Hyper-Kamiokande), "Hyper-Kamiokande Design Report", (2018).

[9] R. L. Workman et al. (Particle Data Group), "Review of Particle Physics", PTEP **2022**, 083C01 (2022).

[10] P. Gubler, T. T. Takahashi, and M. Oka, "Flavor structure of Λ baryons from lattice QCD: From strange to charm quarks", Phys. Rev. D **94**, 114518 (2016).

[11] B. J. Menadue, W. Kamleh, D. B. Leinweber, and M. S. Mahbub, "Isolating the $\Lambda(1405)$ in Lattice QCD", Phys. Rev. Lett. **108**, 112001 (2012).

[12] G. P. Engel, C. B. Lang, and A. Schäfer (BGR (Bern-Graz-Regensburg)), "Low-lying Λ baryons from the lattice", Phys. Rev. D **87**, 034502 (2013).

[13]Y. Nemoto, N. Nakajima, H. Matsufuru, and H. Suganuma, "Negative parity baryons in quenched anisotropic lattice QCD", Phys. Rev. D **68**, 094505 (2003).

[14]T. Burch, C. Gattringer, L. Y. Glozman, C. Hagen, D. Hierl, C. B. Lang, and A. Schafer, "Excited hadrons on the lattice: Baryons", Phys. Rev. D **74**, 014504 (2006).

[15]T. T. Takahashi and M. Oka, "Low-lying Lambda Baryons with spin 1/2 in Two-flavor Lattice QCD", Phys. Rev. D **81**, 034505 (2010).

[16]S. Meinel and G. Rendon, "Charm-baryon semileptonic decays and the strange Λ^* resonances: New insights from lattice QCD", Phys. Rev. D **105**, L051505 (2022).

[17]J. M. M. Hall, W. Kamleh, D. B. Leinweber, B. J. Menadue, B. J. Owen, A. W. Thomas, and R. D. Young, "Lattice QCD Evidence that the $\Lambda(1405)$ Resonance is an Antikaon-Nucleon Molecule", Phys. Rev. Lett. **114**, 132002 (2015).

[18]J. Bulava et al. (Baryon Scattering (BaSc)), "Two-Pole Nature of the $\Lambda(1405)$ resonance from Lattice QCD", Phys. Rev. Lett. **132**, 051901 (2024).

[19]J. Bulava et al. (Baryon Scattering (BaSc)), "Lattice QCD study of $\pi\Sigma$-K^{-}N scattering and the $\Lambda(1405)$ resonance", Phys. Rev. D **109**, 014511 (2024).

[20]U. of Sheffield Open Educational Resources, *Nuclear and Particle Physics: The Feynman diagrams of QCD*, (2024) `https://oer.physics.manchester.ac.uk/NP/Notes/Notes/Notesse54.xht` (visited on 03/15/2010).

[21]K. G. Wilson, "Confinement of Quarks", Phys. Rev. D **10**, 2445–2459 (1974).

[22]C. Gattringer and C. B. Lang, *Quantum chromodynamics on the lattice*, Vol. 788 (Springer, Berlin, 2010).

[23]H. Nielsen and M. Ninomiya, "A no-go theorem for regularizing chiral fermions", Physics Letters B **105**, 219–223 (1981).

[24]M. Luscher and P. Weisz, "On-Shell Improved Lattice Gauge Theories", Commun. Math. Phys. **97**, [Erratum: Commun. Math. Phys.98,433(1985)], 59 (1985).

[25]J. Bulava and S. Schaefer, "Improvement of $N_{\mathrm{f}} = 3$ lattice QCD with Wilson fermions and tree-level improved gauge action", Nucl. Phys. **B874**, 188–197 (2013).

[26]S. Duane, A. Kennedy, B. Pendleton, and D. Roweth, "Hybrid Monte Carlo", Phys. Lett. B **195**, 216–222 (1987).

[27]M. A. Clark and A. D. Kennedy, "Accelerating dynamical fermion computations using the rational hybrid Monte Carlo (RHMC) algorithm with multiple pseudofermion fields", Phys. Rev. Lett. **98**, 051601 (2007).

[28]M. Clark, "The Rational Hybrid Monte Carlo Algorithm", PoS **LAT2006**, edited by T. Blum, M. Creutz, C. DeTar, F. Karsch, A. Kronfeld, C. Morningstar, D. Richards, J. Shigemitsu, and D. Toussaint, 004 (2006).

[29]C. Morningstar and M. J. Peardon, "Analytic smearing of SU(3) link variables in lattice QCD", Phys. Rev. **D69**, 054501 (2004).

[30]R. C. Johnson, "Angular momentum on a lattice", Phys. Lett. B **114**, 147–151 (1982).

[31]J. Slater, *Quantum Theory of Molecules and Solids. Volume 1: Electronic structure of molecules*, Vol. 1 (McGraw-Hill, New York, 1963), Appendix 12.

[32]C. Morningstar, J. Bulava, B. Fahy, J. Foley, Y. Jhang, et al., "Extended hadron and two-hadron operators of definite momentum for spectrum calculations in lattice QCD", Phys.Rev. **D88**, 014511 (2013).

[33]S. Basak, R. G. Edwards, G. T. Fleming, U. M. Heller, C. Morningstar, D. Richards, I. Sato, and S. Wallace, "Group-theoretical construction of extended baryon operators in lattice QCD", Phys. Rev. **D72**, 094506 (2005).

[34]M. Luscher and U. Wolff, "How to Calculate the Elastic Scattering Matrix in Two-dimensional Quantum Field Theories by Numerical Simulation", Nucl. Phys. **B339**, 222–252 (1990).

[35]W. I. Jay and E. T. Neil, "Bayesian model averaging for analysis of lattice field theory results", Phys. Rev. D **103**, 114502 (2021).

[36]T. D. Blanton, A. D. Hanlon, B. Hörz, C. Morningstar, F. Romero-López, and S. R. Sharpe, "Interactions of two and three mesons including higher partial waves from lattice QCD", JHEP **10**, 023 (2021).

[37]G. P. Lepage, B. Clark, C. T. H. Davies, K. Hornbostel, P. B. Mackenzie, C. Morningstar, and H. Trottier (HPQCD), "Constrained curve fitting", Nucl. Phys. B Proc. Suppl. **106**, edited by M. Muller-Preussker, W. Bietenholz, K. Jansen, F. Jegerlehner, I. Montvay, G. Schierholz, R. Sommer, and U. Wolff, 12–20 (2002).

[38]R. A. Briceño, J. J. Dudek, and R. D. Young, "Scattering processes and resonances from lattice QCD", (2017).

[39]C. Morningstar, J. Bulava, B. Singha, R. Brett, J. Fallica, A. Hanlon, and B. Hörz, "Estimating the two-particle K-matrix for multiple partial waves and decay channels from finite-volume energies", Nucl. Phys. **B924**, 477–507 (2017).

[40]W. Commons, *Differential cross section*, (2014) `https://commons.wikimedia.org/wiki/File:Differential_cross_section.svg`.

[41]W. Commons, *Riemann surface sqrt*, (2015) `https://commons.wikimedia.org/wiki/File:Riemann_surface_sqrt.svg`.

[42]T. Degrand and C. Detar, *Lattice methods for quantum chromodynamics* (World Scientific Publishing Company, 2006).

[43]B. S. DeWitt, "Transition from discrete to continuous spectra", Phys. Rev. **103**, 1565–1571 (1956).

[44]K. Huang and C. N. Yang, "Quantum-mechanical many-body problem with hard-sphere interaction", Phys. Rev. **105**, 767–775 (1957).

[45]M. Luscher, "Volume Dependence of the Energy Spectrum in Massive Quantum Field Theories. 2. Scattering States", Commun. Math. Phys. **105**, 153–188 (1986).

[46]M. Lüscher, "Two particle states on a torus and their relation to the scattering matrix", Nucl. Phys. **B354**, 531–578 (1991).

[47]K. Rummukainen and S. A. Gottlieb, "Resonance scattering phase shifts on a non-rest frame lattice", Nucl. Phys. **B450**, 397–436 (1995).

[48]X. Feng, X. Li, and C. Liu, "Two particle states in an asymmetric box and the elastic scattering phases", Phys. Rev. **D70**, 014505 (2004).

[49]S. He, X. Feng, and C. Liu, "Two particle states and the S-matrix elements in multi-channel scattering", JHEP **07**, 011 (2005).

[50]P. F. Bedaque, "Aharonov-Bohm effect and nucleon nucleon phase shifts on the lattice", Phys. Lett. B **593**, 82–88 (2004).

[51]C. Liu, X. Feng, and S. He, "Two particle states in a box and the S-matrix in multi-channel scattering", Int. J. Mod. Phys. A **21**, edited by K.-T. Chao, X.-D. Ji, and C. Liu, 847–850 (2006).

[52]C. h. Kim, C. T. Sachrajda, and S. R. Sharpe, "Finite-volume effects for two-hadron states in moving frames", Nucl. Phys. **B727**, 218–243 (2005).

[53]N. H. Christ, C. Kim, and T. Yamazaki, "Finite volume corrections to the two-particle decay of states with non-zero momentum", Phys. Rev. D **72**, 114506 (2005).

[54]M. Lage, U.-G. Meißner, and A. Rusetsky, "A Method to measure the antikaon-nucleon scattering length in lattice QCD", Phys. Lett. **B681**, 439–443 (2009).

[55]V. Bernard, M. Lage, U. G. Meissner, and A. Rusetsky, "Scalar mesons in a finite volume", JHEP **01**, 019 (2011).

[56]Z. Fu, "Rummukainen-Gottlieb's formula on two-particle system with different mass", Phys. Rev. **D85**, 014506 (2012).

[57]L. Leskovec and S. Prelovsek, "Scattering phase shifts for two particles of different mass and non-zero total momentum in lattice QCD", Phys. Rev. D **85**, 114507 (2012).

[58]R. A. Briceno and Z. Davoudi, "Moving multichannel systems in a finite volume with application to proton-proton fusion", Phys. Rev. **D88**, 094507 (2013).

[59]M. T. Hansen and S. R. Sharpe, "Multiple-channel generalization of Lellouch-Luscher formula", Phys. Rev. **D86**, 016007 (2012).

[60]P. Guo, J. Dudek, R. Edwards, and A. P. Szczepaniak, "Coupled-channel scattering on a torus", Phys. Rev. D **88**, 014501 (2013).

[61]N. Li and C. Liu, "Generalized Lüscher formula in multichannel baryon-meson scattering", Phys. Rev. **D87**, 014502 (2013).

[62]R. A. Briceno, Z. Davoudi, T. C. Luu, and M. J. Savage, "Two-Baryon Systems with Twisted Boundary Conditions", Phys. Rev. D **89**, 074509 (2014).

[63]R. A. Briceno, "Two-particle multichannel systems in a finite volume with arbitrary spin", Phys. Rev. **D89**, 074507 (2014).

[64]A. W. Jackura and R. A. Briceño, "Partial-wave projection of the one-particle exchange in three-body scattering amplitudes", Phys. Rev. D **109**, 096030 (2024).

[65]Z. T. Draper, A. D. Hanlon, B. Hörz, C. Morningstar, F. Romero-López, and S. R. Sharpe, "Interactions of πK, $\pi\pi$K and KKπ systems at maximal isospin from lattice QCD", JHEP **05**, 137 (2023).

[66]T. Luu and M. J. Savage, "Extracting Scattering Phase-Shifts in Higher Partial-Waves from Lattice QCD Calculations", Phys. Rev. D **83**, 114508 (2011).

[67]M. Göckeler, R. Horsley, M. Lage, U. G. Meißner, P. E. L. Rakow, A. Rusetsky, G. Schierholz, and J. M. Zanotti, "Scattering phases for meson and baryon resonances on general moving-frame lattices", Phys. Rev. **D86**, 094513 (2012).

[68]M. Bruno et al., "Simulation of QCD with $\mathrm{N}_f = 2 + 1$ flavors of non-perturbatively improved Wilson fermions", JHEP **02**, 043 (2015).

[69]G. S. Bali, V. Braun, S. Collins, A. Schäfer, and J. Simeth (RQCD), "Masses and decay constants of the η and η' mesons from lattice QCD", JHEP **08**, 137 (2021).

[70]M. Cè et al., "Window observable for the hadronic vacuum polarization contribution to the muon g-2 from lattice QCD", Phys. Rev. D **106**, 114502 (2022).

[71]M. Lüscher and S. Schaefer, "Lattice QCD without topology barriers", JHEP **07**, 036 (2011).

[72]C. Andersen, J. Bulava, B. Hörz, and C. Morningstar, "The $I = 1$ pion-pion scattering amplitude and timelike pion form factor from $N_\mathrm{f} = 2+1$ lattice QCD", Nucl. Phys. **B939**, 145–173 (2019).

[73]D. Mohler and S. Schaefer, "Remarks on strange-quark simulations with Wilson fermions", Phys. Rev. D **102**, 074506 (2020).

[74]M. Lüscher and F. Palombi, "Fluctuations and reweighting of the quark determinant on large lattices", PoS **LATTICE2008**, 049 (2008).

[75]S. Kuberski, "Low-mode deflation for twisted-mass and RHMC reweighting in lattice QCD", Comput. Phys. Commun. **300**, 109173 (2024).

[76]M. Bruno, T. Korzec, and S. Schaefer, "Setting the scale for the CLS $2 + 1$ flavor ensembles", Phys. Rev. **D95**, 074504 (2017).

[77]B. Strassberger et al., "Scale setting for CLS 2+1 simulations", PoS **LATTICE2021**, 135 (2022).

[78]J. Bulava, A. D. Hanlon, B. Hörz, C. Morningstar, A. Nicholson, F. Romero-López, S. Skinner, P. Vranas, and A. Walker-Loud, "Elastic nucleon-pion scattering at $m_\pi = 200$ MeV from lattice QCD", (2022).

[79]F. J. Yndurain, R. Garcia-Martin, and J. R. Pelaez, "Experimental status of the $\pi\pi$ isoscalar S-wave at low energy: $f_0(600)$ pole and scattering length", Phys. Rev. D **76**, 074034 (2007).

[80]G. Silvi et al., "P-wave nucleon-pion scattering amplitude in the $\Delta(1232)$ channel from lattice QCD", Phys. Rev. D **103**, 094508 (2021).

[81]C. Alexandrou, S. Bacchio, G. Koutsou, T. Leontiou, S. Paul, M. Petschlies, and F. Pittler, "Elastic nucleon-pion scattering amplitudes in the Δ channel at physical pion mass from lattice QCD", Phys. Rev. D **109**, 034509 (2024).

[82]M. Fukugita, Y. Kuramashi, M. Okawa, H. Mino, and A. Ukawa, "Hadron scattering lengths in lattice QCD", Phys. Rev. **D52**, 3003–3023 (1995).

[83]C. Lang and V. Verduci, "Scattering in the πN negative parity channel in lattice QCD", Phys.Rev. **D87**, 054502 (2013).

[84]T. R. Hemmert, B. R. Holstein, and N. C. Mukhopadhyay, "NN,$N\Delta$ couplings and the quark model", Phys. Rev. **D51**, 158–167 (1995).

[85]M. Hoferichter, J. Ruiz de Elvira, B. Kubis, and U.-G. Meißner, "Matching pion-nucleon Roy-Steiner equations to chiral perturbation theory", Phys. Rev. Lett. **115**, 192301 (2015).

[86]J. Bulava, D. Darvish, A. D. Hanlon, B. Hörz, C. Morningstar, A. Nicholson, F. Romero-López, S. Skinner, P. Vranas, and A. Walker-Loud, "Lattice QCD studies of the Δ baryon resonance and the $K_0^*(700)$ and $a_0(980)$ meson resonances: the role of exotic operators in determining the finite-volume spectrum", in 40th International Symposium on Lattice Field Theory (Dec. 2023).

[87]J. D. Hunter, "Matplotlib: A 2D Graphics Environment", Comput. Sci. Eng. **9**, 90–95 (2007).

[88]J. M. Blatt and L. C. Biedenharn, "Neutron-Proton Scattering with Spin-Orbit Coupling. 1. General Expressions", Phys. Rev. **86**, 399–404 (1952).

[89]E. Oset and A. Ramos, "Nonperturbative chiral approach to s-wave $\bar{K}N$ interactions", Nucl. Phys. A **635**, 99–120 (1998).

[90]S. Skinner, *Finite-volume spectrum of the isosinglet strange channel calculated in lattice QCD* (Zenodo, Jan. 2024).